TẠP CHÍ KHOA HỌC
TRƯỜNG ĐẠI HỌC QUY NHƠN

Đánh giá ban đầu về ô nhiễm vi nhựa trong trầm tích bãi biển và nước bề mặt ở khu vực ven bờ thành phố Quy Nhơn

Võ Văn Chí*, Nguyễn Thị Phương Hiền

Khoa Khoa học Tự nhiên, Trường Đại học Quy Nhơn, Việt Nam

Ngày nhận bài: 30/11/2021; Ngày nhận đăng: 18/02/2022

TÓM TẮT

Nghiên cứu được thực hiện để đánh giá mức độ ô nhiễm vi nhựa trong nước bề mặt và trong trầm tích bãi biển khu vực thành phố Quy Nhơn. Các mẫu nước và trầm tích được thu tại 4 điểm dọc theo bãi biển Quy Nhơn để phân tích. Mẫu nước được xử lý bằng SDS, Biozym ES, Biozym F và H_2O_2 30% trong khi mẫu trầm tích chỉ xử lý bằng H_2O_2 30%. Kết quả cho thấy mật độ vi nhựa trong nước bề mặt dao động từ 16,37 – 62,86 vi nhựa/m^3 và trung bình là 30,32 vi nhựa/m^3 trong khi mật độ vi nhựa trong trầm tích dao động trong khoảng 1.700 – 3.100 vi nhựa/kg trầm tích khô và trung bình là 2.400 vi nhựa/kg trầm tích khô. Nguồn nước thải trực tiếp từ thành phố được xem là nguồn gây ô nhiễm vi nhựa chính ở khu vực nghiên cứu. Chiều dài các sợi vi nhựa chủ yếu trong khoảng 300 – 2000 µm trong khi diện tích các mảnh vi nhựa tập trung ở nhóm 45000 – 400000 $µm^2$. Màu xanh biển, màu trắng và màu tím là những màu chủ đạo của vi nhựa dạng sợi và màu trắng, vàng và xanh biển là các màu ưu thế của vi nhựa dạng mảnh.

Từ khóa: *Vi nhựa, Quy Nhơn, sự ô nhiễm, trầm tích, nước bề mặt.*

**Tác giả liên hệ chính.*
Email: vovanchi@qnu.edu.vn

JOURNAL OF SCIENCE
QUY NHON UNIVERSITY

Baseline assessment of microplastic contamination in beach sediments and surface waters around the coastal areas of Quy Nhon city

Vo Van Chi*, Nguyen Thi Phuong Hien

Faculty of Natural Sciences, Quy Nhon University, Vietnam

Received: 30/11/2021; Accepted: 18/02/2022

ABSTRACT

The study was carried out to assess microplastic contamination in surface waters and beach sediments around the coastal areas of Quy Nhon city. The water and sediment samples were collected at 4 sites along Quy Nhon beach for analysis. The water samples were treated by SDS, Biozym ES, Biozym F and H_2O_2 30% while sediments were only treated by H_2O_2 30%. The results showed that the microplastic concentration in surface water was from 16.37 – 62.86 items/m^3 with average of 30.32 items/m^3 while this in sediments fluctuated in the range of 1700 – 3100 items/kg of dry sediment with average of 2400 items/kg of dry sediment. The domestic wastewaters from the city are considered as the major source causing microplastic contamination at study sites. The length of microfibers was mostly in the range of 300 – 2000 µm and the area of microfragments was dominant in the range of 45000 – 400000 µm^2. Blue, white and purple were the dominant colors of microfibers, and white, yellow and blue were predominant for microfragments.

Keywords: *Microplastic, Quy Nhon, contamination, sediments, surface water*.

1. INTRODUCTION

Plastic pollution is one of noticable problems in the world, causing negative effects on ecosystems, especially aquatic ecosystems, and also causing potential impacts on human health. Plastic wastes released from human activities mostly end up in the seas and oceans via rivers. Under the influence of environmental factors, especially in coastal areas, such as high temperature, high radiation intensity, waves and wind, large plastic samples are separated into microplastics,[1] that have the size of from 1 µm to 5000 µm.[2] Rahman et al. reported that microplastics can cause direct effects on human health through oxidative stress and cytotoxicity, altering metabolism, neurotoxicity, reproductive system toxicity, carcinogenic, or indirect effect as a vector to transfer chemicals and microorganisms into human body.[3]

Costal ecosystems are places loaded a large amount of macroplastics and microplastics from inland as well as marine activities.[4] Therefore, microplastics can be distributed in different environments in these ecosystems. The microplastic distribution in sediments has been reported in many studies in the world, with different concentrations from the low values as of 1.3 – 36.3 particles/kg dry sediment[5] or

*Corresponding author.
Email: vovanchi@qnu.edu.vn

https://doi.org/10.52111/qnjs.2022.16304

48.7 – 390.7 particles/kg dry sediment[6] to high values as of 2000 – 8000 particles/kg dry sediment[7], 5020 – 8720 particles/kg dry sediment[8] or 3000 – 18000 particles/kg dry sediment.[2] Similarly, microplastic contamination in water environment has been recorded with different densities at studied areas. This was clearly mentioned in the study of Rodrigues *et al.*[9] at the costal areas in Portugal; microplastic concentration varied from 0.015 particales/m^3 at the protected water to 0.17 particales/m^3 at urban estuary, or 2748 particles/m^3 at areas associated with submarine wreck and 4028 particales/m^3 at recreational marina. Other studies also showed the different concentrations of microplastic in waters, such as from 380 to 610 particles/m^3 at Surabaya bay – Indonesia,[10] 1660 - 8925 particles/m^3 at urban lakes in China,[11] or 10000 – 22000 particles/m^3 at delta of Manas river in China.[12] It is clear that microplastic contamination in the environment in general as well as in waters and sediments in particular has been greatly addressed by researchers in the world. However, there have been several studies carried out in Vietnam with different concentrations of microplastic recorded, ranging from 1542 to 2024 particles/kg dry sediment at Sau and Dau beach – Vung Tau[13] to 9238 particles/kg dry sediment at Da Nang beach,[14] or from 0.35 particles/m^3 water in Cua Luc bay - Quang Ninh, 2.522 particles/m^3 water in To Lich river – Ha Noi[13] to 269693 – 863005 particles/m^3 water in downstream areas of Day river.[15]

Quy Nhon is a coastal city with several advantages to develop tourism activities as well as maritime activities through Quy Nhon seaport. Along with such advantages, the coastal areas of Quy Nhon city have been greatly affected by the wastes with noticable amount of plastic waste generated from these activities as well as from the daily activities of the city's residents. Therefore, a few projects have been implemented such as the UN-GEF 2 project operated by the Quy Nhon City Women's Union in the period of 2020 - 2022 to reduce plastic waste in coastal communes and wards in Quy Nhon Bay.[16] For the successful implementation of such community project, it is essential to find scientific evidence to prove when implementing the project. For that reason, we conducted this study to give the baseline assessment on the level of microplastic contamination in the coastal areas of Quy Nhon city as well as make initial speculation about the origin of microplastics in the studied areas.

2. STUDY SITES AND METHODS

2.1. Study sites

The study area is Quy Nhon beach and corresponding coastal waters. Quy Nhon beach runs along Xuan Dieu and An Duong Vuong streets, Quy Nhon city, Binh Dinh province. This is a place for playing and swimming of residents in Quy Nhon city as well as tourists. According to statistics in April 2019,[16] the total population of Quy Nhon city was 290,053 people, with a density of 1,013.8 people/km^2. The daily human activities as well as the development of coastal tourism services, operation of Quy Nhon seaport, or fishing activities have caused certain pressures on the coastal environment.

The sites selected to collect water and sediment samples are along Quy Nhon beach, including D1 (13.7710^{0}N. 109.2448^{0}E), D2 (13.7671^{0}N. 109.2310^{0}E), D3 (13.7597^{0}N. 109.2219^{0}E) and D4 (13.7465^{0}N. 109.2145^{0}E) (Figure 1). D1 is located nearby Quy Nhon seaport and restaurants along Xuan Dieu street. D2 is also nearby restaurants, in addition of the regular wastewater drain from the city and affected from some fishing activities of local residents. D3 is the site less affected than others, separated from street by a park. D4 is located nearby a big hotel and is a place to play and swim for tourists and local residents. In addition, D4 is also affected by fishing activities and the regular wastewater drain from the city.

Figure 1. Sampling sites

2.2. Methods

2.2.1. Sampling

Sediments and surface waters were collected in May 2021 at 4 study sites D1, D2, D3 and D4 along the Quy Nhon beach, from the Quy Nhon seaport to Ghenh Rang (Figure 1). For sediment samples, we used a tube with the diameter of 6cm and the height of 5cm to collect 5 subsamples within an area of 100 m^2, then combined them into a homogeneous sample; sediment samples were collected at the sand layer of 5cm from the surface in the intertidal zone. For water samples, the plankton net with a diameter of 50 cm and mesh size of 80 µm and a flowmeter were used to collect and calculate the collected water volume; a small boat was used to pull the net at low tide at waters about 50-100 m far from the shore. At each site, 3 subsamples were collected, and then mixed into a homogenous sample. Sediment and water samples were stored in glass containers and transported to the laboratory for later analysis.

2.2.2. Sample treatment and analysis

The water samples were treated and analysed according to the method of Emilie *et al.*[13] Firstly, each sample was filtered using the sieve with mesh size of 1 mm to discharge litters such as plants, grass but microplastics with size from 1 to 5 mm were taken and put on GF/A filters for later analysis. After filtered, the water sample was poured into the glass vessel, then added 1 g SDS and put in an incubator at temperature of 50 ^{0}C for 24 hours. Next, sample was added 1 ml of Biozym SE and 1 ml of Biozym F and placed in the incubator at 40 ^{0}C for 48 hours. Then, 15 ml H_2O_2 30% was added to the sample put in the incubator at 40 ^{0}C for 48 hours. After being treated by such chemicals, water sample was taken out of the incubator and filtered using the sieve with mesh size of 250 µm; the upper part of the sieve was tranfered into a 20 ml beaker to perform the overflow process with saturated NaCl solution. Finally, the overflowed solution was filtered on 1.6 µm GF/A filters to collect microplastics. These filters were stored in the clean petri dishes with a lid for later analysis.

Each sediment sample was dried at 55 ^{0}C within 72 hours according to the method of Quynh Anh *et al.*,[14] then mixed for homogeneity and taken 10g to treat. Next steps were almost similar to water treatment but only 20 ml H_2O_2 30% (at 40 ^{0}C for 3 hours) was added to the sample after being filtered using sieve 1 mm to remove organic matter.

https://doi.org/10.52111/qnjs.2022.16304

After above steps, the GF/A filters were observed using LAXS software of the stereomicroscope Leica S9i to record and analyse microplastics. The microplastics were analysed with 3 shapes as fragment, fiber and pellet according to Emilie et al.[13] All microplastics on each filter were taken photo, measured sizes and determined colours.

As limited equipment to analyze the nature of microplastics, based on the suggestion of GESAMP[18] and Emilie *et al.*,[13] we only examined microplastics with length of 300 - 5000 μm and area of 45000 – 25000000 μm^2 to ensure high reliability.

2.2.3. Data analysis

Microsoft Excel 2013 was used to analyse data and make the figures. Data analysed included concentration, size, shape and colour of microplastics found in waters and sediments.

2.2.4. Microplastic contamination control

To ensure the reliable study results, controlling microplastic contamination from surrounding environment is necessary. During the study, we cleaned the sample analysis and treatment area using alcohol before working on samples. In addition, we followed some recommendations of GESAMP[18] such as wearing cotton lab clothes and gloves, rinsing equipment with filtered water before use, etc. Moreover, during the sample treatment or analysis process, we used a control filter for each step to examine microplastic contamination. These control filters then were observed under the stereomicroscope Leica S9i to see whether there is any microplastic contaminated.

There was only one of 8 control filters contaminated 1 microplastic during observation under the stereomicroscope.

3. RESULTS AND DISCUSSION

3.1. Microplastic concentration and shape in surface waters and sediments

Microplastic concentration in surface waters varied from 16.37 to 62.86 particles/m^3, in which the lowest was at D3 and highest at D4. Microplastic concentration in sediments was from 1700 to 3100 particles/kg dry sediment, with the highest value at D2 and the lowest value at D3 (Table 1). It can be seen that microplastic concentration was different between study sites and this can be caused by different factors including human activities. Clearly, D3 is less affected by such activities than other sites and this can be the reason explaining why microplastic concentration here is lower than that at others. In contrast, D4 is the place affected from lot of activities such as tourism, fishing and especially wastewater discharge and these can lead to the higher microplastic concentration at here compared to other sites. However, microplastic concentration in sediments at D4 was not the highest and this gives a speculation that the daily wastewater source from city is the main cause leading to the high concentration of microplastic in waters at this site. This observation is even more valid when D2 is also heavily affected by the city's wastewater as at D4 and showed the second high concentration of microplastics among the 4 study sites. Thus, it can be said that there are different sources causing microplastic contamination at study area, of which the direct wastewater source from city is one of major reasons. This is also recorded by Quynh Anh *et al.*[14] when doing the research on microplastic at Da Nang beach. Besides, other activities such as restaurant services, hotel services, or fishing, etc. can be also reasons causing microplastic contamination at our study area.

The average microplastic concentration in sediments in this study (at Quy Nhon beach) is higher than that at Sau and Dau beach – Vung Tau (with 1542 and 2024 particles/kg dry sediment respectively)[13] but lower than that at Da Nang beach (9238 particles/kg dry sediment).[14] Similarly, microplastic concentration in surface waters in this study is much higher than that at Cua Luc bay – Quang Ninh (0.35 particles/m^3) but much lower than that at To Lich river – Ha Noi (2522 particles/m^3)[13] and at downstream of Day river (269693 – 863005 particles/m^3).[15]

Based on these results, it can be seen that microplastic contamination level at study areas in Vietnam is different and this can be caused by human activities such as industrial development, tourism, etc. In general, microplastic concentration at areas much affected by human activities is higher than that at less affected ones. This was reported in the research of Rodrigues *et al.*;[9] protected seas have very low microplastic concentration, and contamination level gradually increases at urban estuary, submarine wreck and recreational marina. Therefore, big cities with lots of tourism, industrial activities, etc often have high microplastic contamination level. On the other hand, microplastic concentration in waters at seas or bays is normally lower than that at rivers. This is also convinced by results of the research of Emilie *et al.*[13]

Table 1. Concentration of microplastic in surface waters and sediments

Study sites	Microplastic concentration in surface waters (number of particles/m^3)	Microplastic concentration in sediments (number of particles/kg dry sediment)	The typical characteristics of the study sites
D1	19.35	2400	Nearby seaport and restaurants
D2	22.68	3100	Nearby restaurants; there is the regular wastewater drain from the city; there is some fishing activities
D3	16.37	1700	Less affected by human activities
D4	62.86	2400	Nearby hotel; there is the regular wastewater drain from the city; there is some fishing activities
Average	**30.32**	**2400**	

The results of this study showed that there were 2 shapes of microplastics in waters as well as sediments, that were fragments and fibers. Generally, the ratio of fibers (varied from 66.67 – 81.67% for waters and 70.59 – 95.83% for sediments) was more dominant than that of fragments (Table 2). The average ratio of fibers of 4 sites accounted for 75.51% for waters and 86.87% for sediments. The dominance of fibers is also reported in other studies such as the research of Doan Thi Oanh *et al.* (2021) (92.55 – 96.04%),[15] Quynh Anh et al. (2020) (99.2%),[14] or Filho and Monteiro (2019) (95%).[19]

Table 2. The ratio of microplastic shapes in surface waters and sediments

Study sites	Surface waters		Sediments	
	Ratio of fibers (%)	Ratio of fragments (%)	Ratio of fibers (%)	Ratio of fragments (%)
D1	66.67	33.33	87.50	12.50
D2	81.67	18.33	93.55	6.45
D3	80.70	19.30	70.59	29.41
D4	73.00	27.00	95.83	4.17
Average	**75.51**	**24.49**	**86.87**	**13.13**

https://doi.org/10.52111/qnjs.2022.16304

3.2. Size of microplastics in surface waters and sediments

The fibers in surface waters at 4 study sites mostly had the length of from 300 to 2000 µm. Of which, the length of fibers found at D1, D2 and D4 was mostly from 1000 to 2000 µm (accounting for 60.94%, 46.94% và 64.74%) while D3 had 69.57% of bifers having the length of from 300 to 1000 µm. When data were pooled from 4 study sites, the ratio of fibers with length of 1000 - 2000 µm was highest (55.12%), followed by this of fibers with length of 300 - 1000 µm (30.45%) (Figure 2).

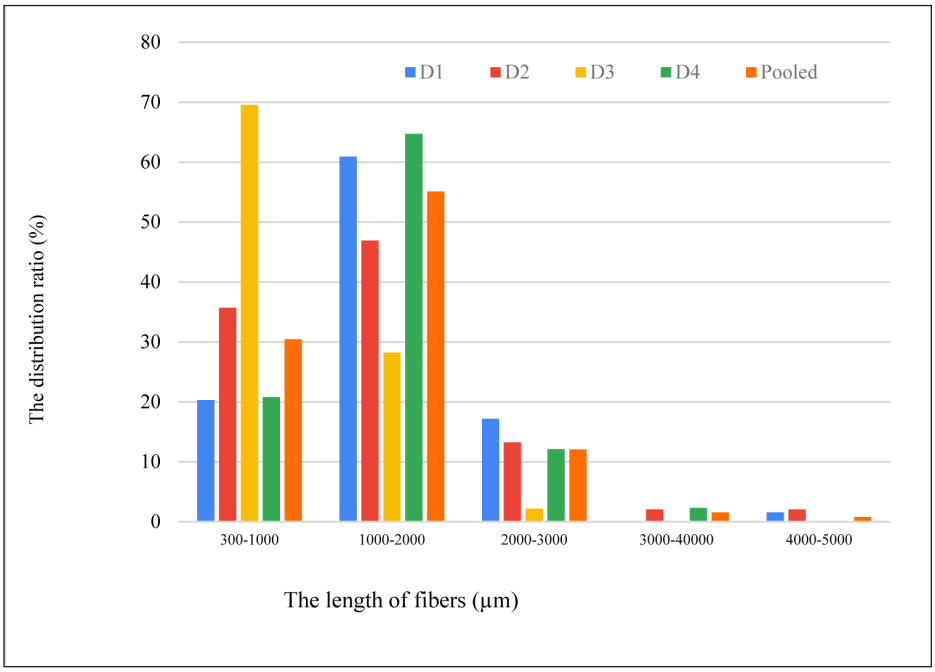

Figure 2. The distribution ratio of fibers in surface waters according to the length

The fragments in surface waters mostly had the area of 45000 – 200000 µm^2 with the ratio of 62.5%, 59.09%, 81.82% and 75% for D1, D2, D3 and D4, respectively. The pooled ratio of fragments in this size was also highest (69.77%) in size classes of microplastics found, followed by fragments in area of 200000 – 400000 µm^2 (18.6%) (Figure 3).

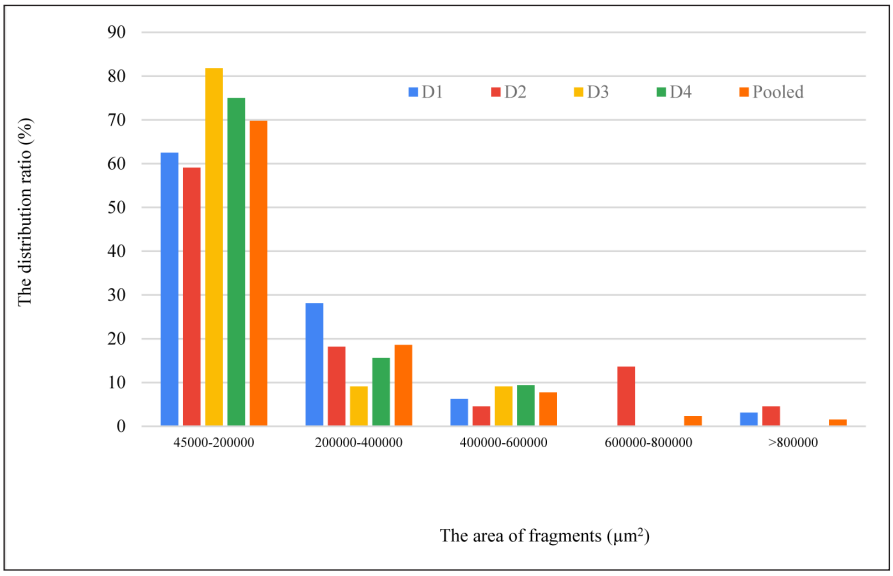

Figure 3. The distribution ratio of fragments in surface waters according to the area

Unlike in surface waters, although there was the different size distribution of fibers between study sites, the length of fibers in sediments was only predominant in class of 1000 - 2000 µm, with pooled ratio of 42.35% while other size class had almost similar ratios (Figure 4). The fragments in sediments mostly had area in 2 classes of 45000 - 200000 µm^2 and 200000 - 400000 µm^2, in which the smaller class was dominant, with pooled ratio of 90.91% (Figure 5).

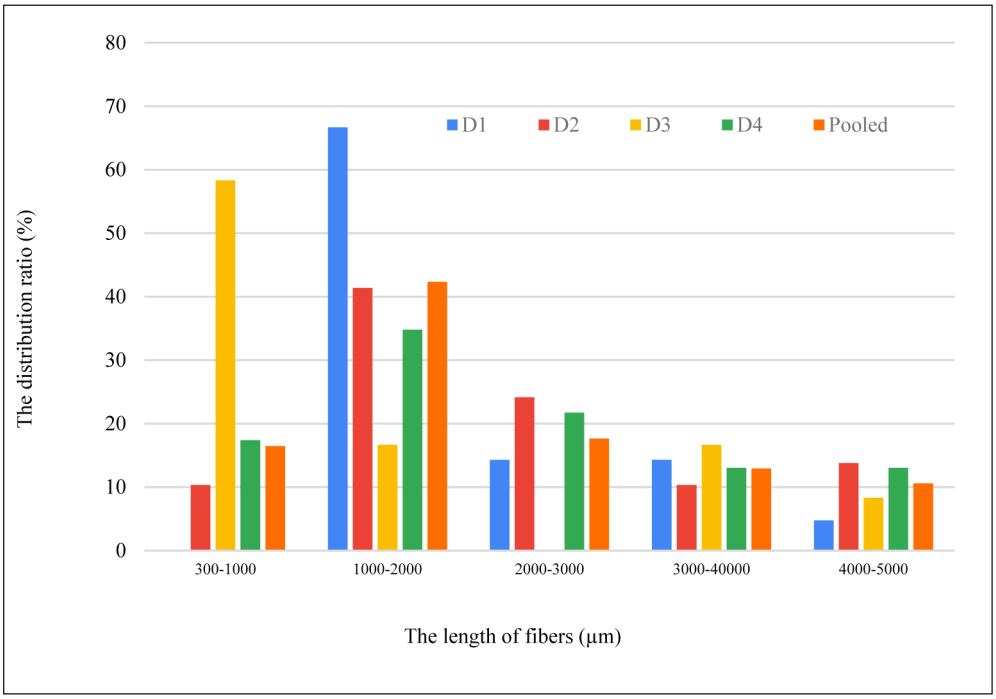

Figure 4. The distribution ratio of fibers in sediments according to the length

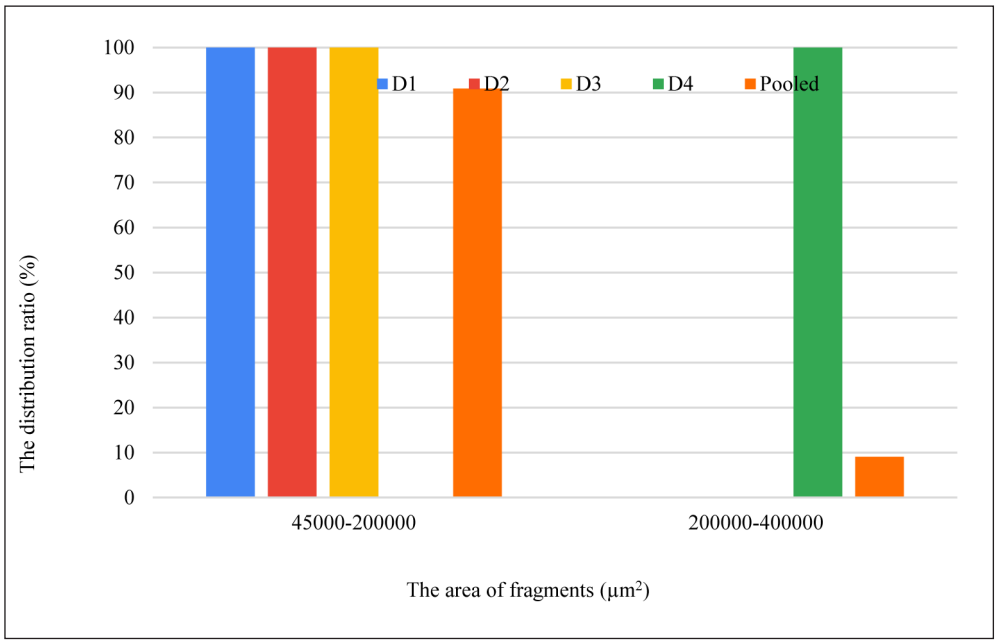

Figure 5. The distribution ratio of fragments in sediments according to the area

In general, fibers in surface waters and sediments mainly have the length of 300 - 2000 µm and fragments mostly have the area of 45000 - 400000 µm^2. Doan Thi Oanh *et al.*[15] also reported that microplastics in waters at downstream of Day river mostly had the length of 300 - 2000 µm for fibers (accounting for 78.45 - 85.71%) and area of 50000 - 400000 µm^2 (accounting for 68.72 - 87.50%) for fragments. Similarly, the dominance in number of small size-had microplastics was also recorded in other studies.[11,14] Effects of water currents and ultra violet radiation is one of factors producing small size-had microplastics.[20]

3.3. The colours of microplastics in surface waters and sediments

The colour of microplastic fibers in surface waters was quite diverse but different between study sites. Blue, white and black were major colours at D1, purple, grey and blue were predominant at D2, purple and blue dominated at D3 while white and blue were main colours at D4. When pooled for 4 sites, it can be seen that blue was most dominant (23.5%), followed by purple (23.2%) and white (17.44%) (Figure 6).

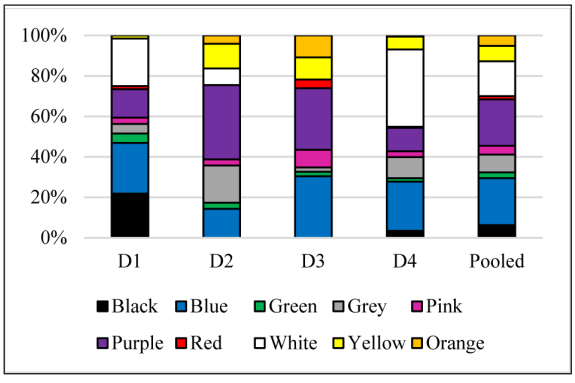

Figure 6. The colour distribution of fibers in surface waters

The color of microplastic fragments in surface waters was also very diverse and accounted for different proportions at the study sites. Specifically, white dominated at D1 and D4, white and yellow were the dominant colors at D2 while red and orange were predominant at D3. White was the most dominant color when pooled for 4 sites (44.96%), followed by yellow (14.73%) and blue (12.4%) (Figure 7).

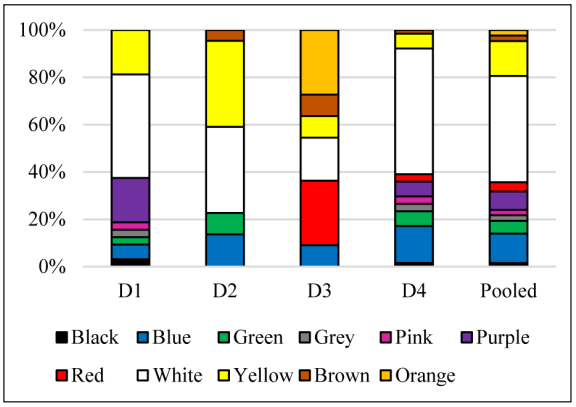

Figure 7. The colour distribution of fragments in surface waters

Regarding to colour of microplastics in sediments, because of very low proportion of fragments, we only examined fibers' colour. Generally, the colour of fibers in sediments was less diverse than that in surface waters. The distribution ratio of colours at study sites was not similar, in which white accounted for the highest ratio at D1, D2 and D4 while blue dominated at D3. Pooled for 4 sites, it can be seen that blue was predominant colour (32.32%), followed by white (30.19%) and purple (15.47%) (Figure 8).

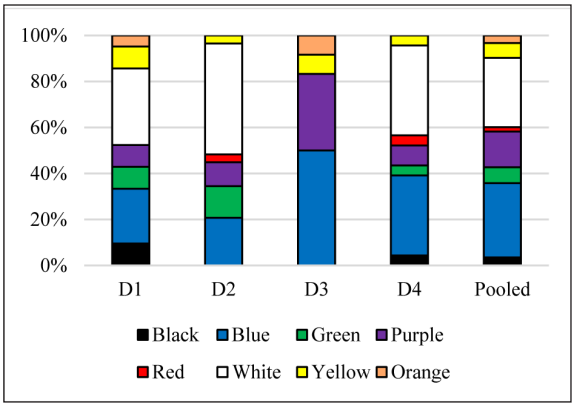

Figure 8. The colour distribution of fibers in sediments

In general, white is the dominant colour of microplastic fibers in surface waters and sediments, followed by blue and purple. Similarly, white is also the dominant colour of fragments, but followed by yellow and blue. Not similar to our results, purple is the predominant colour of microplastics in the research of Doan Thi Oanh *et al.*,[15] followed by green and blue; black and blue are the major colours in the study of Nuelle *et al.*;[21] or blue dominates, followed by

white in the study of Quynh Anh *et al.*[14] Thus, colour of microplastic in studies is different and this can be governed by different waste sources at study areas. These sources can be from garments, plastic fishing gears, packaging materials or from washing clothes through domestic wastewater.[22]

4. CONCLUSION

The microplastic concentration in surface waters varies from 16.37 to 62.86 particles/m^3 and average of 30.32 particles/m^3. The microplastic concentration in sediments is from 1700 to 3100 particles/kg dry sediments and average of 2400 particles/kg dry sediments.

The fibers found in this study mostly have the length of from 300 to 2000 µm. The fragments dominate in range of area from 45000 to 400000 $µm^2$.

Blue, white and purple are the dominant colours of fibers and white, yellow and blue dominate for fragments.

Acknowledgement

This research is conducted within the framework of science and technology projects at institutional level of Quy Nhon University under the project code T2021.703.06.

REFERENCES

1. M. A. Browne, T. Galloway, R. Thompson. Microplastic – an emerging contaminant of potential concern?, *Integrated Environmental Assessment, Management*, **2007**, *3*, 559–561.
2. S. Abidli, H. Toumi, Y. Lahbib, N. Trigui El Menif. The first evaluation of microplastics in sediments from the complex Lagoon-Channel of Bizerte (northern Tunisia), *Water Air Soil Pollution*, **2017**, *228*, 262.
3. A. Rahman, A. Sarkar, O. P. Yadav et al. Potential human health risks due to environmental exposure to microplastics and knowledge gaps: a scoping review, *Science of the Total Environment,* **2021**, *757*, 143872.
4. P. G. Ryan, C. J. Moore, J. A. Van Franeker, C. L. Moloney. Monitoring the abundance of plastic debris in the marine environment, *Philosophical Transactions of the Royal Society,* **2009**, *364*(1526), 1999-2012.
5. E. Esiukova. Plastic pollution on the Baltic beaches of Kaliningrad region, Russia, *Marine Pollution Bulletin*, **2017**, *114*, 1072-1080.
6. M. Claessens, S. D. Meester, L. V. Landuyt, K. D. Clerck, C. R. Janssen. Occurrence and distribution of microplastics in marine sediments along the Belgian coast, *Marine Pollution Bulletin*, **2011**, *62*, 2199-2204.
7. A. Mathalon, P. Hill. Microplastic fibers in the intertidal ecosystem surrounding Halifax harbor, Nova Scotia, *Marine Pollution Bulletin,* **2014**, *81*(1), 69-79.
8. Q. Qiu, J. Peng, X. Yu, F. Chen, J. Wang, F. Dong. Occurrence of microplastics in the coastal marine environment: first observation on sediment of China, *Marine Pollution Bulletin,* **2015**, *98* (1-2), 274-280.
9. S. M. Rodrigues, C. Marisa R. Almeida, S. Ramos. Microplastics contamination along the coastal waters of NW Portugal, *Case Studies in Chemical and Environmental Engineering*, **2020**, *2*, 100056.
10. M. R. Cordova, A. I. S. Purwiyanto, Y. Suteja. Abundance and characteristics of microplastics in the northern coastal waters of Surabaya, Indonesia, *Marine Pollution Bulletin,* **2019**, *142*, 183-188.
11. W. Wang, A. W. Ndungu, Z. Li, J. Wang. Microplastics pollution in inland freshwaters of China: a case study in urban surface waters of Wuhan, China, *Science of The Total Environment*, **2017**, *575*, 1369-1374.
12. G. Wang, J. Lu, W. Li, J. Ning, L. Zhou, Y. Tong, Z. Liu, H. Zhou, N. Xiayihazi. Seasonal variation and risk assessment of microplastics in surface water of the Manas River Basin, China, *Ecotoxicology and Environmental Safety*, **2021**, *208*, 111477.
13. E. Strady, Thi Ha Dang, Thanh Duong Dao, Hai Ngoc Dinh, Thi Thanh Dung Do, Thanh Nghi

Duong, Thi Thuy Duong, Duc An Hoang, Thuy Chung Kieu-Le, Thi Phuong Quynh Le, Huong Mai, Dang Mau Trinh, Quoc Hung Nguyen, Quynh Anh Tran-Nguyen, Quoc Viet Tran, Tran Nguyen Sang Truong, Van Hai Chu, Van Chi Vo. Baseline assessment of microplastic concentrations in marine and freshwater environments of a developing Southeast Asian country, Viet Nam, *Marine Pollution Bulletin*, **2021,** *162*, 111870.

14. Quynh Anh Tran Nguyen, Hoai Nhu Y Nguyen, Emilie Strady, Quy Tuan Nguyen, Mau Trinh Dang, Van Minh Vo. Characteristics of microplastics in shoreline sediments from a tropical and urbanized beach (Da Nang, Vietnam), *Marine Pollution Bulletin,* **2020**, *161*, 111768.

15. Doan Thi Oanh, Duong Thi Thuy, Nguyen Thi Nhu Huong, Hoang Thi Quynh, Le Thi Phuong Quynh, Duong Hong Phu, Le Phuong Thu, Bui Huyen Thuong. Preliminary results on microplastics in surface water from the downstream of the Day River, *Vietnam Journal of Earth Sciences*, **2021**, 1-11.

16. Quy Nhon City Women's Union. *Project Document "Improving management capacity and awareness of environmental protection of local communities, building a community model of collecting, classifying, and treating to reduce plastic waste in coastal communes and wards of Quy Nhon bay, Binh Dinh province" (UN-GEF 2)*, Project code: VNM/UNDP/2019/6, 2020.

17. Binh Dinh Statistical Office. *The 2019 Population and Housing Census implemented according to Decision No. 772/QD-TTg dated June 26, 2018 of the Prime Minister*, 2019.

18. P. J. Kershaw, A. Turra, F. Galgani (Eds.). *Guidelines for the Monitoring and Assessment of Plastic Litter and Microplastics in the Ocean,* GESAMP Joint Group of Experts on the Scientific Aspects of Marine Environmental Protection, UNEP, London, UK, 2019.

19. J. E. M. Filho, R. C. P. Monteiro. Widespread microplastics distribution at an Amazon macrotidal sandy beach, *Marine Pollution Bulletin,* **2019**, *145*, 219-223.

20. T. S. Hebner, M. A. Maurer-Jones. Characterizing microplastic size and morphology of photodegraded polymers placed in simulated moving water conditions, *Environmental Science: Processes & Impacts*, **2020**, *22*, 398-407.

21. M. T. Nuelle, J. H. Dekiff, D. Remy, E. Fries. A new analytical approach for monitoring microplastics in marine sediments, *Environmental Pollution*, **2014**, *184*, 161-169.

22. L. Su, Y. Xue, L. Li, D. Yang, P. Kolandhasamy, D. Li, H. Shi. Microplastics in Taihu Lake, China, *Environmental Pollution*, **2016**, *216*, 711-719.

TẠP CHÍ KHOA HỌC
TRƯỜNG ĐẠI HỌC QUY NHƠN

Xây dựng cấu trúc phân tử bằng thuật toán kết hợp K-Nearest Neighbor và cây tìm kiếm K-Dimension

Trương Thị Cẩm Mai[1,*], Nguyễn Trương Thành Hưng[2,3]

[1]Khoa Khoa học Tự nhiên, Trường Đại học Quy Nhơn, Việt Nam
[2]Quy Nhơn AI, FPT Software, Việt Nam
[3]Khoa Kỹ thuật, Trường Đại học Friedrich-Alexander Erlangen-Nürnberg, Đức

Ngày nhận bài:23/01/2022; Ngày nhận đăng: 14/05/2022

TÓM TẮT

Việc xây dựng các đặc tính và cấu trúc phân tử đóng một vai trò quan trọng trong nhiều lĩnh vực khác nhau, như khoa học vật liệu, cảm biến, công nghệ nano, thiết kế và khám phá thuốc. Tuy nhiên, việc xây dựng cấu trúc phân tử trên một tập dữ liệu thô, tập dữ liệu bị nhiễu và thiếu thông tin, là một nhiệm vụ đầy thách thức nhưng rất quan trọng. Thuật toán phân loại K-Nearest Neighbors (KNN) là một thuật toán lazy learning, có xu hướng tìm kiếm các điểm gần nhất cho một mục tiêu trong toàn bộ tập huấn luyện. Tuy nhiên, quá trình dự đoán của KNN khá mất thời gian. Trong khi thuật toán cây tìm kiếm K-Dimension (K-D tree) là một cây nhị phân đa chiều, có cấu trúc lưu trữ cụ thể để biểu diễn dữ liệu huấn luyện một cách hiệu quả về mặt thời gian. Từ các khía cạnh trên, trong bài báo này, chúng tôi đã thử nghiệm và đề xuất một phương pháp gọi là thuật toán cây tìm kiếm KNN-KD để xử lý tập dữ liệu thô về cấu trúc phân tử bằng cách kết hợp các ưu điểm của KNN và cây K-D.

Từ khóa: *Xây dựng cấu trúc phân tử, học máy, cây tìm kiếm K-Dimension, K-Nearest neighbors.*

**Tác giả liên hệ chính.*
Email: truongcammai@qnu.edu.vn

JOURNAL OF SCIENCE
QUY NHON UNIVERSITY

Construction of molecular structures using K-Nearest Neighbor with K-Dimension tree algorithm

Truong Thi Cam Mai[1,*], Nguyen Truong Thanh Hung[2,3]

[1]*Faculty of Natural Sciences, Quy Nhon University, Vietnam*
[2]*Quy Nhon AI, FPT Software, Vietnam*
[3]*Faculty of Engineer, Friedrich-Alexander University Erlangen-Nürnberg, Germany*

Received: 23/01/2022; Accepted: 14/05/2022

ABSTRACT

The construction of molecular properties plays a significant role in various fields, such as material science, sensors, nanotechnology, drug design, and more. However, the construction of molecular structures on a raw dataset, which is noisy and incomplete, is a challenging but crucial task. K-Nearest neighbor Classification (KNN) is a lazy learning classification algorithm with tendency to search the nearest neighbors for a target in the entire training set. Nevertheless, each step of KNN is quite time-consuming. In comparison, the K-Dimension tree (K-D tree) algorithm is a multi-dimensional binary tree, a specific storage structure for time-efficiently representing training data. To that respect, in this journal article, we conduct and propose a method called the KNN-KD tree algorithm to process a raw labeled dataset of the molecular properties by combining the advantages of the KNN and K-D tree.

Keywords: *Construction of molecular structures, machine learning, K-Dimension tree, K-Nearest neighbors.*

1. INTRODUCTION

The construction of molecular structures is one of the widespread issues where various approaches are applied using traditional chemistry formulae or mathematic computations. However, the datasets collected in experiments are noisy and incomplete for reconstructing molecular structures. In this article, a raw chemical dataset of Chemistry and Mathematics in Phase Space (CHAMPS)[1] is used to prove the performance of the geometric-based approximated machine learning model, namely the K-Dimension tree (K-D tree) in the construction of molecular structures. Significantly, this journal article will analyze, construct and visualize the molecular structures while we only use the XYZ coordinates of atoms for training the model. Consequently, this method can reduce the computing time with comparably high accuracy to rule-based methods.

1.1. Construction of molecular structures

The construction of molecular structures is a typical issue in chemistry since it impacts biomedical engineering, drug discovery, and vaccine exploration. In the real scenario, much information on the molecular properties is noisy, incomplete, and deficient.[2] As a demand, we need methods that improve the exploration of the molecular structures to deal with the shortage of information.

**Corresponding author.*
Email: truongcammai@qnu.edu.vn

https://doi.org/10.52111/qnjs.2022.16305

Various approaches to constructing the molecular structures are applied with machine learning.[3,4] However, the complexity of constructing the molecular structures increase significantly once the bonding schema is involved.[3] One of the state-of-the-art methods which achieve high accuracy on the CHAMPS dataset is a hybrid approach, namely soft graph transformer by Bosch Corporate Research and Bosch Center for AI.[5] This model processes the entire molecule one by one, simultaneously predicting each of the scalar couplings in the molecule. Instead of using a traditional graph model, their approach processes the data as a meta-graph where each atom, chemical and non-chemical bonds, namely just pairs of atoms, are included in the model, and even triplets or quads all become nodes for the graph transformer. Distance measurement between all the nodes in the graph is necessarily defined to support the model. For example, atom-to-atom distances use the actual distance between atoms. In contrast, atom-to-bond distances use the minimum distance from the atom to the two atoms in the bond, with similar extensions for triplets quads. Some other methods apply the Bidirectional Encoder Representations from Transformers (BERT) training to extract only raw coordinates instead of distance, translational and rotational invariances, such as MTM[6], Mol-BERT[7], BERT of Xin-Yu et al.[8]

Most other studies on molecular structures based on the CHAMP dataset have focused on predicting the scalar coupling constant without having a proper way to process and classify the bond information. Hence, the success rate of bond reconstruction is not good enough for further steps. Moreover, the running time of extracting information from coordinate files is time-consuming due to the enormous-size dataset. Also, some approaches applying multiprocessing may yield incorrect data. For the above reasons, a high percentage of molecule structures are not constructed correctly, which leads to the fact that various models cannot improve the accuracy in predicting the scalar coupling constants. Consequently, there is a need to create an easily customed algorithm to improve the success rate of the construction of molecular structures.

1.2. K-Nearest neighbors algorithm

K-Nearest Neighbors (KNN) algorithm is based on the distance metric function, namely Euclidean distance, to calculate the distance between the sample to be classified x and each sample in the training set, sort the calculated distance, and select the k training samples closest to the sample to be classified as the k nearest neighbors of x. If the sample belonging to a particular class of the k nearest neighbors is the majority, the representative classification sample x is classified into the category.[9]

1.3. K-D tree algorithm

K-Dimension tree (K-D tree) is a binary tree structure that recursively partitions the parameter space along the data axes, splitting it into nested orthotropic regions into which data points are filed.[10] K-D tree is a particular case of binary space partition trees. In detail, it is a space partitioning data structure for organizing points in a K-Dimensional space. A non-leaf node in the K-D tree divides the space into two parts, called half-spaces. Each subspace can be recursively divided in the same way. The left subtree of that node represents points to the left of this space, and the right subtree represents points to the right of the space. Constructing a K-D tree on a K-Dimension dataset represents a partition of the K-Dimensional space formed by the K-Dimensional dataset.

K-D trees are helpful in range searches and nearest neighbor searches. They are the most powerful data structures for small and moderate numbers of dimensions up to 20 dimensions.[11] In general, structures of the K-D tree attempt to reduce the required number of distance calculations by efficiently encoding aggregate distance information for the sample.

The construction of a K-D tree is speedy since partitioning is conducted only along the data axes. Once built, the nearest neighbor of a query point can be determined with only distance computation. Nevertheless, the K-D tree method is high-speed for low-dimensional neighbor searches. It becomes ineffective as it grows tremendous. The primary reason is that the ratio of the volume of a unit sphere in K-dimensions falls exponentially compared to a unit cube in K-dimensions. Thus at an exponential rate, many cells have to be searched within a particular radius of a query point, say for a nearest-neighbor search. Additionally, the number of neighbors for any cell grows up and eventually becomes insurmountable.[12]

1.4. Improved neighbor search algorithm using a K-D tree to find multiple k nearest neighbors (KNN-KD tree)

However, the nearest neighbor searching algorithm applied with the original K-D tree can only find one nearest neighbor. Consequently, it is necessary to adapt the original algorithm to be more efficient for searching the molecular data called KNN applied with the K-D tree (KNN-KD tree).[13,14] It can discover multiple K-nearest neighbors of a given query point instead of just finding one nearest neighbor. A bounded priority queue that stores the list of K-nearest neighbors together with their distances to the query point is applied in the adapted algorithm. The higher the priority value of the point is, the longer the distance from that point to the query point becomes. A fixed upper bound of the bounded priority queue must be defined, which is the number of nearest neighbors. The bound is used to prune tree searches, so if a series of K-nearest neighbor queries are required, it may help supply the distance to the nearest neighbor of the most recent point. Whenever a new point is added to the queue, if the queue is at capacity, the point with the longest distance to the query point is ejected from the queue.[15]

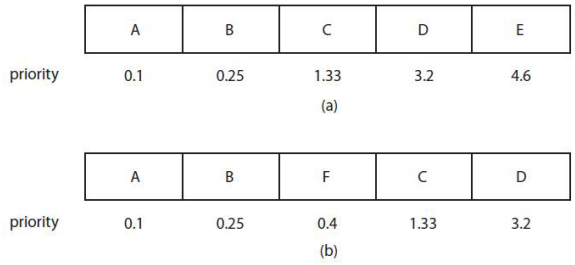

Figure 1. Bounded priority queue for KNN

For example, Figure 1a shows the nearest neighbor priority queue with the upper-bounded size of five and holds five points, from A to E. Suppose that the next nearest neighbor point to be inserted into the priority queue is the point F with the priority of 0.4. Because the maximum size of the priority queue is five, point F is inserted into the priority queue. However, point E with the longest distance to the query point q is eliminated. Figure 1b shows the resulting priority queue after point F is inserted. On the other hand, suppose that the next nearest neighbor to be inserted into the priority queue is point G with a distance of 3.5. Because the distance value of G is greater than the maximum priority element in the queue, G is not inserted into the queue.

In conclusion, there are two improvements in the KNN-KD tree algorithm from the traditional K-D tree to improve search efficiency. The first improvement is that when determining whether to look on the opposite side of the splitting hyperplane, the algorithm applies the distance from the point with the longest distance in the nearest neighbor priority queue as the radius of the candidate hypersphere.[16] The second improvement is that it reduces the time complexity from $O(n)$ to $O(n^{1-1/k}+m)$.[17]

2. DATASET AND RESEARCH METHOD

2.1. Dataset

Because the training and test splits are by molecule, no molecule in the training data will be found in the test data. The dataset contains these files as follows.

• **train.csv** The training dataset contained 4,658,147 scalar coupling observations of 85,003

https://doi.org/10.52111/qnjs.2022.16305

unique molecules. The first column (*molecule_name*) is the molecule's name where the coupling constant originates. The second (*atom_index_0*) and the third column (*atom_index_1*) are the atom indices of the atom pair, creating the coupling. The fourth column (*scalar_coupling_constant*) is the scalar coupling constant needed for predicting. All of the molecules contained five types of atoms: carbon (C), hydrogen (H), nitrogen (N), fluorine (F), and oxygen (O). There were eight distinct types of scalar coupling, including 1JHC, 1JHN, 2JHH, 2JHC, 2JHN, 3JHH, 3JHC, and 3JHH, which means that the fluorine coupling is not presented in the dataset.

- **test.csv** The test set has the same information as the train set but without the target variable, namely the scalar coupling constant. Because scalar coupling constant contains information about relative bond distances and angles, which are informative in determining the connectivity between atoms in a molecule, scalar coupling constant is not available in the test dataset to evaluate whether the model is robust to it.[18] The test dataset contained 2,505,542 scalar coupling observations of 45,772 unique molecules.

- **structures.csv** contains the molecular structure XYZ information, where the first column (*molecule_name*) is the molecule's name, followed by the index of the atom *(atom_index)*. The following column (*atom*) contains the atomic element symbols such as H for hydrogen, C for carbon, N for Nitrogen. The remaining columns include the *X*, *Y,* and *Z* cartesian coordinates.

- **dipole_moments.csv** contains the molecular electric dipole moments. These are three-dimensional vectors that indicate the charge distribution in the molecule. The first column *(molecule_name)* are molecule's names; the second to the fourth column is the XYZ components of the dipole moment.

- **magnetic_shielding_tensors.csv** contains the magnetic shielding tensors for atoms in the molecules. The first column (*molecule_name*) is the molecule name, the second column (*atom_index*) is the index of the atom in a molecule, the third to eleventh columns comprise the XX, YX, ZX, XY, YY, ZY, XZ, YZ, and ZZ elements of the tensor/matrix respectively.

- **scalar_coupling_contributions.csv** The scalar coupling constants in the train set (or corresponding files) are a sum of four terms. *scalar_coupling_contributions.csv* contains all these terms. The first column (*molecule_name*) is the name of the molecule. The second (*atom_index_0*) and third column (*atom_index_1*) are the atom indices of the atom pair. The fourth column shows the type of coupling. The fifth column (*fc*) is the Fermi Contact contribution. The sixth column (*sd*) is the Spin-dipolar contribution. The seventh column (*pso*) is the Paramagnetic spin-orbit contribution. Finally, the eighth column (*dso*) is the Diamagnetic spin-orbit contribution.

2.2. Proposed method

This journal article proposes to apply the K-Nearest Neighbour with the K-D tree (KNN-KD tree) algorithm to solve the construction of molecular structures, where the knowledge of geometry and pattern matching is utilized.

Our KNN-KD tree algorithm is split into four main steps to reconstruct the molecular structures based on the bonding schema. Every molecule is selected and restored by four steps where the XYZ cartesian coordinate of atoms structure is applied in the K-D tree. Our method solves the three kinds of coupling types.

In general, the bond length between the two atoms is approximately the sum of the covalent radii of the two atoms. Consequently, in the bonding reconstruction algorithm, the valence radii of the chemical elements are pre-defined and applied. The covalent radius is the distance from the center of the nucleus to the outermost shell of the electron, and its value may be derived from experimental measurements or calculated by theoretical models.[6] However,

these relationships are certainly not accurate due to the inconstant size of an atom but depend on its chemical environment.[19] For example, in the heteroatomic A-B bonds, ionic terms may enter.[20] Furthermore, the differential value of single, double, and triple bonds are too small to distinguish based on the distance values derived from the XYZ cartesian coordinate of atoms in the dataset. Consequently, in our algorithm, only the single bond covalent radius is manipulated to create the general bonding schema.

2.2.1. Single bond connect reconstruction

To successfully reconstruct the total bonding system, firstly, the overall molecular bonding structure must be created. The background of single bond connect reconstruction is based on the bond length comparison. In detail, each time, a pair of XYZ cartesian coordinates of two atoms in a specific molecule is put into the K-D tree structure in the three-dimensional geometry. To be more easily understandable, a random molecule, *dsgdb9nsd_000007*, is analyzed.

Table 1. The XYZ cartesian coordinate of the molecule *dsgdb9nsd_000007*

index	atom	x	y	z
0	C	-0.0187	1.5256	0.0104
1	C	0.0021	-0.0039	0.0019
2	H	0.9949	1.9397	0.0029
3	H	-0.5421	1.9236	-0.8651
4	H	-0.5252	1.9142	0.9000
5	H	0.5255	-0.4019	0.8775
6	H	-1.0115	-0.418	0.0095
7	H	0.5086	-0.3924	-0.8876

Table 1 shows that the molecule *dsgdb9nsd_000007* has eight atoms inside, which is two carbon atom and six hydrogen atoms. With the XYZ cartesian coordinate, it is easy to outline the position of every atom inside the molecule in the three-dimensional geometry, as illustrated in Figure 2. Still, there is no connection between these atoms in the dataset, namely the bonding schema. The approach is to search for all possible connections to create single chemical bondings from an atom to others. Since the valence of each atom is not provided, the standard valence is used as the default value. Also, any atom with zero available bonding is rejected. With the molecule *dsgdb9nsd_000007*, the algorithm starts with the first atom of hydrogen because the processing order beginning with the hydrogen avoids a butadiene-like molecule.

Based on the K-D tree query, the nearest atom is chosen by distance. At first, the K-D tree finds the nearest atom to a selected atom. For the spatiotemporal interpolation for the *dsgdb9nsd_000007* data, a three-dimensional K-D tree has been constructed to find the K-nearest neighbors. Figure 3 illustrates the K-D tree built from eight atomic points of *dsgdb9nsd_000007* data alongside its index. Atom C at *i=1* is the root point because it is the median point on the x-axis and splits the atomic points dataset into two groups. The first left branch group with points whose x-axis values are less than or equal to the atomic root point $x_{C[1]}$. While the other right branch group with points whose x-axis value is greater than $x_{C[1]}$. The split at the atomic root point is visualized in Figure 4. The red line is the splitting line according to the x-axis.

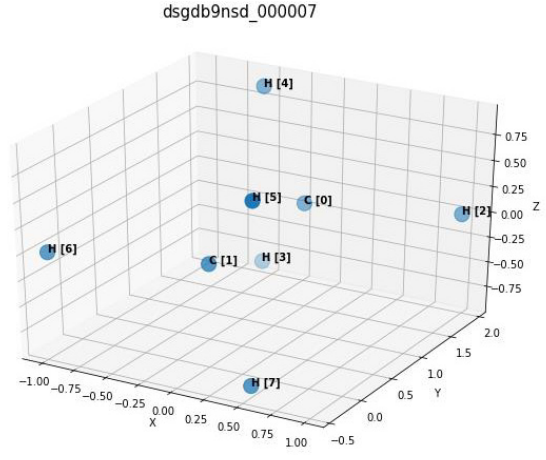

Figure 2. Eight atoms of the molecule *dsgdb9nsd_000007* in the XYZ cartesian coordinate system.

https://doi.org/10.52111/qnjs.2022.16305

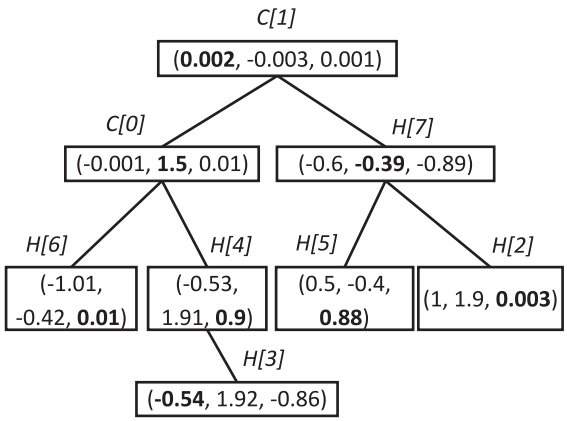

Figure 3. Visualization of the K-D tree structure constructed from 8 atomic points. Each square contains the XYZ cartesian coordinate with its *atom[index]*.

Then, to continue building the K-D tree for the molecule *dsgdb9nsd_000007*, recursively build the K-D tree in the right and the left half-space in Figure 4 by splitting at the atomic point hydrogen *(i=7)* of the right half-space and hydrogen (*i=4)* of the left half-space. The reason is that both mentioned atomic points are the median point according to the y-axis, and splitting remained atomic data point horizontally through it. Continuing partition recursively to completion will result in the entirely constructed K-D tree, as illustrated in Figure 5. The blue line is the splitting line according to the y-axis, while the green line is the splitting line according to the z-axis.

From the entirely constructed K-D tree, the K-D tree query has been implemented to get the array list of ordered atoms index relying on the distance from the selected atom point. Since the ordered atoms list of the molecule *dsgdb9nsd_000007* is: *['H', 'H', 'H', 'H', 'H', 'H', 'C', 'C']*, we start with the atom H at *i=2*. For each atom, the K-D tree query returns the nearest neighbor according to the distance. Based on the entirely constructed K-D tree structure in Figure 5, the atom C at *i=1* (C[1]) as the root is taken as an example. Atom C[1] becomes the query point in the K-D tree structure. The C[1] query point continually traverses all nodes inside its branch then creates its sphere where the radius is the distance from C[1] to the current nearest node. Next, we check whether the sphere crosses any coordinate axis, backtrack to the intersected branch, and measure the distance to find the more current nearest node. We repeatedly measure, create the new sphere, and check the intersected area until the nearest node is found. In this case of C[1], the atom hydrogen with *i=6* (H[6]) becomes the nearest neighbor, which is shown in Figure 6. The distance from C[1] to H[6] is 1.09495347.

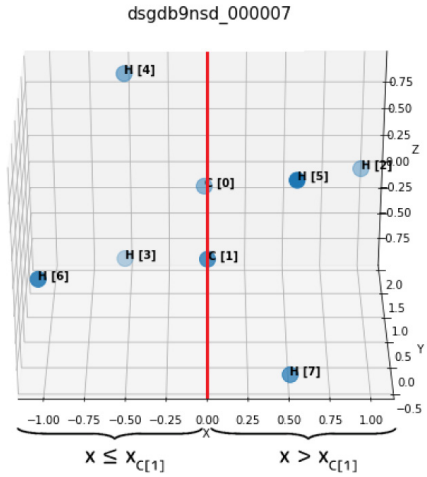

Figure 4. Visualization of splitting the atomic points into two groups according to the x-axis at atom C *(i=1)*.

After finding out H[6] as the nearest node of C[1], if there is no bond yet between those two atoms and the connection between them certainly exists once, the algorithm continues to compare the calculated distance between them to the predicted bonding distance. In addition, the number of nearest nodes taken into consideration is based on the valence of the element. If the valence value is larger than the number of atoms in a specific molecule, the maximum number of atoms is used. For example, the valence of C is 4, and then the four nearest nodes are taken to measure the distance.

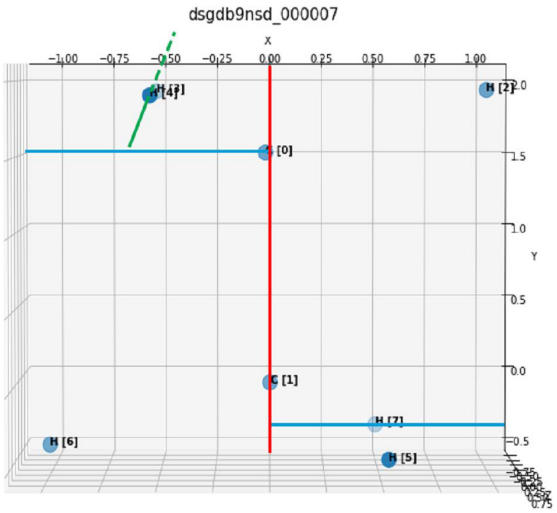

Figure 5. An entirely constructed K-D tree applies to the molecule *dsgdb9nsd_000007*

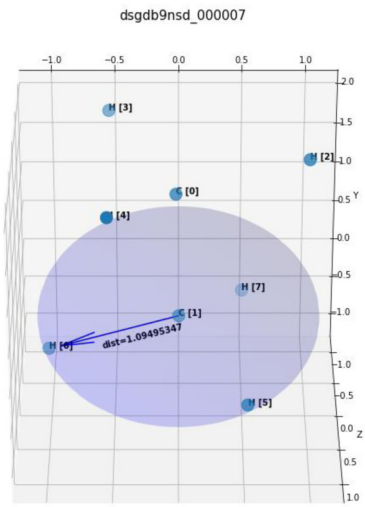

Figure 6. The nearest neighbor of atom C *(i=1)* is the atom H *(i=6)* with the *dist=1.09495347*.

The predicted bonding distance between them is measured as the sum of the bond length of each atom. In this case, only atoms with the measured distance in the 20% expected distance or closer are kept. Then, we check whether both atoms have remaining valence or not and continue decreasing the remaining valence and creating a new bond. If any of them has zero remaining valences, we mark both atoms as leaves. The function continues running until all nodes are marked as leaves. In the end, the molecule *dsgdb9nsd_000007* is constructed as in Figure 7. Based on the fully bonding reconstructed structure of *dsgdb9nsd_000007*, it is relatively easy to figure out that the chemical formula is Ethane (C_2H_6), all connected by single bonds.

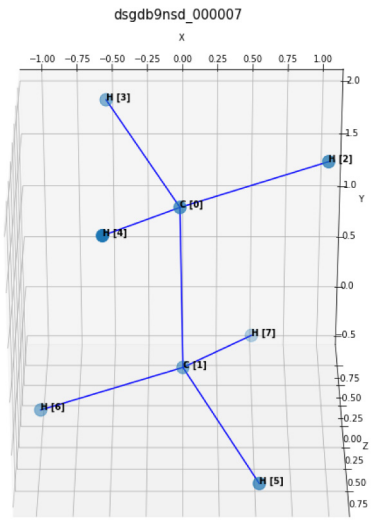

Figure 7. Fully bonding reconstructed *dsgdb9nsd_000007* molecule

2.2.2. n-bond connect greedy reconstruction

After successfully reconstructing the single bonding, the next step is rebuilding n-bond connections. Even though there is a calculated table of bond length for the double bond and triple bond, the accuracy and the consistency of the bonding connection are low. For example, the C atom has various variations in CC bond lengths that can be reasonably explained on the basis of hybridization being the primary factor. When atoms with lone pairs are involved, it appears necessary to introduce electron delocalization effects.[21] As a consequence, the bond length and bond angles do not provide a reliable measure of carbon hybridization. Any atom whose valence is greater than 1 can potentially share two or three pairs of electrons with another atom. The n-bond connect reconstruction is applied for any molecule having any remaining available valence, which is not yet connected to other atoms. The molecule *dsgdb9nsd_000005* is a typical example for this case because after applying the single bond connect reconstruction, its total remaining available valence is 4. The structure data of molecule *dsgdb9nsd_000005*

https://doi.org/10.52111/qnjs.2022.16305

are listed in Table 2. Both atom C and atom N have two remaining unconnected bonds. Especially, atom C is marked as a leaf due to its connection to atom H, which has zero valence.

The idea of solving the n-bond connection is to link the atoms by electron pair bonds until each atom has a full octet based on the Lewis structure for compounds. While there are remaining atoms marked as leaves with available valence, the algorithm will add as many bonds as possible between atoms having any available valence. Every atom is taken into consideration one by one. Until any of them has remaining valences, the algorithm will mark both atoms as leaves. The greedy algorithm is also applied to make a locally optimal choice at each stage. If any atoms still have a remaining available valence, the algorithm will check each key according to these bonding keys. Then, the bond will be added to as many as possible between a pair of atoms that have an available valence. With the greedy algorithm, it is possible to entirely reconstruct the double bond and triple bond of molecules.

Table 2. The XYZ cartesian coordinate of the molecule *dsgdb9nsd_000005*

index	atom	x	y	z
0	C	-0.0133	1.1324	0.0082
1	N	0.0023	-0.0191	0.0019
2	H	-0.0278	2.1989	0.0141

To better understand how the implemented algorithm works, there is a visualization of the bonding schema of the molecule *dsgdb9nsd_000005*. As can be seen from Figure 8, the bonding between atom C at *i=0* (C[0]) and atom H at *i=2* (H[2]) is colored black, which means the single bond. Since the H[2] is marked as a leaf, so does the C[0]. Next, the algorithm solves for the bonding between C[0] and atom nitrogen at *i=1* (N[1]). After running the n-bond connect greedy reconstruction, the triple bond between C[0] and N[1] is constructed as the red line. All atoms in the molecule have no available valence left. Hence, the double bond and triple bond reconstruction algorithm is assumptively successful.

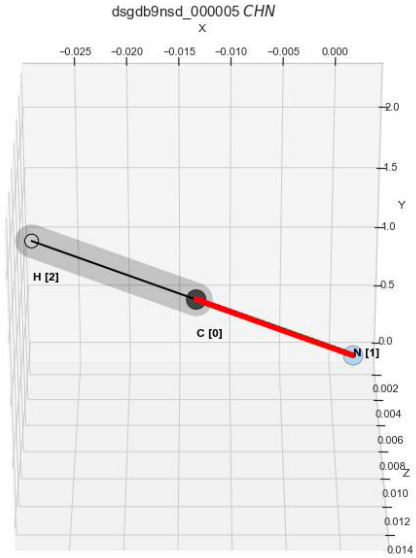

Figure 8. Fully bonding reconstructed *dsgdb9nsd_000005* molecule. The black line presents a single bond, and the red line presents the triple bond

2.2.3. Ionized radical search

After successful n-bond reconstruction, there are still many molecules without the completed bonding structure due to the ionization. The possible ionized groups which can be formed from H, C, N, F, and O in the dataset are Carboxyle (COO^-) and Ammoniumyl (NH_3^+). The idea of searching ionic bonds is initially to look for covalent bonds with remaining valence on some atoms where these covalent bonds are processed n-bond connection. For example, to find the ionic group NH_3^+, it is necessary to search for the disconnected NH_3. However, for the ionic group COO^-, we need to find the CO group with one available bond connected to an O atom.

To better understand the radical ionic search algorithm, the molecule *dsgdb9nsd_000271* is taken into consideration because it has both ionic group COO^- and NH_3^+ in its structure. After pre-processing, the molecule *dsgdb9nsd_000271* is identified as Alanine with the chemical formula $C_3H_7NO_2$. After processing with the ionic radial

search algorithm, the structural result of the molecule *dsgdb9nsd_000271* is visualized in Figure 9.

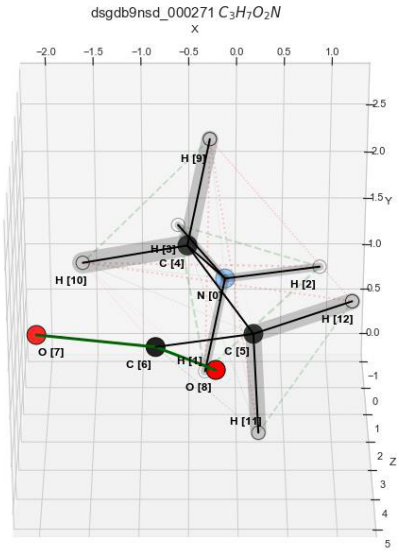

Figure 9. Fully bonding reconstructed *dsgdb9nsd_000271* ($C_3H_7NO_2$) molecule. The black line presents the single bond, the green line presents the double bond, and the red line presents the triple bond

2.2.4. Ring search

Besides reconstructing the bonding schema, the ring of atoms inside a particular molecule should be considered. The reason for identifying the chemical ring is to easily distinguish the correct chemical formula of a specific molecule. For instance, the molecule *dsgdb9nsd_000017* is one of the remarkable molecules containing a ring inside itself. The reason this molecule is more specific than the other is that the chemical formula formed from its atoms can be three different compounds.

Table 3. The XYZ cartesian coordinate of the molecule *dsgdb9nsd_000017*

index	atom	x	y	z
0	C	0.0153	1.4176	0.009
1	C	1.2648	0.6492	-0.0066
2	O	-0.0002	-0.0077	0.002
3	H	-0.3176	1.8859	0.9348
4	H	-0.3353	1.8958	-0.9039
5	H	1.8324	0.5626	-0.9319
6	H	1.8501	0.5527	0.9068

The approach of the algorithm to identify the ring of a particular molecule and its order is to apply the network graph to search for a cycle graph. The minimum cycle basic algorithm supports this approach since searching for the chemical ring is equivalent to finding the minimal cycle basic in a graph where the graph is the bonding structure. It is a cycle basic for which the total weight, in other words, the length for an unweighted graph, of all the cycles is minimum. The graph is split into connected subgraphs. The idea behind the minimum cycle basic algorithm is to use an all-pairs shortest paths (APSP) algorithm as a subroutine. Then, Dijkstra's algorithm is used for APSP computation. In other words, the graph of the bonding structure will be analyzed to find the shortest ring in a molecule.

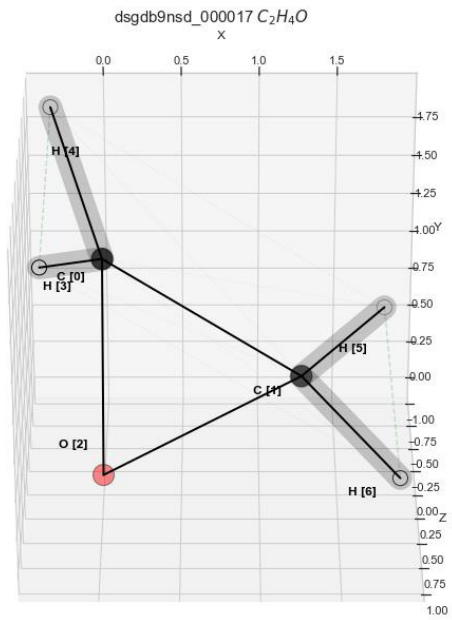

Figure 10. Fully bonding reconstructed *dsgdb9nsd_000017* molecule (C_2H_4O). The ring is between C, O, and C

3. RESULTS AND DISCUSSION

3.1. Results

After we apply the KNN-KD tree algorithm in the construction of molecular structures, we get 45772 unique molecules built from the test set and 85003 unique molecules built from the train set. After constructing the bonding type, there are 17 bonding types.

https://doi.org/10.52111/qnjs.2022.16305

The number of built molecules is equal to the initial number of molecules in the dataset, which means it is likely that there is no failure in the reconstruction algorithm. However, there is a high possibility that some molecules are not correctly handled according to the order of atoms or the bonding types. That is why there should be a proper evaluation to determine the success rate of the bonds reconstruction algorithm.

To evaluate the success rate of our KNN-KD tree algorithm, we propose to compare the output results to the result computed by OpenBabel, which is a chemical toolbox designed to search, analyze, convert, or store data from molecule modeling, chemistry, solid-state materials, biochemistry, or related areas.[22] Besides that, we conduct another baseline to test the accuracy of the KNN-KD tree algorithm. The second evaluation is to calculate the bond type consistency based on the distribution of bond length.

3.1.1. Evaluate by pairwise comparison versus OpenBabel

The pairwise comparison is applied to evaluate the calculated bonding type related to the bonding distance between two atoms and whether they are significantly different from one another. A pairwise-comparison trial included a pair of scalar coupling with its bonding type and the bonding distance between atoms. We derive results from the OpenBabel toolbox with the CHAMPS dataset and compare them with results computed by our KNN-KD tree algorithm. Any pair having a different bond type or a significant difference in the distance value between two atoms is set as an error, which is considered to be larger than 0.01.

Table 4 shows that there are 31927 scalar coupling observations of 2064 unique molecules marked as the error, which accounts for 2.4% of total processed molecules in the train set. At the same time, there are 17692 scalar coupling observations of 1150 unique molecules flagged as the error, which occupies around 2.5% of total processed molecules in the test set.

Table 4. The comparison table between our method and OpenBabel

Dataset	Test set	Train set
Unique molecule	45772	85003
Inconsistent unique molecule	1150	2064
Unconsistency percentage	2.5%	2.4%

3.1.2. Evaluate by bond type consistency distribution

Each bonding pair is grouped by its different bonding valence for both the train and test datasets. So, it is more understandable to analyze the distribution of bonding types over the distance between atoms. The computation of bond type consistency based on the bond length is applied. Each bonding pair is grouped by its different bonding valence for both the train and test datasets. So, it is more understandable to analyze the distribution of bonding types over the distance between atoms.

As can be seen from Figure 14, the train and test set match well for the relative distribution of bond length. The train and test should be the same for the prediction of the scalar coupling constant. The number of bonds also builds the distributions, which peak at a different bond distance. This is consistent with the expected behavior that the more bonds, the further distance between two atoms.

Table 5. The successful rate of bond reconstruction according to coupling types

Dataset	Coupling type	Running time	Successful rate
Train set	1JHC	111s	100.00%
	1JHN	141s	100.00%
	2JHC	241s	99.98%
	2JHH	336s	100.00%
	2JHN	379s	99.88%
	3JHC	491s	99.97%
	3JHH	600s	99.96%
	3JHN	655s	99.94%
Test set	1JHC	702s	100.00%
	1JHN	717s	100.00%
	2JHC	768s	99.99%
	2JHH	817s	100.00%
	2JHN	839s	99.90%
	3JHC	896s	99.98%
	3JHH	951s	99.96%
	3JHN	980s	99.96%

The distribution of the 1.0 CC, 2.0 CC, and 3.0 CC is a perfect example of very well separated distributions. Adding the COO^- handling improved a lot of things by separating the previous 1.0 CO bimodal distribution into two well-defined peaks, one for 1.5 CO and the second for 1.0 CO. Consequently, some other bimodal distributions like 1.0 CN, which decreased in 6.5% of bonds, can be expected to be resolved the same way if needed. Based on the calculated distribution, the running time of the implemented algorithm, together with the success rate, can be derived in Table 5.

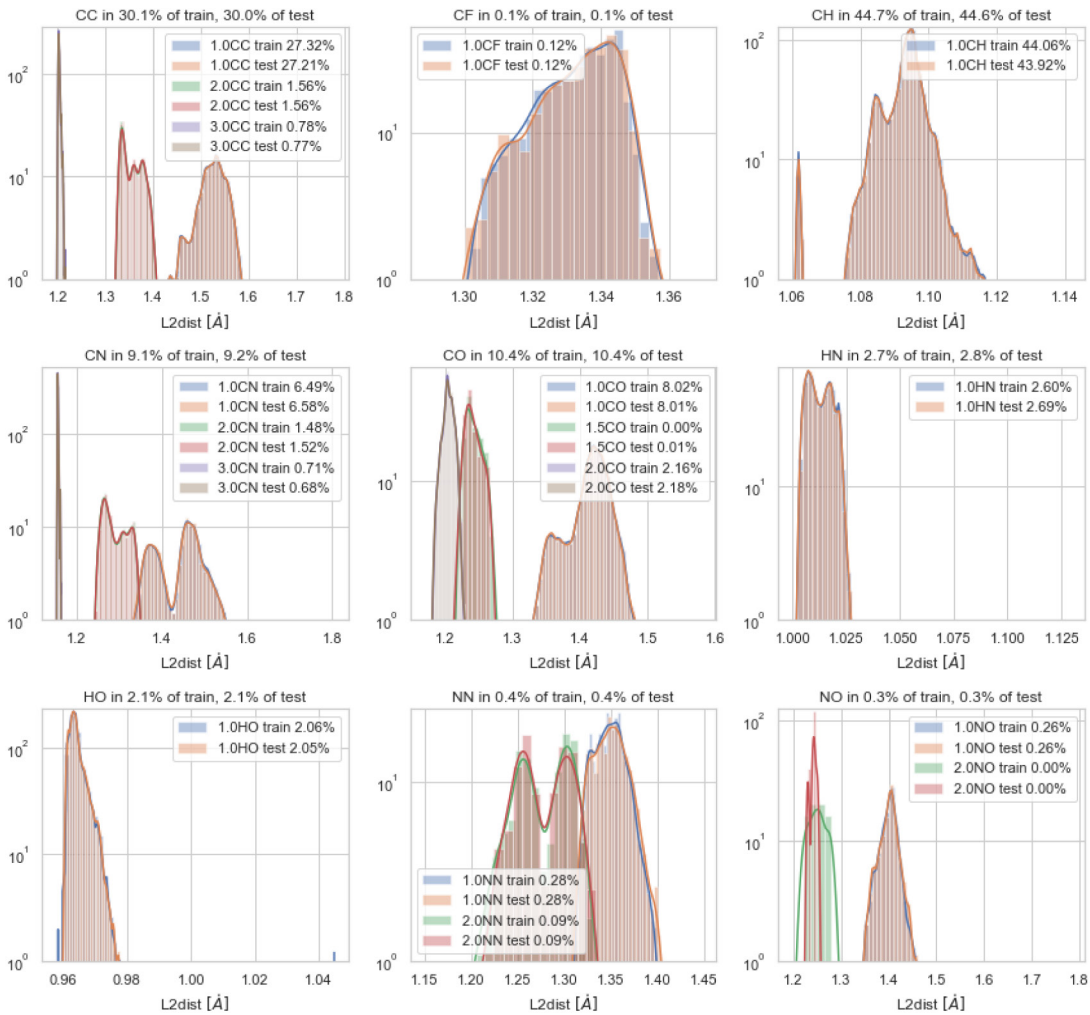

Figure 11. The diagram of bond length by atom pair and number of bonds. The line illustrates the distribution of each bond type in the train/test set

https://doi.org/10.52111/qnjs.2022.16305

3.2. Discussion

Our results can be improved by applying other systems. The initial algorithm calculates the distance between atoms based on the XYZ cartesian system. However, according to some research, this representation is not stable. Each coupling pair is located at a different point in space, and two similar coupling sets would have significantly different XYZ positions. So, instead of using coordinates, another system is considered. In this system, initially, each pair of atoms is taken as two first core atoms. The distance of the center between each pair needs to be calculated. Then, all n-nearest atoms to the center, which exclude the first two atoms, are required. Any two closest atoms become the third and the fourth core atoms. Finally, the distances from four core atoms to the rest of the atoms and to the core atoms are calculated as well. By using this representation, each atom's position can be described by four distances from the core atoms. This representation is not only stable for rotation and transition but also suitable for pattern-matching. So, by taking a sequence of atoms together with describing each by four distances and atom type and looking up for the same pattern, we can find similar configurations and detect the scalar coupling constant.

4. CONCLUSION

This research of analyzing and visualizing the molecular properties based on the KNN-KD tree algorithm has confirmed that our method can successfully construct the structure of molecules with a comparable result to rule-based methods. The findings also revealed that taking some additional datasets into account can improve the success rate of constructing the molecular structures, such as dipole interactions, magnetic shielding, and potential energy, Mulliken charges.[23–25] With the benchmark studies, the advantages and disadvantages of some data structures, which are also used for distance calculation, are presented. With our KNN-KD tree algorithm in the construction of molecular structures, utilizing models to predict the scalar coupling constants has become much more straightforward and correct. These facts motivate us to conduct and investigate the relationship between atoms in a particular molecule in the future further.

In conclusion, this research makes the following contributions: 1) proposing a geometric-based approximated machine learning model, namely the KNN-KD tree in the construction of molecular structures only with XYZ coordinates of atoms for training the model. Unlike other data structures for distance calculation, our method reduces the pre-processing time, single query time and computational resources in various essential chemistry fields such as biomedical engineering, drug discovery, and vaccine exploration. 2) visualizing the molecular structure based on the bonding schema, which was built by our KNN-KD tree algorithm, to give a better understanding and representational figures. 3) leveraging the force field method in molecular modeling because it can be extended to estimate the forces and potential energy of a system of atoms.

Our future works concern a more in-depth analysis of particular mechanisms and new proposals to try different methods. Although the results of the proposed algorithm are reasonable, there is still room for improvement. There are some features and some additional datasets that are not accounted for that likely have a significant effect on each different bonding type. The algorithm may take dipole interactions, magnetic shielding, potential energy, and Mulliken charges into account to improve the accuracy.

REFERENCES

1. Predicting molecular properties, <https://kaggle.com/c/champs-scalar-coupling>, accessed 21/01/2022.
2. X. Yang, Y. Wang, R. Byrne, G. Schneider, S. Yang. Concepts of artificial intelligence for computer-assisted drug discovery, *Chemical Reviews,* **2019**, *119*(18), 10520-10594.

3. K. Hansen, F. Biegler, R. Ramakrishnan, W. Pronobis, O. A. von Lilienfeld, K. - R. Müller, A. Tkatchenko. Machine learning predictions of molecular properties: accurate many-body potentials and nonlocality in chemical space, *Journal of Physical Chemistry Letters*, **2015**, *6*(12), 2326-2331.

4. K. Gubaev, E. V. Podryabinkin, A. V. Shapeev. Machine learning of molecular properties: locality and active learning, *The Journal of Chemical Physics,* **2018**, *148*(24), 241727.

5. boschresearch/BCAI_kaggle_CHAMPS, <https://github.com/boschresearch/BCAI_kaggle_CHAMPS>, accessed 21/01/2022.

6. A. Yoshimori. Prediction of molecular properties using molecular topographic map, *Molecules,* **2021**, *26*(15), 4475.

7. J. Li, X. Jiang. Mol-BERT: An effective molecular representation with BERT for molecular property prediction, *Wireless Communications and Mobile Computing,* **2021**, *2021*, e7181815.

8. X. - Y. Yu, R. Fu, P. - Y. Luo, Y. Hong, Y. - H. Huang. Construction and prediction of antimicrobial peptide predicition model based on BERT, <https://jasonyanglu.github.io/files/lecture_otes/%E6%B7%B1%E5%BA%A6%E5%AD%A6%E4%B9%A0_2020/Project/Construction%20and%20Prediction%20of%20Antimicrobial%20Peptide.pdf>, accessed 13/02/2022.

9. J. C. Bezdek, S. K. Chuah, D. Leep. Generalized K-nearest neighbor rules, *Fuzzy Sets and Systems* **1986**, *18*(3), 237-256.

10. J. L. Bentley. Multidimensional binary search trees used for associative searching, *Communication of the ACM,* **1975**, *18*(9), 509-517.

11. J. S. Beis, D. G. Lowe. *Shape indexing using approximate nearest-neighbour search in high-dimensional spaces*, In Proceedings of IEEE Computer Society Conference on Computer Vision and Pattern Recognition, 1997, 1000-1006.

12. M. Otair. Approximate K-nearest neighbour based spatial clustering using K-D tree, *International Journal of Database Management Systems***, 2013**, *5*(1), 97-108.

13. Nguyen Truong Thanh Hung. *Analyzing and visualizing chemical molecular properties using K-Dimension tree algorithm*, BA thesis, 2020.

14. M. Muja, D. G. Lowe. Scalable nearest neighbor algorithms for high dimensional data, *IEEE Transactions on Pattern Analysis and Machine Intelligence*, **2014**, *36*(11), 2227-2240.

15. G. S. Iwerks, H. Samet, K. Smith. - *Continuous K-nearest neighbor queries for continuously moving points with updates*, Proceedings 2003 VLDB Conference, Freytag, San Francisco, 2003, 512-523.

16. A. J. Broder. Strategies for efficient incremental nearest neighbor search, *Pattern Recognition,* **1990**, *23*(1), 171-178.

17. W. Hou, D. Li, C. Xu, H. Zhang, T. Li. *An advanced K-nearest neighbor classification algorithm based on KD-tree*, 2018 IEEE International Conference of Safety Produce Informatization (IICSPI), 2018, 902-905.

18. M. Tafazzoli, M. Ghiasi. New karplus equations for 2JHH, 3JHH, 2JCH, 3JCH, 3JCOCH, 3JCSCH, and 3JCCCH in some aldohexopyranoside derivatives as determined using nmr spectroscopy and density functional theory calculations, *Carbohydrate Research,* **2007**, *342*(14), 2086-2096.

19. R. D. Shannon. Revised effective ionic radii and systematic studies of interatomic distances in halides and chalcogenides, *Acta Crystallographica Section A*, **1976**, *32*(5), 751-767.

20. Z. Li, C. Bommier, Z. S. Chong, Z. Jian, T. W. Surta, X. Wang, Z. Xing, J. C. Neuefeind, W. F. Stickle, M. Dolgos, P. A. Greaney, X. Ji. Mechanism of Na-Ion storage in hard carbon anodes revealed by heteroatom doping, *Advanced Energy Materials,* **2017**, *7*(18), 1602894.

21. D. R. Lide. A survey of carbon-carbon bond lengths, *Tetrahedron,* **1962**, *17*(3), 125-134.

https://doi.org/10.52111/qnjs.2022.16305

22. N. M. O'Boyle, M. Banck, C. A. James, C. Morley, T. Vandermeersch, G. R. Hutchison. Open babel: An open chemical toolbox, *Journal of Cheminformatics,* **2011**, *3*(1), 33.

23. M. Riad Manaa, H. A. Ichord, D. W. Sprehn. Predicted molecular structure of novel C48B12, *Chemical Physics Letters,* **2003**, *378*(3), 449-455.

24. Z. Rinkevicius, J. Vaara, L. Telyatnyk, O. Vahtras. Calculations of nuclear magnetic shielding in paramagnetic molecules, *Journal of Chemical Physics,* **2003**, *118*(6), 2550-2561.

25. V. P. Spiridonov, N. Vogt, J. Vogt. Determination of molecular structure in terms of potential energy functions from gas-phase electron diffraction supplemented by other experimental and computational data, *Structural Chemistry,* **2001**, *12*(5), 349-376.

TẠP CHÍ KHOA HỌC
TRƯỜNG ĐẠI HỌC QUY NHƠN

Nghiên cứu lý thuyết cấu trúc và độ bền của sulfamethoxazole hấp phụ trên bề mặt rutile TiO_2 (001)

Ngô Thị Hồng Nhung[1], Nguyễn Tiến Trung[2], Nguyễn Ngọc Trí[2,*]

[1]Khoa Sư phạm, Trường Đại học Quy Nhơn, Việt Nam
[2]Phòng thí nghiệm Hóa học tính toán và mô phỏng, Khoa Khoa học tự nhiên, Trường Đại học Quy Nhơn, Việt Nam

Ngày nhận bài:23/03/2022; Ngày nhận đăng: 14/05/2022

TÓM TẮT

Trong những năm gần đây, sự hiểu biết về các quá trình trên bề mặt vật liệu là chủ đề quan tâm đối với các nhà khoa học. Giai đoạn hấp phụ quan trọng đối với những nhìn nhận xa hơn về các tương tác bề mặt và các phản ứng quang xúc tác. Trong nghiên cứu này chúng tôi sử dụng các tính toán lý thuyết phiếm hàm mật độ để khảo sát sự hấp phụ sulfamethoxazole (SMX) trên bề mặt rutile TiO_2 (001) (r-TiO_2). Các kết quả chỉ ra rằng quá trình SMX hấp phụ trên r-TiO_2 là khá mạnh với năng lượng hấp phụ khoảng -51 kcal.mol^{-1} thu được tại phiếm hàm vdW-DF2. Các cấu hình hấp phụ được làm bền chủ yếu bởi các tương tác tĩnh điện giữa nhóm >S=O với các vị trí Ti_{5f}. Bên cạnh đó, các liên kết hydro kiểu C/N-H···O_b được đánh giá như sự bổ sung quan trọng trong việc làm bền các phức. Các phân tích AIM và sự chuyển mật độ điện tích khẳng định sự tồn tại và vai trò của các tương tác bề mặt trong quá trình hấp phụ.

Từ khóa: *Sulfamethoxazole, rutile-TiO_2 (001), DFT, phiếm hàm vdW.*

**Tác giả liên hệ chính.*
Email: nguyenngoctri@qnu.edu.vn

JOURNAL OF SCIENCE
QUY NHON UNIVERSITY

Theoretical investigation on structure and stability of sulfamethoxazole adsorbed on the rutile TiO_2 (001) surface

Ngo Thi Hong Nhung[1], Nguyen Tien Trung[2], Nguyen Ngoc Tri[2,*]

[1]Faculty of Pedagogy, Quy Nhon University, Vietnam
[2]Laboratory of Computational Chemistry and Modelling, Faculty of Natural Sciences, Quy Nhon University, Vietnam

Received:23/03/2022; Accepted: 14/05/2022

ABSTRACT

In recent years, the understanding of processes on material surfaces has drawn considerable interest from scientists. The adsorption stage is important for further insights into surface interactions and photocatalytic reactions. In this study, we use density functional theory computations to investigate the adsorption of sulfamethoxazole (SMX) molecules on the rutile-TiO_2 (001) surface (r-TiO_2). Results show that the process of SMX adsorbed on r-TiO_2 is quite strong with an adsorption energy of -51 kcal.mol^{-1} obtained at vdW-DF2 functional. The adsorption configurations are stabilized mainly by electrostatic interactions between >S=O group and Ti_{5f} sites. Besides, the C/N-H···O_b hydrogen bonds are evaluated as an important addition in stabilizing complexes. The AIM and charge density transfer analyses confirm the existence and role of surface interactions in the adsorption process.

Keywords: *Sulfamethoxazole, rutile-TiO_2 (001), DFT, vdW functional.*

1. INTRODUCTION

Photocatalysts have recently emerged as attractive interests and are widely applied in energy, environmental, and health fields because of their significant properties. Semiconductor materials were evaluated as an efficient approach in advanced photocatalytic processes.[1] It is noticeable that TiO_2 is one of the potential candidates and is commonly used for photocatalysis.[2] Besides, the rutile-TiO_2 (001) found considerably upon the rutile phase formation is regarded as a highly reactive, photocatalytic facet.[3-5] However, this facet has not been wholly investigated about reactions or interactions on its surface before.

In addition, sulfamethoxazole (SMX) is a wide-board antibiotic and widely used for bacterial infections. The existence of their residues in aquatic environments significantly affects to life and growth of organisms.[6,7] The removal of polluted compounds is thus paid more attention by scientists. In previous reports, materials based on TiO_2 were investigated to remove various organic pollutants, especially for antibiotics.[8-11] Further, adsorption is critical in complex processes on material surfaces,

* *Corresponding author.*
Email: nguyenngoctri@qnu.edu.vn

https://doi.org/10.52111/qnjs.2022.16306

including photocatalysis, sensing, and storage. Understanding of surface interactions plays an essential role in evaluating the adsorption ability and reaction mechanism.[12]

Recently, computational chemistry methods have been applied for evaluating and understanding surface phenomena.[13] Using quantum chemical calculations clarified the intermolecular interactions between molecules and material surfaces such as TiO_2.[14,15] Significantly, including van der Waals forces in computations provided a better evaluation of the adsorption ability of molecules on material surfaces.[16] However, the origin and role of surface interactions between compounds containing >S=O functional groups such as sulfamethoxazole (SMX) with material surfaces, such as rutile-TiO_2 (001) facet (r-TiO_2), have not been examined entirely yet. Hence, in this work, we use quantum chemical computations to investigate the adsorption of SMX on r-TiO_2 to gain insights into the surface interactions.

2. COMPUTATIONAL DETAILS

The SMX molecule, r-TiO_2 structures, and adsorption configurations are optimized using density functional theory (DFT). The vdW-DF2 functional is used to include van der Waals forces in calculations.[17] The kinetic cut-off energy is set up at 500 eV with a 10^{-5} eV convergence index. The Brillouin zone is sampled at the Gamma center with the k-point mesh of *2 x 2 x 1*. The model slab (a = b = 18.38 Å, c = 30.00 Å) is designed with a vacuum space of 15 Å to ignore boundary interactions. The adsorption energy (E_A) is calculated by expression:

$$E_A = E_C - E_M - E_S.$$

Where E_C, E_M, E_S are energy values of optimized structures for complexes, SMX molecule, and r-TiO_2, respectively. Besides, the interaction and deformation energies are computed as follows:

$$E_I = E_C - E_M^* - E_S^*; E_{DM} = E_M^* - E_M; E_{DS} = E_S^* - E_S.$$

Here, E_I is the interaction energy. E_{DM} and E_{DS} are deformation energy values for molecule and surface. E_M^* and E_S^* are the single-point energy values of isolated SMX and r-TiO_2 in the optimized complexes. These calculations are performed by the VASP program.[18] Besides, the characteristics such as molecular electrostatic potential (MEP) map, deprotonation enthalpy (DPE), and proton affinity (PA) at sites of SMX molecule are considered at the B3LYP/6-31G(d,p) level of theory and carried out by the Gaussian 09 program.[19] The existence and strength of surface interactions are determined by the atoms-in-molecules (AIM) theory and charge density transfers at the B3LYP/6-31G(d,p) level.[20] Moreover, the hydrogen bond energy (E_{HB}) is computed from electron density potential (V(r)) through AIM analysis and followed by the expression: $E_{HB} = 0.5\ V(r)$.[21]

3. RESULTS AND DISCUSSION

3.1. Optimized structures

Performing the optimization of the geometrical structures, we obtain four stable adsorption configurations denoted by **S1**, **S2**, **S3**, and **S4**, as shown in Figure 1.

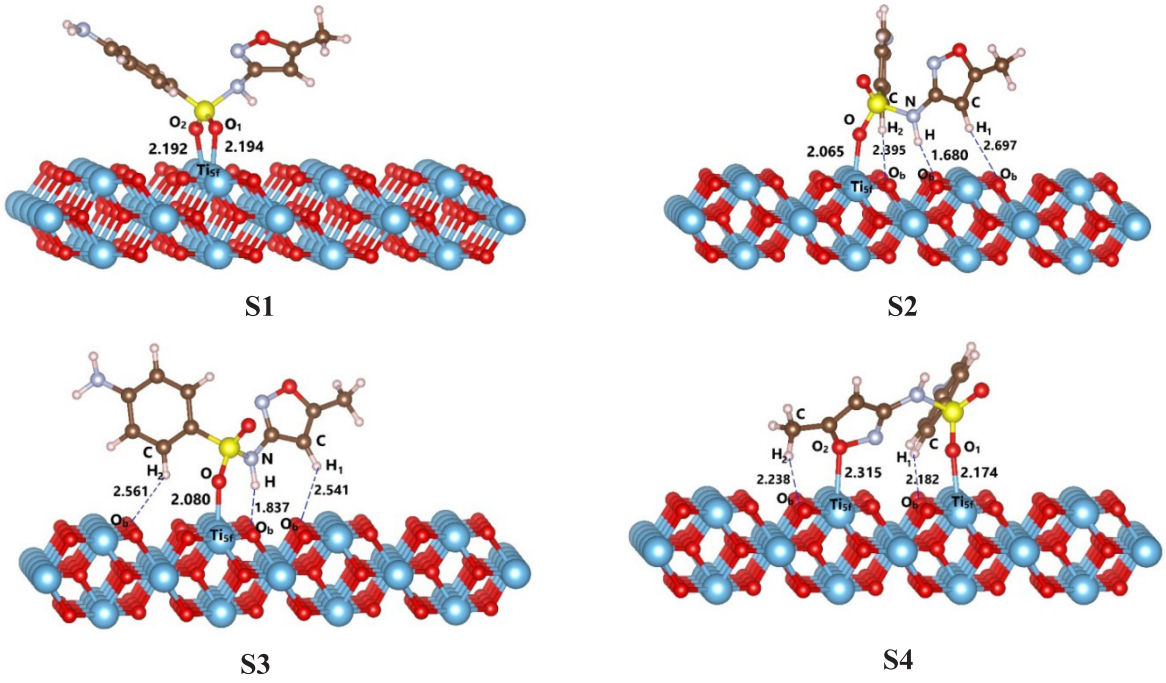

Figure 1. The stable configurations of adsorption of SMZ on r-TiO_2 (distances in Å)

The intermolecular distances of Ti_{5f}···O, H···O_b contacts are in the ranges of 2.065 - 2.315 Å, 1.680 - 2.697 Å, respectively. These values are smaller than the total of van der Waals radii of atoms involved in interactions. The bonding angels between C/N-H···O_b and S-O···Ti_{5f} contacts range of 129.75 - 168.23° and 131.11 - 168.26°, respectively. The bond length changes in forming intermolecular interactions for C/N-H, S-O are also examined. Accordingly, the bond elongations of 0.011 - 0.037 Å, 0.033 - 0.049 Å, and 0.001 - 0.004 Å are found for S-O, N-H, and C-H bonds. Besides, the adhesion of SMX onto r-TiO_2 is arranged horizontally. The electrostatic interactions appear at the high negative/positive charge density sites of >S=O and Ti_{5f} in configurations similar to recent reports.[22] These results are consistent with the formation of geometrical structures of other molecules adsorbed on TiO_2 surfaces.[14-16,22] Consequently, the stability of adsorption configurations depends on the Ti_{5f}···O, H···O_b interactions in a horizontal arrangement of SMX on r-TiO_2.

3.2. Energy aspects

The adsorption, interaction, and deformation energies for the stable configurations and monomers are observed at vdW-DF2 functional as gathered in Table 1.

Table 1. The energy aspects of the adsorption configurations (in kJ.mol^{-1})

	E_A	E_I	E_{DS}	E_{DM}
S1	-167.3	-215.0	29.9	17.9
S2	-190.4	-237.6	25.7	21.5
S3	-187.7	-220.8	13.9	19.2
S4	-214.4	-247.5	22.7	10.4

The calculated results imply that the E_{ads}, E_{int} values are in the range of -167.3 to -214.4, -215.0 to -247.5 kJ.mol^{-1}, respectively, and decrease similarly in the order of **S1 > S3 > S2 > S4**. Therefore, **S4** is the most stable complex, and **S1** is the less stable one. It is noted that **S4** is stabilized by two Ti_{5f}···O interactions and C-H···O_b hydrogen bonds while the stability of **S1** is contributed significantly by two Ti_{5f}···O interactions. The strength of **S2** and **S3** is based on one Ti_{5f}···O interaction and N/C-H···O_b hydrogen bonds. Hence, the stability of complexes mainly depends on Ti_{5f}···O electrostatic interactions and the essential addition of C/N-H···O_b hydrogen bonds. Besides, the adsorption of SMX on the

https://doi.org/10.52111/qnjs.2022.16306

(001) facet of rutile-TiO_2 is slightly weaker than that for other antibiotics.[14] It is due to the horizontal arrangement of these molecules on TiO_2 being more convenient than SMX. At >C=O, -COOH groups, the negative charge density is higher than at >S=O. Consequently, stable intermolecular contacts are favorably formed in these systems as compared to SMX-TiO_2.

In addition, the deformation energy is an essential factor in evaluating the interaction ability and separation of the molecule on the material surface upon the adsorption process. Table 1 shows that the deformation energy values for r-TiO_2 (E_{DS}) and SMX (E_{DM}) are ca. 13.9 - 29.9 kJ.mol^{-1}, and 10.4 - 21.5 kJ.mol^{-1}, respectively. It can be seen that a more considerable change in geometry of r-TiO_2 following the complexation in comparison to SMX. Calculated results are similar to rutile-TiO_2 (110) surface changes following the adsorption of molecules containing functional groups on its surface.[14,15,22] Particularly, the E_{DS} and E_{DM} values of rutile-TiO_2 surface and molecules in these reports are of 10.5 - 56.5 kcal. mol^{-1} and 3.3 - 54.0 kJ.mol^{-1}, respectively. Indeed, the interaction between SMX and r-TiO_2 causes slight changes of the isolated geometries for the surface and molecule upon complexation.

3.3. Existence and role of surface interactions

3.3.1. MEP analysis and DPE, PA at sites of molecules

To evaluate the formation ability of intermolecular interactions, we carried out computations on characteristics of molecules including MEP and DPE, PA at sites. The calculated results are illustrated in Figure 2 and given in Table 2.

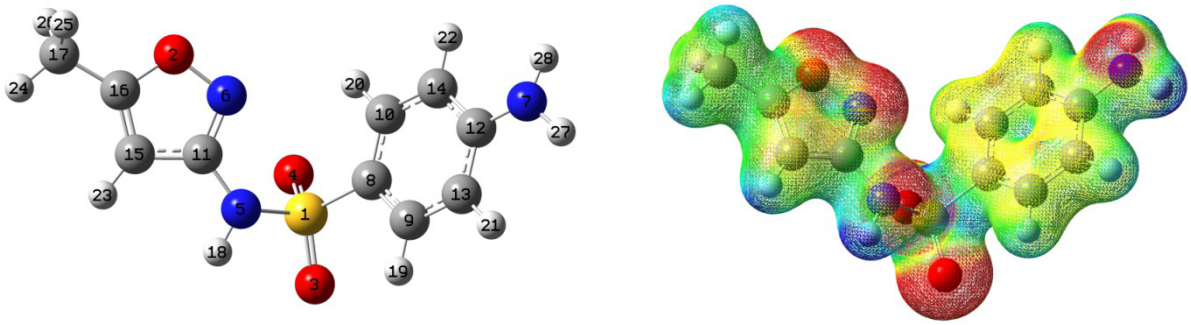

Figure 2. The optimized geometry and MEP map of sulfamethoxazole at B3LYP/6-31G(d,p) level (electron density = 0.02 au; region of -5.10^{-5} to 0.20 au)

Table 2. The deprotonation energy (DPE) and proton affinity (PA) at bonds and atoms in sulfamethoxazole at B3LYP/6-31G(d,p) level (all given in kJ.mol^{-1})

	N_5-H_{18}	N_7-H_{27}	C_{13}-H_{21}	C_9-H_{19}	C_{17}-H_{24}	C_{15}-H_{23}
DPE	1482.0	1552.7	1691.2	1689.5	1700.8	1666.5
	O_3	O_4	O_2	N_6	N_5	N_7
PA	888.7	956.0	766.1	977.0	925.9	869.4

The MEP map for sulfamethoxazole indicates that the $O_{(2,3,4)}$ and $N_{(5,6,7)}$ sites have high negative electron densities (red color regions). These sites strongly interact with positive charge regions at Ti_{5f} on r-TiO_2 to form Ti_{5f}···O attractive electrostatic interactions, especially at >S=O group. Meanwhile, the significant positive regions at H atoms (in C-H, N-H bonds) conveniently interact with the negative charge sites at O_b lying on the surface to form C/N-H···O_b stable hydrogen bonds.

As presented in Table 2, the proton affinity of atoms decreases in the order of N_6 > O_4(O_3) > N_5 > N_7 > O_2. The electrostatic interactions between O/N sites with the Ti_{5f} on r-TiO_2 are thus stable, especially at N_6 and O_4 sites. Besides, the hydrogen bonds formed between H atoms and O_b on r-TiO_2 are more favorable

at N_5-H_{18} than at N_7-$H_{28/27}$ as compared to C-H bonds. This is understood that the DPE values of N-H are smaller than those of C-H bonds (cf. Table 2). Indeed, the interactions between SMX and r-TiO_2 are favorable at the opposite regions of high charge density as well as at the sites that have strong proton affinity or slight deprotonation energy.

3.3.2. AIM analysis and electron density transfers

The characteristics of topological geometries for the first-layered structures are displayed in Figure 3 and listed in Table 3. The electron density transfers upon complexation are also displayed in Figure 4 for whole adsorption configurations.

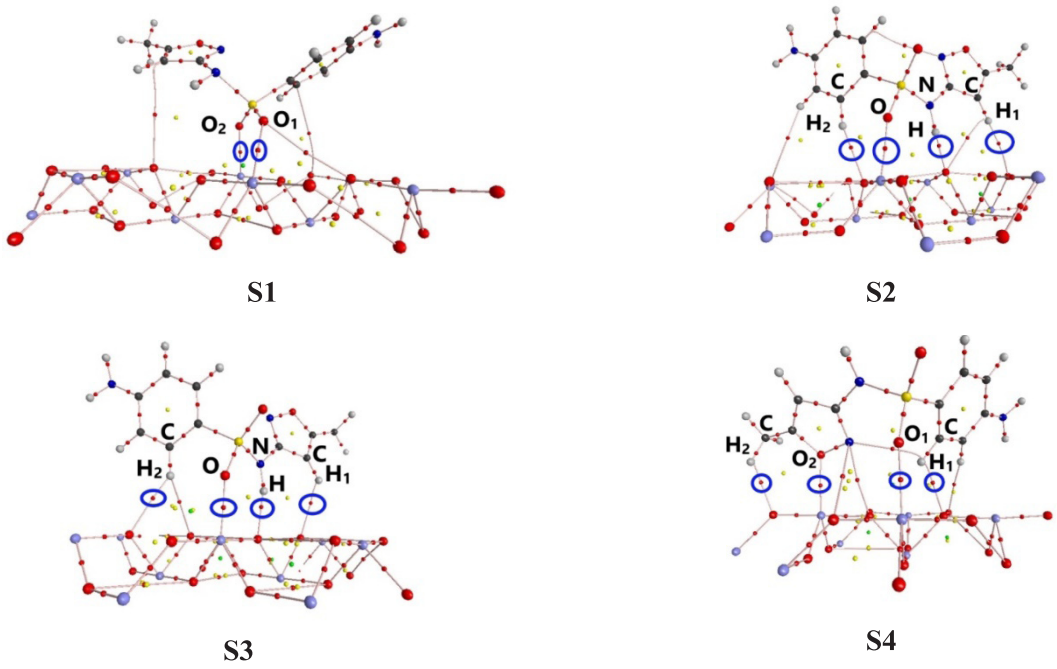

Figure 3. The topological geometries for first-layered structures of complexes

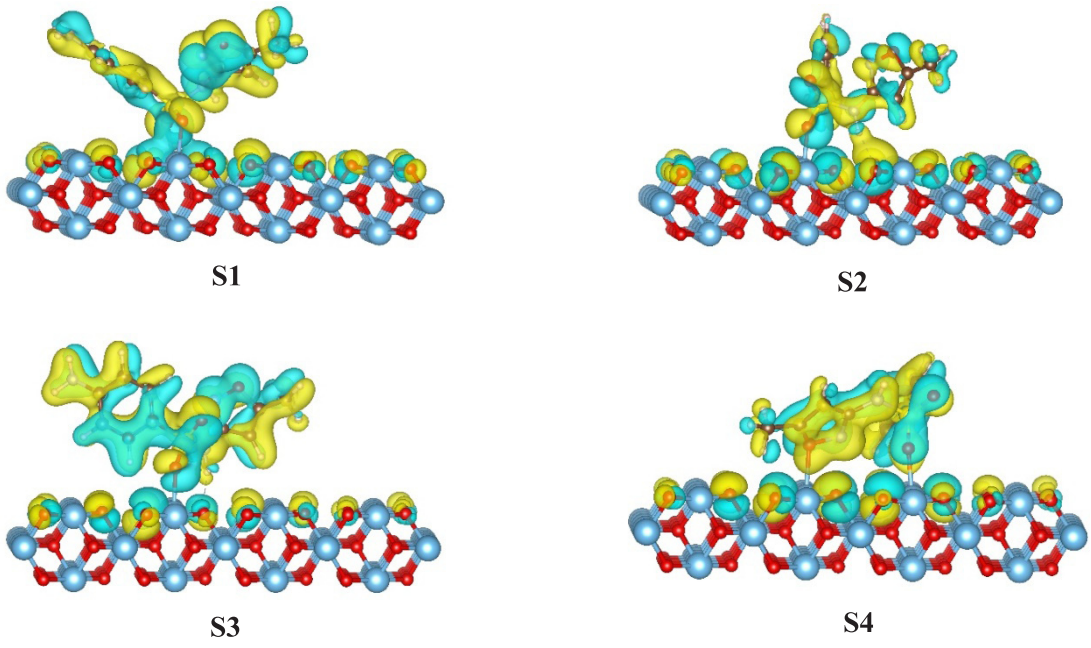

Figure 4. The charge distribution upon complexation

Table 3. The AIM analysis for structures in Fig.3 at the B3LYP/6-31G(d,p) level (ρ(r), ∇(ρ(r)), H(r) (in au); E_{HB} (in kJ.mol^{-1}))

	BCPs	ρ(r)	∇(ρ(r))	H(r)	E_{HB}
S1	$O_1\cdots Ti_{5f}$	0.046	0.265	0.005	
	$O_2\cdots Ti_{5f}$	0.046	0.264	0.005	
S2	$O\cdots Ti_{5f}$	0.064	0.373	0.002	
	$N\text{-}H\cdots O_b$	0.048	0.127	-0.008	-62.2
	$C\text{-}H_1\cdots O_b$	0.007	0.021	0.001	-4.1
	$C\text{-}H_2\cdots O_b$	0.011	0.034	0.001	-7.8
S3	$O\cdots Ti_{5f}$	0.063	0.358	0.001	
	$N\text{-}H\cdots O_b$	0.033	0.089	-0.002	-35.7
	$C\text{-}H_1\cdots O_b$	0.008	0.027	0.001	-5.1
	$C\text{-}H_2\cdots O_b$	0.009	0.029	0.001	-6.2
S4	$O_1\cdots Ti_{5f}$	0.045	0.281	0.007	
	$O_2\cdots Ti_{5f}$	0.035	0.182	0.004	
	$C\text{-}H_1\cdots O_b$	0.017	0.052	0.001	-13.9
	$C\text{-}H_2\cdots O_b$	0.019	0.065	0.002	-17.2

Figure 3 shows that the BCPs are found between $Ti_{5f}\cdots O$, $H\cdots O_b$ intermolecular contacts. As presented in Table 3, the electron density (ρ(r)) values of $Ti_{5f}\cdots O$, $H\cdots O_b$ BCPs are of 0.035 to 0.064 au, 0.007 to 0.048 au, respectively. These intermolecular contacts are thus regarded as non-covalent interactions.[20] It can be confirmed further by the slightly positive values of H(r) at most of $Ti_{5f}\cdots O$, $H\cdots O_b$ BCPs. Noticeably, the $N\text{-}H\cdots O_b$ contacts in **S2**, **S3** have negative H(r) values of -0.01 au, indicating their partly covalent nature. The large ρ(r) values at $Ti_{5f}\cdots O$ BCPs imply their high strength and significant contribution to the stability of complexes. Moreover, the hydrogen bond energy (E_{HB}) values are calculated and listed in Table 3. Accordingly, the more negative values of E_{HB} in **S2** imply the more significant contribution of hydrogen bonds to its stability as compared to **S3**, **S4**, and **S1**. The cooperation of two $Ti_{5f}\cdots O$ stable interactions and hydrogen bonds brings the considerable strength of **S4** as related to other ones. Indeed, the adsorption ability of SMZ on the (001) facet of rutile-TiO_2 is quite strong.

The electron density transfer (EDT) is one of the crucial characteristics to determine the existence and strength of intermolecular interactions. The considerable transfers of electron density in complexes lead to form stable interactions. The calculated EDT values for **S1**, **S4** are 0.057 e and 0.011 e, implying the more substantial electron density transfers from SMX to r-TiO_2 to form $Ti\cdots O$ contacts than the reverse transfers from r-TiO_2 to SMX to form $O\cdots H$ hydrogen bonds. In contrast, the EDT values for **S2** and **S3** are -0.033 and -0.012 e, indicating the more substantial electron density transfers from r-TiO_2 to SMX than the reverse transfers from SMX to r-TiO_2. Therefore, it can be suggested that the $Ti_{5f}\cdots O$ and $H\cdots O_b$ intermolecular interactions exist following the complex formation.

4. CONCLUSIONS

The stable complexes for adsorption of the SMX molecule on the rutile TiO_2 (001) surface are examined at vdW-DF2 functional. The adsorption energy of the complexes is in the range of -167.3 to -214.4 kJ.mol^{-1}. The main contribution is determined by the attractive electrostatic forces between >S=O group and Ti_{5f} site, while the vital addition of the N/C-H···O hydrogen bonds is found in stabilizing of adsorption configurations. AIM analysis indicates that the interactions between $>S{=}O\cdots Ti_{5f}$ and $N/C\text{-}H\cdots O_b$ mostly have non-covalent in nature. It is noticeable that the $C/N\text{-}H\cdots O_b$ partly covalent hydrogen bonds play a crucial addition in stabilization. Furthermore, the electron density transfers occur significantly from SMX to r-TiO_2 following the formation of the interaction. Indeed, the process of SMX adsorbed on the surface of r-TiO_2 is evaluated as chemical adsorption.

Acknowledgement

This research is conducted within the framework of science and technology projects at the institutional level of Quy Nhon University under the project code T2020.659.07.

REFERENCES

1. F. Zhang, X. Wang, H. Liu, C. Liu, Y. Wan, Y. Long and Z. Cai. Recent advances and applications of semiconductor photocatalytic technology, *Applied Sciences*, **2019**, *9*, 2489(1-43).
2. M. Huang, J. Yu, B. Li, C. Deng, L. Wang, W. Wu, L. Dong, F. Zhang, M. Fan. Intergrowth and coexistence effects of TiO_2–SnO_2 nanocomposite with excellent photocatalytic activity, *Journal of Alloys and Compounds*, **2015**, *629*, 55-61.
3. U. Diebold. Structure and properties of TiO_2 surfaces: a brief review, *Applied Physics A*, **2003**, *76*, 681-687.
4. L. Wu, Z. Wang, F. Xiong, G. Sun, P. Chai, Z. Zhang, H. Xu, C. Fu, and W. Huang. Surface chemistry and photochemistry of small molecules on rutile TiO_2(001) and TiO_2(011)-(2 × 1) surfaces: The crucial roles of defects, *Journal of Chemical Physics*, **2020**, *152*, 044702(1-11).
5. B. D. Sosnowchik, H. C. Chiamori, Y. Ding, J.-Y. Ha, Z. L. Wang and L. Lin. Titanium dioxide nanoswords with highly reactive, photocatalytic facets, *Nanotechnology*, **2010**, 21485601(1-6).
6. K. Kümmerer. Antibiotics in the aquatic environment - A review - Part I, *Chemosphere*, **2009**, *75*, 417-434.
7. J. Niu, L. Zhang, Y. Li, J. Zhao, S. Lv, K. Xiao. Effects of environmental factors on sulfamethoxazole photodegradation under simulated sunlight irradiation: kinetics and mechanism, *Journal of Environmental Sciences*, **2013**, *25*, 1098-1106.
8. C. Deiana, E. Fois, G. Martra, S. Narbey, F. Pellegrino, G. Tabacchi. On the simple complexity of carbon monoxide on oxide surfaces: facet-specific donation and backdonation effects revealed on TiO_2 anatase nanoparticles, *ChemPhysChem*, **2016**, *7*, 1-6.
9. M. Sowmiya, K. Senthilkumar. Adsorption of proline, hydroxyproline and glycine on anatase (001) surface: a first-principle study, *Theoretical Chemistry Accounts*, **2016**, *135*, 12(1-8).
10. X. Pan, Q. X. Cai, W. L. Chen, G. L. Zhuang, X. N. Li, J. G. Wang. A DFT study of gas molecules adsorption on the anatase (001) nanotube arrays, *Computational Materials Science*, **2013**, *67*, 174-181.
11. S. Manzhos, G. Giorgi, K. Yamashita. A Density Functional Tight Binding Study of Acetic acid adsorption on crystalline and amorphous surfaces of Titania, *Molecules*, **2015**, *20*, 3371-3388.
12. U. Diebold. The surface science of titanium dioxide, *Surface Science Reports*, **2003**, *48*, 53-229.
13. K. N. Jens, A. P. Frank, S. Felix and B. Thomas. Density functional theory in surface chemistry and catalysis, *Proceedings of the National Academy of Sciences of the United States of America*, **2011**, *108*, 937-943.
14. N. N. Tri, H. Q. Dai, A. J. P. Carvalho, M. T. Nguyen and N. T. Trung. Insights into adsorptive interactions between antibiotic molecules and rutile-TiO_2 (110) surface, *Surface Science*, **2021**, *703*, 121723(1-8).
15. N. N. Tri, H. Q. Dai, N. T. Trung. Insight into the adsorption of organic molecules on rutile TiO_2 (110) surface: A theoretical study, *Vietnam Journal of Chemistry*, **2018**, *56(6)*, 751-756.
16. J. T. Marcus, M. B. Peter, A. B. Roger, G.-C. Ricardo. Adsorption of organic molecules at the TiO_2(110) surface: The effect of van der Waals interactions, *Surface Science*, **2015**, *632*, 142-153.
17. K. Lee, E. D. Murray, L. Kong, B. I. Lundqvist, and D. C. Langreth. Higher-accuracy van der Waals density functional, *Physical Review B*, **2010**, *82*, 081101(1-4).
18. J. Hafner. Ab-Initio Simulations of Materials Using VASP: Density-Functional Theory and Beyond, *Journal of Computational Chemistry*, **2008**, *29*, 2044-2078.
19. M. J. Frisch et al. *Gaussian 09 (Revision B.01)*, Wallingford, CT: Gaussian, 2010.
20. R. F. W. Bader. *Atoms in molecules: A quantum theory*, Oxford: Oxford University Press, 1990.
21. I. Matta, I. Alkorta, E. Espinosa, E. Molins. Relationships between interaction energy, intermolecular distance and electron density properties in hydrogen bonded complexes under external electric fields, *Chemical Physics Letters*, **2011**, *507*, 185-189.
22. N. N. Tri, N. T. Trung. Theoretical study on adsorption of sulfamethoxazole on rutile-TiO_2 (110) surface using quantum chemical method, *Quy Nhon University – Journal of Science*, **2021**, *15(5)*, 47-54.

https://doi.org/10.52111/qnjs.2022.16306

TẠP CHÍ KHOA HỌC
TRƯỜNG ĐẠI HỌC QUY NHƠN

Bảo mật lớp vật lý cho các kỹ thuật truyền dẫn đa người dùng của mạng chuyển tiếp MIMO lớn với xử lý tuyến tính

Nguyễn Đỗ Dũng[1,*], Đào Minh Hưng[1], Võ Nguyễn Quốc Bảo[2]

[1]*Khoa Kỹ thuật và Công nghệ, Trường Đại học Quy Nhơn, Việt Nam*
[2]*Học viện Công nghệ Bưu chính Viễn thông, Việt Nam*

Ngày nhận bài: 08/05/2021; Ngày nhận đăng:13/07/2021

TÓM TẮT

Trong bài báo này, chúng tôi xem xét vấn đề truyền dẫn đa người dùng trong hệ thống chuyển tiếp nhiều đầu vào nhiều đầu ra (MIMO). Trong đó, một trạm gốc được trang bị nhiều ăng ten truyền đồng thời thông tin đến nhiều người dùng thông qua sự trợ giúp của bộ chuyển tiếp được trang bị mảng ăng ten lớn. Giao thức giải mã và chuyển tiếp (DF) được xem xét bằng cách sử dụng kỹ thuật tổ hợp tỷ lệ cực đại/ truyền tỷ lệ cực đại (MRC/MRT) hoặc kỹ thuật tiếp nhận ép về không/ truyền ép về không (ZFR/ZFT), để xử lý tín hiệu tại bộ chuyển tiếp trong điều kiện thông tin trạng thái kênh không hoàn hảo. Kết quả, các biểu thức chính xác và biểu thức xấp xỉ đạt được về tốc độ kênh người sử dụng và tốc độ an toàn rớt kênh đối với một xác suất rớt kênh an toàn cho trước. Ngoài ra, chúng tôi đã đề xuất phân tích tiệm cận trong các trường hợp đặc biệt khác nhau. Nó đã tiết lộ rằng, phần lớn tỷ lệ nghe trộm được loại bỏ khi một số lượng ăng ten bộ chuyển tiếp tiến đến vô cùng và đồng thời năng lượng truyền tại trạm gốc và bộ chuyển tiếp có thể được giảm nhỏ xuống đáng kể theo yếu tố tỉ lệ $1/\sqrt{N}$, trong khi đó vẫn duy trì được hiệu suất hệ thống an toàn. Cuối cùng, kết quả mô phỏng thể hiện tính hợp lệ trong phân tích của bài báo.

Từ khoá: *Truyền thông an toàn, MIMO đa người dùng, chuyển tiếp MIMO lớn, mạng chuyển tiếp.*

**Tác giả liên hệ chính.*
Email: nguyendodung@qnu.edu.vn

https://doi.org/10.52111/qnjs.2022.16307

JOURNAL OF SCIENCE
QUY NHON UNIVERSITY

Physical layer security for multiuser transmission techniques of massive MIMO relay networks with linear processing

Nguyen Do Dung[1,*], **Dao Minh Hung**[1], **Vo Nguyen Quoc Bao**[2]

[1]*Faculty of Engineering and Technology, Quy Nhon University, Vietnam*
[2]*Posts and Telecommunications Institute of Technology, Vietnam*

Received: 08/05/2021; Accepted: 13/07/2021

ABSTRACT

In this paper, we consider the problem of secure multiuser transmission in a massive multiple input multiple output (MIMO) relaying system, wherein a base station equipped with many antennas transmits simultaneously its message to multiuser at the destination via help of a relay equipped with massive antenna arrays. Decode and forward (DF) protocol is considered by using the maximum ratio combining/maximum ratio transmission (MRC/MRT) or zero-forcing reception/zero-forcing transmission (ZFR/ZFT) to process signals at the relay under imperfect channel state information (CSI). As a result, exact and asymptotic expressions for user rate and outage secrecy rate for a given secure outage probability of eavesdropper links are derived. Furthermore, we have proposed the asymptotic analysis in various special cases. It is disclosed that the majority of eavesdropper rates is eliminated when a number of relay antennas go to infinity, and simultaneously the transmit power at the base station and the relay can be scaled down significantly by factor $1/\sqrt{N}$ while maintaining secure system performance. Finally, numerical results confirm the validity of our analysis.

Keywords: *Secure communication, multiuser MIMO, massive MIMO relaying, relay networks.*

1. INTRODUCTION

Recently, massive MIMO system can considerably enhance the data rate and serve many users in the same time-frequency resource by utilizing hundreds of antennas simultaneously.[1,2] Massive MIMO inherits all the advantage of traditional multiuser MIMO such as improved spectral efficiency, reliability, and reduced interference. Owing to the efficient use of the very large antenna arrays, transceiver is simplified even with just simple linear processing, e.g., maximum ratio transmission (MRC) or zero forcing (ZF).[3–6] Therefore, multiple transmit antennas techniques can also be exploited for enhancement of secrecy performance. In literatures,[7,8] it was found that,
the information leakage to an eavesdropper can be fairly small and insignificant as the number of antennas goes to infinity. As discussed in the article,[9] with standard time division duplexing (TDD) mode the legitimate user obtains several orders of magnitude much larger than the received signal power at the eavesdropper. This generates a state where the secrecy rate is quite high rate to the legitimate user. Altogether, massive MIMO enables excellent physical layer security without any extra effort.

In order to assess on the physical layer security performance, the gap between the legitimate channel capacity and the wiretap channel capacity is usually determined, namely secrecy rate.[10–12] Several excellent studies have investigated relay networks into physical layer security derived the considerable improvement of the legitimate channel capacity through cooperative diversity, hence enhances secure transmission.[13,14] However, presences of eavesdroppers in wireless networks are usually typical passive in order to hide their existence. Therefore, the transmitter cannot obtain eavesdropper CSI. Besides, the quality of legitimate CSI is also a challenge due to the fact

**Corresponding author.*
Email: nguyendodung@qnu.edu.vn

https://doi.org/10.52111/qnjs.2021.16307

that there exists legitimate channel estimation error or a feedback delay.[14–16] As in the article,[17] when the CSI is obtained by using property of reciprocity in TDD model systems, it may be imperfect because of delay or pilot contamination. In this context, the concept of secrecy outage rate was also considered to evaluate the secure communication with a given probability[18,19] due to unavailability of the eavesdropper CSI. Additionally, combining multiple relay cooperative beamforming with artificial noise (AN) was adopted to enhance the legitimate signal, and simultaneously degrade the eavesdropper signal.[20–22] Topics of secure communications on physical layer security including node authentication, message integrity, and secrecy have also been considered.[23]

In general, unlike the corresponding classical cryptographic approaches which are all based on computational security, the added strength of physical layer security is that it is based on information theoretic security, in which no limitation with respect to the opponent's computational capacity is assumed and is therefore inherently quantum resistant. Physical layer security solutions emerge as competitive candidates for low complexity, low-delay and low-footprint, adaptive, flexible and context aware security schemes, leveraging the physical layer of the communications.

Note that, secrecy performance of massive MIMO relaying system under the amplify-and-forward for multiuser transmission was discussed in the article.[24] In this paper, we continue surveying the relay-assisted massive MIMO system under DF to enhance the secrecy performance which is the paper's main motivation. Specifically, we focus on considering relay schemes, including MRC/MRT and ZFR/ZFT, and taking into account the effects of second hop channel estimation for physical layer security in a massive MIMO relaying network. The main contributions of this paper are summarized as follows:

i) Based on two linear processing methods, the secure multiuser MIMO downlink transmission techniques are considered to solve the challenging issue of the short-distance between the relay and eavesdroppers, and CSI imperfect channels. As a result, novel closed-form expressions of data rate and secrecy outage rate for MRC/MRT and ZFR/ZFT, which help us employ secure performance comparison of different network and system settings and provide significant insights for system design and optimization. It is noteworthy that secure transmission performance on short-distance eavesdroppers is addressed.

ii) The multiple-antenna MIMO technique at the relay is utilized by exploiting the large-scale antenna array gain. When the number of relay antennas approaches infinity, eavesdroppers of rate have less effects on secrecy performance, and simultaneously the transmit power at the BS and the relay can be scaled by factor $1/\sqrt{N}$.

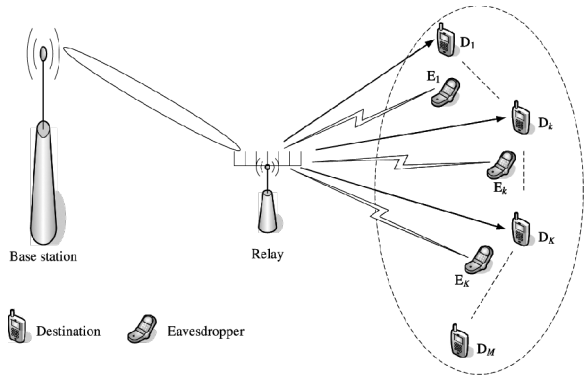

Figure 1. Relay-aided massive MIMO network.

The remainder of this chapter is organized in the following manner. In Section 2, the system model of the massive MIMO DF relaying system employing physical layer security under imperfect CSI is presented. In Section 3, we derive explicit expressions of the secrecy outage rate for both MRC/MRT and ZFR/ZFT methods, from which their secure performances in diffident cases are compared. In Section 4, we analyze asymptotic behavior of secrecy outage rate functions for typical power scaling laws in various scenarios. Numerical results are verified according to proposed schemes in Section 5. Finally, Section 6 concludes the paper.

Notation: Throughout the paper, we use upper (lower) case boldface to denote matrices (vectors). The superscripts $*$, T, and H stand for the complex conjugate, transpose, and conjugate-transpose, respectively. $\mathbf{A}_{ij}$ denotes the (i,j)-th entry of matrix $\mathbf{A}$, and $\mathbf{I}_N$ is the $N \times N$ identity matrix. We use $\mathbb{E}\{.\}$, $\|.\|$ and $\mathrm{Tr}(.)$ to denote the statistical expectation, the Euclidean norm and the trace of a matrix, respectively.

2. SYSTEM MODEL

In this section, the system model of secure multiuser downlink transmission based on relaying is introduced. Wherein, performance metrics are considered

https://doi.org/10.52111/qnjs.2022.16307

to evaluate on the secrecy characteristics of the system.

2.1. General description

In this paper, the relay strategy assisting secure multi-user downlink transmission is in Figure 1, wherein the base station (BS) is equipped with M antennas to serve corresponding single-antenna mobile destinations, M, via help of a relay (R) with N antennas. Because the system model is assumed that there is no direct path between BS and all D nodes due to a long propagation or shadowing.[25,26] Specifically, we will consider that a secure transmission downlink when K antennas at BS simultaneously send messages to desired K mobile destinations $(\mathsf{D}_1, \ldots, \mathsf{D}_K)$ with $(1 \leq K \leq M)$ in presence of K passive eavesdropper $(\mathsf{E}_1, \ldots, \mathsf{E}_K)$ either pretending to be legitimate destinations or to be idle mobile destinations.[27] We also assume that all E nodes are out of the coverage area the BS,[28,29] i.e., they are far from the BS and close to the R and D nodes. Therefore, all E nodes can only receive directly from the emitting R.

In the first phase, having K antennas transmit simultaneously their signal vector, $\mathbf{x} = [x_1, x_2, \ldots, x_K]^T$. Here, we assume that $\mathbb{E}\{|x_k|^2\} = 1$ so that P_{S} is the average transmit power per antenna at BS. The received signal at R is given by

$$\mathbf{y}_{\mathsf{R}} = \sqrt{P_{\mathsf{S}}}\mathbf{G}_{\mathsf{BR}}\mathbf{x} + \mathbf{n}_{\mathsf{R}}, \tag{1}$$

where $\mathbf{G}_{\mathsf{BR}} \in \mathbb{C}^{N\times K}$ denotes the channel matrix from BS to R. It notes that the channel matrices account for independent and identically distributed (i.i.d.) Rayleigh fading and time division duplex. More precisely, $\mathbf{G}_{\mathsf{BR}}$ can be expressed as $\mathbf{G}_{\mathsf{BR}} \triangleq \sqrt{\eta_{\mathsf{BR}}}\mathbf{H}_{\mathsf{BR}}$, where the small-scaled fading matrix $\mathsf{H}_{\mathsf{BR}} \in \mathbb{C}^{N\times K}$ has i.i.d. $\mathcal{CN}(0,1)$ elements, while factor η_{BR} is the distance-dependent path-loss random variable with variance $E\{|\eta_{\mathsf{BR}}|^2\} = \sigma^2_{\mathsf{BR}}$.

By using the linear receiver, the received signal $\mathbf{y}_{\mathsf{R}}$ at the relay is separated into K streams by multiplying it with a linear detector matrix $\mathbf{A}^T$ as

$$\mathbf{r} = \mathbf{A}^T\mathbf{y}_{\mathsf{R}}, \tag{2}$$

$$= \sqrt{P_{\mathsf{S}}}\mathbf{A}^T\mathbf{G}_{\mathsf{BR}}\mathbf{x} + \mathbf{A}^T\mathbf{n}_{\mathsf{R}}. \tag{3}$$

In particular, the k-th signal stream processed at R can be written as

$$\mathbf{r}_k = \sqrt{P_{\mathsf{S}}}\mathbf{a}_k^T\mathbf{g}_{\mathsf{BR},k}x_k + \sqrt{P_{\mathsf{S}}}\sum_{i\neq k}^{K}\mathbf{a}_k^T\mathbf{g}_{\mathsf{BR},i}x_i + \mathbf{a}_k^T\mathsf{n}_{\mathsf{R}}. \tag{4}$$

In the second phase, the relay performs linear precoding to all decoded signals, $\mathbf{x}$, in the first phase by multiplying it with a beamforming matrix $\mathbf{B}$, i.e., $\mathbf{s} = \mathbf{B}\mathbf{x}$. These signals are then broadcasted to destinations. Hence, the received $K \times 1$ signals at all D will be

$$\mathbf{y}_{\mathsf{D}} = \mathbf{G}_{\mathsf{RD}}^T\mathbf{s} + \mathbf{n}_{\mathsf{D}},$$

$$= \mathbf{G}_{\mathsf{RD}}^T\mathbf{B}\mathbf{x} + \mathbf{n}_{\mathsf{D}}. \tag{5}$$

In particular, we can write the received signal at D_k under the form of

$$y_{\mathsf{D}_k} = \mathbf{g}_{\mathsf{RD},k}^T\mathbf{b}_k x_k + \sum_{i\neq k}^{K}\mathbf{g}_{\mathsf{RD},k}^T\mathbf{b}_i x_i + n_{\mathsf{D}_k}, \tag{6}$$

where the channel matrix between the K destinations and the relay is denoted by $\mathbf{G}_{\mathsf{RD}} = [\mathbf{g}_{\mathsf{RD},1}, \mathbf{g}_{\mathsf{RD},2}, ..., \mathbf{g}_{\mathsf{RD},K}] \in \mathbb{C}^{N\times K}$. $\mathbf{G}_{\mathsf{RD}}$ can be further written as $\mathbf{G}_{\mathsf{RD}} = \mathbf{H}_{\mathsf{RD}}\mathbf{D}_{\mathsf{RD}}^{1/2}$, in which $\mathbf{H}_{\mathsf{RD}} \in \mathbb{C}^{N\times K}$ includes the i.i.d. $\mathcal{CN}(0,1)$ small-scale fading coefficients, and $\mathbf{D}_{\mathsf{RD}}$ is the large-scale fading diagonal matrix depended on distance path-loss, and i-th diagonal element of the diagonal matrix is denoted by $[\mathbf{D}_{\mathsf{RD}}]_{ii} = \sigma^2_{\mathsf{RD},i}, (i = 1, 2, \ldots, K)$. Moreover, $\mathbf{n}_{\mathsf{D}}$ and $\mathbf{n}_{\mathsf{R}}$ are the AWGN vectors at R and K destinations, respectively, with i.i.d. components following $\mathcal{CN}(0,1)$. From (4) and (6), the instantaneous received signal-to-interference-plus-noise ratio (SINR) at R with k-th stream and D_k is given by, respectively,

$$\gamma_{\mathsf{BR}_k} = \frac{P_{\mathsf{S}}\left|\mathbf{a}_k^T\mathbf{g}_{\mathsf{BR},k}\right|^2}{P_{\mathsf{S}}\sum_{i\neq k}^{K}\left|\mathbf{a}_k^T\mathbf{g}_{\mathsf{BR},i}\right|^2 + P_{\mathsf{S}}\left|\mathbf{a}_k^T\mathbf{n}_{\mathsf{R}}\right|^2}, \tag{7}$$

and

$$\gamma_{\mathsf{RD}_k} = \frac{\left|\mathbf{g}_{\mathsf{RD},k}^T\mathbf{b}_k\right|^2}{\sum_{i\neq k}^{K}\left|\mathbf{g}_{\mathsf{RD},k}\mathbf{b}_i\right|^2 + 1}. \tag{8}$$

As a result, we can obtain an achievable rate of the transmission links BS $\rightarrow$ R and R $\rightarrow$ D_k respectively as

$$\mathscr{R}_{\mathsf{BR}_k} = \log_2\left(1 + \gamma_{\mathsf{BR}_k}\right), \tag{9}$$

and

$$\mathscr{R}_{\mathsf{RD}_k} = \log_2\left(1 + \gamma_{\mathsf{RD}_k}\right). \tag{10}$$

At the same time, E_k tries to intercept information from R to D_k. Therefore, the received signal at E_k can be obtained as

https://doi.org/10.52111/qnjs.2021.16307

$$y_{\mathsf{E}_k} = \mathbf{g}_{\mathsf{RE},k}^T \mathbf{b}_k x_k + \sum_{i \neq k}^{K} \mathbf{g}_{\mathsf{RE},k}^T \mathbf{b}_i x_i + n_{\mathsf{E}_k}, \quad (11)$$

where $\mathbf{g}_{\mathsf{RE},k}$ is the channel vector between E_k and R, n_{E_k} is the AWGN with zero mean and unit covariance at E_k.

Similar to (8), we assume that the channel $\mathbf{g}_{\mathsf{RE},k}$ is obtained at k-th corresponding eavesdropper is perfect CSI. Therefore, the achievable SINR at E_k is

$$\gamma_{\mathsf{RE}_k} = \frac{\left|\mathbf{g}_{\mathsf{RE},k}^T \mathbf{b}_k\right|^2}{\sum_{i \neq k}^{K} \left|\mathbf{g}_{\mathsf{RE},k} \mathbf{b}_i\right|^2 + 1}. \quad (12)$$

From (12), the corresponding eavesdropper rate of transmission link $\mathsf{R} \to \mathsf{E}_k$ derived as

$$\mathscr{R}_{\mathsf{RE}_k} = \log_2 \left(1 + \gamma_{\mathsf{RE}_k}\right). \quad (13)$$

For secure multiuser massive MIMO relaying system, we assume that the achievable total legitimate channel rate and the achievable total eavesdropper channel rate are $\mathscr{R}_{\mathsf{D}}$ and $\mathscr{R}_{\mathsf{E}}$, respectively. From the perspective of information theory, the achievable secrecy rate region for decode-and-forward dualhop relay wiretap channel is expressed as [11,30]

$$\mathscr{R}_{\mathsf{SE}} = \left[\mathscr{R}_{\mathsf{D}} - \mathscr{R}_{\mathsf{E}}\right]^+ = \sum_{k=1}^{K} \mathscr{R}_{\mathsf{SE}_k}, \quad (14)$$

where $\mathscr{R}_{\mathsf{SE}_k}$ is the achievable secrecy rate at D_k,[31] given by

$$\mathscr{R}_{\mathsf{SE}_k} = \left[\mathscr{R}_{\mathsf{D}_k} - \mathscr{R}_{\mathsf{E}_k}\right]^+, \quad (15)$$

with $[x]^+ = \max(x, 0)$. In (15), $\mathscr{R}_{\mathsf{D}_k}$ and $\mathscr{R}_{\mathsf{E}_k}$ represent the achievable channel rate of the transmission link $\mathsf{BR}_k \to \mathsf{R} \to \mathsf{D}_k$ and $\mathsf{BR}_k \to \mathsf{R} \to \mathsf{E}_k$, respectively. Thus, we have

$$\mathscr{R}_{\mathsf{D}_k} = \frac{1}{2} \min \left(\mathscr{R}_{\mathsf{BR}_k}, \mathscr{R}_{\mathsf{RD}_k}\right), \quad (16)$$

and

$$\mathscr{R}_{\mathsf{E}_k} = \frac{1}{2} \min \left(\mathscr{R}_{\mathsf{BR}_k}, \mathscr{R}_{\mathsf{RE}_k}\right). \quad (17)$$

2.2. Performance metrics

In this paper, we assume that there is no knowledge of eavesdropper links at BS and R. Maintaining a steady secrecy rate over all realizations of fading channels is difficult since CSI eavesdroppers is unavailable. Based on the given secrecy outage probability, ζ, we take the maximum rate which is defined as secrecy outage rate, $\mathscr{R}_{\mathtt{OSE}_k}$, at D_k. Hence, we have[7]

$$\zeta = \Pr\left(\mathscr{R}_{\mathtt{OSE}_k} > \mathscr{R}_{\mathsf{D}_k} - \mathscr{R}_{\mathsf{E}_k}\right). \quad (18)$$

From (17), we can rewrite (18) as

$$\zeta = \Pr\left[\mathscr{R}_{\mathtt{OSE}_k} > \mathscr{R}_{\mathsf{D}_k} - \frac{1}{2}\log_2\left(1 + \gamma_{\mathsf{E}_k}\right)\right], \quad (19)$$

$$= 1 - F_{\gamma_{\mathsf{E}_k}}\left[2^{2\left(\mathscr{R}_{\mathsf{D}_k} - \mathscr{R}_{\mathtt{OSE}_k}\right)-1}\right]. \quad (20)$$

where $\gamma_{\mathsf{E}_k} \triangleq \min\left(\gamma_{\mathsf{BR}_k}, \gamma_{\mathsf{RE}_k}\right)$ and $F_{\gamma_{\mathsf{E}_k}}(.)$ is the cumulative distribution function (CDF) of γ_{E_k}. After we simply manipulate the expression (20), the system secrecy outage rate as a function of ζ can be derived as

$$\mathscr{R}_{\mathtt{OSE}_k} = \mathscr{R}_{\mathsf{D}_k} - \frac{1}{2}\log_2\left[1 + F_{\gamma_{\mathsf{E}_k}}^{-1}(1 - \zeta)\right], \quad (21)$$

where ${F\gamma_{\mathsf{E}_k}}^{-1}(.)$ is the inverse CDF of $F_{\gamma_{\mathsf{E}_k}}(.)$.

We consider both MRC/MRT and ZFR/ZFT schemes under practical wireless network scenarios. Specifically, the BS and R locations are fixed while all destinations serve as mobile terminals as the case considered in this paper. Therefore, the first-hop channel, $\mathbf{G}_{\mathsf{BR}}$, is considered as perfect CSI by accurately estimating. Whereas, the achieved second-hop channel, $\mathbf{G}_{\mathsf{RD}}$, is imperfect due to applying due to channel reciprocity in TDD systems and the mobility of destination nodes,[25] which leads to the channel estimation error matrix, $\hat{\mathbf{G}}_{\mathsf{RD}}$, of the actual channel matrix $\mathbf{G}_{\mathsf{RD}}$, we can write[32]

$$\mathbf{G}_{\mathsf{RD}} = \hat{\mathbf{G}}_{\mathsf{RD}} + \boldsymbol{\mathcal{E}}_{\mathsf{RD}}, \quad (22)$$

where $\hat{\mathbf{G}}_{\mathsf{RD}} = [\hat{\mathbf{g}}_{\mathsf{RD},1}, \ldots, \hat{\mathbf{g}}_{\mathsf{RD},K}] \in \mathbb{C}^{(N \times K)}$, $\boldsymbol{\mathcal{E}}_{\mathsf{RD}} = [\mathbf{e}_{\mathsf{RD},1}, \ldots, \mathbf{e}_{\mathsf{RD},K}] \in \mathbb{C}^{(N \times K)}$ is the estimation error matrix, which is independent of $\hat{\mathbf{G}}_{\mathsf{RD}}$, i.e., $\boldsymbol{\mathcal{E}}_{\mathsf{RD}} \sim \mathcal{CN}(0, \mathbf{E}_{\mathsf{RD}})$ with $\mathbf{E}_{\mathsf{RD}} = \text{diag}\left[\sigma_{e,1}^2, \ldots, \sigma_{e,K}^2\right]$, and $\hat{\mathbf{G}}_{\mathsf{RD}} \sim \mathcal{CN}(0, \mathbf{D}_{\mathsf{RD}} - \mathbf{E}_{\mathsf{RD}})$ with $\mathbf{D}_{\mathsf{RD}} - \mathbf{E}_{\mathsf{RD}} \triangleq \hat{\mathbf{D}}_{\mathsf{RD}} = \text{diag}\left[\hat{\sigma}_{\mathsf{RD},1}^2, \ldots, \hat{\sigma}_{\mathsf{RD},K}^2\right]$, whose element is $\hat{\sigma}_{\mathsf{RD},i}^2 \triangleq \sigma_{\mathsf{RD},i}^2 - \sigma_{e,i}^2$ for $i = 1, 2, \ldots, K$.

2.2.1. *MRC/MRT processing*

With low complexity, MRC/MRT scheme is widely applied in massive MIMO techniques.[4,33] Hence, the

MRC receiver and MRT beamforming matrices at the relay are respectively given by[5,6]

$$\mathbf{A}^T = \mathbf{A}_{\mathtt{MRC}}^T \triangleq \mathbf{G}_{\mathsf{BR}}^H, \tag{23}$$

and

$$\mathbf{B} = \mathbf{B}_{\mathtt{MRC}} \triangleq \rho_{\mathtt{MRC}} \hat{\mathbf{G}}_{\mathsf{RU}}^*. \tag{24}$$

Here, $\mathbf{A}_{\mathtt{MRC}}^T$ is chosen for facilitating signal processing in the first phase. In the second phase, $\mathbf{B}_{\mathtt{MRT}}$ is chosen under the practical CSI, i.e. $\hat{\mathbf{G}}_{\mathsf{RD}}$ based on the MRT criterion. Note that $\rho_{\mathtt{MRC}}$ is the power-normalization factor to meet the long-term total transmit power at the relay[6], namely,

$$\rho_{\mathtt{MRC}} \approx \sqrt{\frac{P_{\mathsf{R}}}{N\sum_{i=1}^{K}\hat{\sigma}_{\mathsf{RD},i}^2}}. \tag{25}$$

2.2.2. ZFR/ZFT *processing*

Similar to MRC/MRT scheme, when using ZFR/ZFT scheme for the receivers and precoders at R can be respectively given by[6]

$$\mathbf{A}^T = \mathbf{A}_{\mathtt{ZF}}^T \triangleq \left(\mathbf{G}_{\mathsf{BR}}^H \mathbf{G}_{\mathsf{BR}}\right)^{-1} \mathbf{G}_{\mathsf{BR}}^H, \tag{26}$$

and

$$\mathbf{B} = \mathbf{B}_{\mathtt{ZF}} \triangleq \rho_{\mathtt{ZF}} \hat{\mathbf{G}}_{\mathsf{RD}}^* \left(\hat{\mathbf{G}}_{\mathsf{RD}}^T \hat{\mathbf{G}}_{\mathsf{RD}}^*\right)^{-1} \tag{27}$$

where $\rho_{\mathtt{ZF}}$ is also the power normalization factor for ZFR/ZFT, in which we use the property of $\mathrm{Tr}(\mathbf{AB}) = \mathrm{Tr}(\mathbf{BA})$ and then applying[34] Lemma 2.9 to obtain

$$\rho_{\mathtt{ZF}} \approx \sqrt{\frac{(N-K)\,P_{\mathsf{R}}}{\sum_{i=1}^{K}\frac{1}{\hat{\sigma}_{\mathsf{RD},i}^2}}}. \tag{28}$$

3. ACHIEVABLE RATE ANALYSIS AND SECRECY PERFORMANCE

In this section, we will consider the achievable secrecy rate of the $\mathsf{BS} \to \mathsf{R} \to \mathsf{D}_k$ link based on the approach in the article,[35] where the received signal is analyzed as a known mean times the desired symbol plus an uncorrelated effective noise. This is widely utilized in analysis of MIMO technique since it can be obtained an explicit rate expression and no requirement of instantaneous CSI at destination. Therefore, we may analyze received signal streams at R and D as follows:

From (4), the k-th received signal stream at R is rewritten as

$$\mathbf{r}_k = \sqrt{P_{\mathsf{S}}}\mathbf{a}_k^T \mathbf{g}_{\mathsf{BR},k} x_k + \tilde{n}_{\mathsf{R}_k}, \tag{29}$$

where $\tilde{n}_{\mathsf{R}_k}$ is the effective noise at R, given by

$$\tilde{n}_{\mathsf{R}_k} \triangleq \sqrt{P_{\mathsf{S}}}\sum_{i\neq k}^{K}\mathbf{a}_k^T \mathbf{g}_{\mathsf{BR},i} x_i + \mathbf{a}_k^T n_{\mathsf{R}}. \tag{30}$$

From above analyses, the k-th received SINR at R for both cases of MRC/MRT and ZFR/ZFT is express as below

$$\gamma_{\mathsf{BR}_k}^{\mathtt{MRC/ZF}} \triangleq \frac{P_{\mathsf{S}}\left|\mathbb{E}\left\{\mathbf{a}_k^T \mathbf{g}_{\mathsf{BR},k}\right\}\right|^2}{P_{\mathsf{S}}\mathrm{Var}\left(\mathbf{a}_k^T \mathbf{g}_{\mathsf{BR},k}\right) + P_{\mathsf{S}}\mathsf{IS}_k + \mathsf{NR}_k}, \tag{31}$$

where IS_k and NR_k represent the interference between streams transmitted from $\mathsf{BS} \to \mathsf{R}$, and the noise at the relay, respectively. In particular, we have

$$\mathsf{IS}_k \triangleq \sum_{i\neq k}^{K}\mathbb{E}\left\{\left|\mathbf{a}_k^T \mathbf{g}_{\mathsf{BR},i}\right|^2\right\}, \tag{32}$$

$$\mathsf{NR}_k \triangleq \mathbb{E}\left\{\left|\mathbf{a}_k^T n_{\mathsf{R}}\right|^2\right\}. \tag{33}$$

Similar to signal analysis way as in the first phase, the corresponding received SINR at D_k in the second phase is derived from (6) as follows:

$$\gamma_{\mathsf{RD}_k}^{\mathtt{MRC/ZF}} \triangleq \frac{\left|\mathbb{E}\left\{\mathbf{g}_{\mathsf{RD},k}^T \mathbf{b}_k\right\}\right|^2}{\mathrm{Var}\left(\mathbf{g}_{\mathsf{RD},k}^T \mathbf{b}_k\right) + \sum_{i\neq k}^{K}\mathbb{E}\left\{\left|\mathbf{g}_{\mathsf{RD},k}^T \mathbf{b}_i\right|^2\right\} + 1}. \tag{34}$$

Next, the legitimate channel rate and the secrecy outage rate will be considered in detail by using the above technique.

3.1. MRC/MRT at R

When MRC receiver and MRT beamforming are performed, we have the following theorem.

Theorem 1. *For* MRC/MRT *processing, the achievable rate of the transmission link* $\mathsf{BS} \to \mathsf{R} \to \mathsf{D}_k$ *in the massive MIMO DF relaying system is tightly approximated as*

$$\mathscr{R}_{\mathsf{D}_k}^{\mathtt{MRC}} = \frac{1}{2}\log_2\left(1 + \min\left\{\frac{NP_{\mathsf{S}}\sigma_{\mathsf{BR}}^2}{KP_{\mathsf{S}}\sigma_{\mathsf{BR}}^2 + 1}, \frac{NP_{\mathsf{R}}\hat{\sigma}_{\mathsf{RD},k}^4}{\left[P_{\mathsf{R}}\left(\hat{\sigma}_{\mathsf{RD},k}^2 + \sigma_{e,k}^2\right) + 1\right]\sum_{i=1}^{K}\hat{\sigma}_{\mathsf{RD},i}^2}\right\}\right). \tag{35}$$

Proof. See Appendix A. □

For eavesdroppers, we assume that each eavesdropper has perfect CSI by the channel estimates. Therefore, the corresponding eavesdropper rate at E_k can be obtained as

$$\begin{aligned}\mathscr{R}_{\mathsf{E}_k}^{\mathtt{MRC}} &= \frac{1}{2}\log_2\left(1+\min\left(\gamma_{\mathsf{BR}_k}^{\mathtt{MRC}},\gamma_{\mathsf{RE}_k}^{\mathtt{MRC}}\right)\right),\\ &= \frac{1}{2}\log_2\left(1+\min\left(\frac{NP_{\mathsf{S}}\sigma_{\mathsf{BR}}^2}{KP_{\mathsf{S}}\sigma_{\mathsf{BR}}^2+1},\right.\right.\\ &\left.\left.\frac{\rho_{\mathtt{MRC}}^2\left|\mathbf{g}_{\mathsf{RE},k}^T\hat{\mathbf{g}}_{\mathsf{RD},k}^*\right|^2}{\rho_{\mathtt{MRC}}^2\sum_{i\neq k}^K\left|\mathbf{g}_{\mathsf{RE},k}^T\hat{\mathbf{g}}_{\mathsf{RD},i}^*\right|^2+1}\right)\right).\end{aligned} \tag{36}$$

Thus, the achievable secrecy rate at D_k can be given by

$$\mathscr{R}_{\mathsf{SE}_k}^{\mathtt{MRC}} = \frac{1}{2}\log_2\left(\frac{1+\min\left(\gamma_{\mathsf{BR}_k}^{\mathtt{MRC}},\gamma_{\mathsf{RD}_k}^{\mathtt{MRC}}\right)}{1+\min\left(\gamma_{\mathsf{BR}_k}^{\mathtt{MRC}},\gamma_{\mathsf{RE}_k}^{\mathtt{MRC}}\right)}\right). \tag{37}$$

Based on (37), the asymptotic form for the secrecy outage rate at D_k is derived in the following Theorem 2.

Theorem 2. *Subject to a predefined outage secrecy probability, ζ, the secrecy outage rate of D_k in* MRC/MRT *of massive MIMO DF relay network under $N > \max\left(K, \frac{(KP_{\mathsf{S}}\sigma_{\mathsf{BR}}^2+1)\hat{\sigma}_{\mathsf{RD},k}^2}{P_{\mathsf{S}}\sigma_{\mathsf{BR}}^2\sum_{i\neq k}^K\hat{\sigma}_{\mathsf{RD},i}^2}\right)$, is given by*

$$\mathscr{R}_{\mathtt{OSE}_k}^{\mathtt{MRC}} = \mathscr{R}_{\mathsf{D}_k}^{\mathtt{MRC}} - \mathscr{R}_{\mathtt{OE}_k}^{\mathtt{MRC}}(\zeta), \tag{38}$$

where $\mathscr{R}_{\mathtt{OE}_k}^{\mathtt{MRC}}(\zeta)$ is obtained as shown in (39) *at the top of the next page.*

Proof. See Appendix B. □

3.2. ZFR/ZFT at R

For ZFR/ZFT, we can also obtain the rate and secrecy
outage rate of D_k, which are similar to the consideration way in MRC/MRT. As a result, we have a closed-form expression for the achievable rate in the following Theorem 3.

Theorem 3. *For* ZFR/ZFT *processing, the achievable rate of the transmission link $\mathsf{BS}\rightarrow\mathsf{R}\rightarrow\mathsf{D}_k$ in the massive MIMO DF relaying system is given as in* (40) *shown at the top of the next page.* □

Next, the acquired rate at corresponding E_k for ZFR/ZFT is

$$\begin{aligned}y_{\mathsf{RE}_k} &= \rho_{\mathtt{ZF}}\mathbf{g}_{\mathsf{RE},k}^T\left[\hat{\mathbf{G}}_{\mathsf{RD}}^*\left(\hat{\mathbf{G}}_{\mathsf{RD}}^T\hat{\mathbf{G}}_{\mathsf{RD}}^*\right)^{-1}\right]_k x_k+\\ &\quad\rho_{\mathtt{ZF}}\sum_{i\neq k}^K\mathbf{g}_{\mathsf{RE},k}^T\left[\hat{\mathbf{G}}_{\mathsf{RD}}^*\left(\hat{\mathbf{G}}_{\mathsf{RD}}^T\hat{\mathbf{G}}_{\mathsf{RD}}^*\right)^{-1}\right]_i x_i+n_{\mathsf{E}_k},\\ &= \mathbf{g}_{\mathsf{RE},k}^T\left[\tilde{\mathbf{B}}_{\mathtt{ZF}}\right]_k x_k+\sum_{i\neq k/}^K\mathbf{g}_{\mathsf{RE},k}^T\left[\tilde{\mathbf{B}}_{\mathtt{ZF}}\right]_i x_i+n_{\mathsf{E}_k},\end{aligned} \tag{41}$$

where $\left[\tilde{\mathbf{B}}_{\mathtt{ZF}}\right]_k \triangleq \left[\hat{\mathbf{G}}_{\mathsf{RD}}^*\left(\hat{\mathbf{G}}_{\mathsf{RD}}^T\hat{\mathbf{G}}_{\mathsf{RD}}^*\right)^{-1}\right]_k$. Note that the received signal at E_k is presented to be similar to one at D_k in the proof of Theorem 3. Therefore, the acquired eavesdropper rate at E_k is given by

$$\begin{aligned}\mathscr{R}_{\mathsf{E}_k}^{\mathtt{ZF}} = \frac{1}{2}\log_2\left(1+\min\left\{(N-K)P_{\mathsf{S}}\sigma_{\mathsf{BR}}^2,\right.\right.\\ \left.\left.\frac{\rho_{\mathtt{ZF}}^2\left|\mathbf{g}_{\mathsf{RE},k}^T\left[\tilde{\mathbf{B}}_{\mathtt{ZF}}\right]_k\right|^2}{\rho_{\mathtt{ZF}}^2\left|\sum_{i\neq k}^K\mathbf{g}_{\mathsf{RE},k}^T\left[\tilde{\mathbf{B}}_{\mathtt{ZF}}\right]_i\right|^2+1}\right\}\right).\end{aligned} \tag{42}$$

The secrecy outage rate at D_k is derived in Theorem 4 by using the approach like MRC/MRT.

Theorem 4. *Subject to a predefined outage secrecy probability, ζ, the secrecy outage rate of D_k in* ZFR/ZFT *of the massive MIMO DF relay network under $N > \left(K+\frac{1}{P_{\mathsf{S}}\sigma_{\mathsf{BR}}^2\hat{\sigma}_{\mathsf{RD},k}^2\sum_{i\neq k}^K\frac{1}{\hat{\sigma}_{\mathsf{RD},i}^2}}\right)$, can be given by*

$$\mathscr{R}_{\mathtt{OSE}_k}^{\mathtt{ZF}} = \mathscr{R}_{\mathsf{D}_k}^{\mathtt{ZF}} - \mathscr{R}_{\mathtt{OE}_k}^{\mathtt{ZF}}(\zeta), \tag{43}$$

where $\mathscr{R}_{\mathtt{OE}_k}^{\mathtt{ZF}}(\zeta)$ is obtained as in (44) *shown at the top of the next page.*

Proof. See Appendix D. □

Remark 1. *It is found that the achievable rates in Theorem 1 and 3 are also valid for traditional MIMO systems. However, achieved their bounds in massive MIMO systems are tighter than that in traditional MIMO systems since the central theorem is performed to approximate the effective noise in both phases.*

$$\mathscr{R}_{\mathtt{OE}_k}^{\mathtt{MRC}}(\zeta) \triangleq \frac{1}{2}\log_2\left(\frac{N\sum_{i=1}^{K}\hat{\sigma}_{\mathsf{RD},i}^2 - \left(P_{\mathsf{R}}\sigma_{\mathsf{RE},k}^2\hat{\sigma}_{\mathsf{RD},k}^2 + P_{\mathsf{R}}\sigma_{\mathsf{RE},k}^2\sum_{i\neq k}^{K}\hat{\sigma}_{\mathsf{RD},i}^2\right)\log\zeta}{N\sum_{i=1}^{K}\hat{\sigma}_{\mathsf{RD},i}^2 - P_{\mathsf{R}}\sigma_{\mathsf{RE},k}^2\sum_{i\neq k}^{K}\hat{\sigma}_{\mathsf{RD},i}^2\log\zeta}\right). \tag{39}$$

$$\mathscr{R}_{\mathsf{D}_k}^{\mathtt{ZF}} = \frac{1}{2}\log_2\left(1+\min\left\{(N-K)P_{\mathsf{S}}\sigma_{\mathsf{BR}}^2, \frac{(N-K)P_{\mathsf{R}}\hat{\sigma}_{\mathsf{RD},k}^2}{P_{\mathsf{R}}\sum_{i=1}^{K}\sigma_{e,i}^2 + \hat{\sigma}_{\mathsf{RD},k}^2\sum_{i=1}^{K}\frac{1}{\hat{\sigma}_{\mathsf{RD},i}^2}}\right\}\right). \tag{40}$$

Remark 2. *Based on the effective multiuser interference suppressing capability of* ZFR/ZFT *technique in relaying systems, the achievable rate on the* $\mathsf{BS}\to\mathsf{R}\to\mathsf{D}_k$ *transmission link is better than that for* MRC/MRT.

Remark 3. *Satisfying constraint conditions in Theorem 2 and 4 is easy by more increasing a number of* N *antennas at* R. *It implies that the signal processing systems are proposed with low-complexity, and concurrently the secrecy outage rate can be improved due to the very large number of relay antennas.*

Therefore, the secrecy outage rate should be considered in the regime of very large N to enhance the spectral efficiency, namely to improve the secure downlink transmission in multi-antenna MIMO relaying systems in the presence of eavesdroppers. In addition, the joint utilization of massive MIMO and relay can fully exploit another benefit as cutting down transmit power at the BS and relay without compromising the system performance, which is shown by the following section.

4. ASYMPTOTIC ANALYSIS WITH MASSIVE ARRAYS

With the advantage of increasing a number of N antennas at R, this section will investigate in the asymptotic analysis scenarios to provide insights into the system characteristics. Specifically, when $N\to\infty$ with fixed total transmit power of E_{S} and E_{R}, i.e., $P_{\mathsf{S}}=\frac{E_{\mathsf{S}}}{N^{\alpha}}$, $P_{\mathsf{R}}=\frac{E_{\mathsf{R}}}{N^{\beta}}$ with $\alpha,\beta\in[0,1]$. $\mathscr{R}_{\mathtt{OSE}_k}^{\mathcal{A}}$ with $\mathcal{A}\in\{\mathtt{MRC},\mathtt{ZF}\}$ can be re-expressed, respectively, as

$$\mathscr{R}_{\mathtt{OSE}_k}^{\mathcal{A},\infty} = \mathscr{R}_{\mathsf{D}_k}^{\mathcal{A},\infty} - \mathscr{R}_{\mathtt{OE}_k}^{\mathcal{A},\infty}(\zeta), \tag{45}$$

where $\mathscr{R}_{\mathsf{D}_k}^{\mathcal{A},\infty}$ and $\mathscr{R}_{\mathtt{OE}_k}^{\mathcal{A},\infty}(\zeta)$ are given in (46) and (47) for MRC and (48) and (49) for ZF, respectively, with $e_{\mathtt{M}}=\sum_{i=1}^{K}\hat{\sigma}_{\mathsf{RD},i}^2$, $f_{\mathtt{M}}=-E_{\mathsf{R}}\sigma_{\mathsf{RE},k}^2\hat{\sigma}_{\mathsf{RD},k}^2\log\zeta$, $h_{\mathtt{M}}=-E_{\mathsf{R}}\sigma_{\mathsf{RE},k}^2\sum_{i\neq k}^{K}\hat{\sigma}_{\mathsf{RD},i}^2\log\zeta$, $e_{\mathtt{Z}}=\hat{\sigma}_{\mathsf{RD},k}^2\sum_{i=1}^{K}\frac{1}{\hat{\sigma}_{\mathsf{RD},i}^2}$, $f_{\mathtt{Z}}=-E_{\mathsf{R}}\sigma_{\mathsf{RE},k}^2\log\zeta$, and $e_{\mathtt{Z}}=-E_{\mathsf{R}}\sigma_{\mathsf{RE},k}^2\hat{\sigma}_{\mathsf{RD},k}^2\sum_{i\neq k}^{K}\frac{1}{\hat{\sigma}_{\mathsf{RD},i}^2}\log\zeta$.

$$\mathscr{R}_{\mathsf{D}_k}^{\mathtt{MRC}} = \frac{1}{2}\log_2\left(1+\min\left(\frac{NE_{\mathsf{S}}\sigma_{\mathsf{BR}}^2}{KE_{\mathsf{S}}\sigma_{\mathsf{BR}}^2+N^{\alpha}}, \frac{NE_{\mathsf{R}}\hat{\sigma}_{\mathsf{RD},k}^4}{\left[E_{\mathsf{R}}\left(\hat{\sigma}_{\mathsf{RD},k}^2+\sigma_{e,k}^2\right)+N^{\beta}\right]\sum_{i=1}^{K}\hat{\sigma}_{\mathsf{RD},i}^2}\right)\right), \tag{46}$$

$$\mathscr{R}_{\mathtt{OE}_k}^{\mathtt{MRC}}(\zeta) = \frac{1}{2}\log_2\left(\frac{N^{(1-\beta)}e_{\mathtt{M}}+f_{\mathtt{M}}+h_{\mathtt{M}}}{N^{(1-\beta)}e_{\mathtt{M}}+h_{\mathtt{M}}}\right), \tag{47}$$

and

$$\mathscr{R}_{\mathsf{D}_k}^{\mathtt{ZF}} = \frac{1}{2}\log_2\left(1+\min\left(\frac{(N-K)E_{\mathsf{S}}\sigma_{\mathsf{BR}}^2}{N^{\alpha}}, \frac{(N-K)E_{\mathsf{R}}\hat{\sigma}_{\mathsf{RD},k}^2}{E_{\mathsf{R}}\sum_{i=1}^{K}\sigma_{e,i}^2+N^{\beta}\hat{\sigma}_{\mathsf{RD},k}^2\sum_{i=1}^{K}\frac{1}{\hat{\sigma}_{\mathsf{RD},i}^2}}\right)\right), \tag{48}$$

$$\mathscr{R}_{\mathtt{OE}_k}^{\mathtt{ZF}}(\zeta) = \frac{1}{2}\log_2\left(\frac{N^{\beta}e_{\mathtt{Z}}+f_{\mathtt{Z}}+h_{\mathtt{Z}}}{N^{\beta}e_{\mathtt{Z}}+h_{\mathtt{Z}}}\right), \tag{49}$$

From (46) and (48), it shows that α and β should be chosen in the interval $[0,1]$ for non-vanishing $\mathscr{R}_{\mathsf{D}_k}^{\mathtt{MRC/ZF}}$ as $N\to\infty$. Because, if we choose α and/or $\beta>1$, $\mathscr{R}_{\mathsf{D}_k}^{\mathtt{MRC/ZF}}$ may be zero. Therefore, we now consider the asymptotic achievable rate and secrecy outage rate of the transmission link $\mathsf{BS}\to\mathsf{R}\to\mathsf{D}_k$ as $N\to\infty$ in some following special cases. More explicitly, selected factor pairs, (α,β), are at high bound of $[0,1]$, i.e., $\alpha=1$ and/or $\beta=1$, and in the interval $(0,1)$, i.e., $\alpha=1/2$ and/or $\beta=1/2$.

https://doi.org/10.52111/qnjs.2021.16307

$$\mathbf{R}_{\mathtt{OE}_k}^{\mathtt{ZF}}(\zeta) \triangleq \frac{1}{2}\log_2\left(\frac{\hat{\sigma}_{\mathtt{RD},k}^2\sum_{i=1}^{K}\frac{1}{\hat{\sigma}_{\mathtt{RD},i}^2} - \left(P_{\mathsf{R}}\sigma_{\mathtt{RE},k}^2 + P_{\mathsf{R}}\sigma_{\mathtt{RE},k}^2\hat{\sigma}_{\mathtt{RD},k}^2\sum_{i\neq k}^{K}\frac{1}{\hat{\sigma}_{\mathtt{RD},i}^2}\right)\log\zeta}{\hat{\sigma}_{\mathtt{RD},k}^2\sum_{i=1}^{K}\frac{1}{\hat{\sigma}_{\mathtt{RD},i}^2} - P_{\mathsf{R}}\sigma_{\mathtt{RE},k}^2\hat{\sigma}_{\mathtt{RD},k}^2\sum_{i\neq k}^{K}\frac{1}{\hat{\sigma}_{\mathtt{RD},i}^2}\log\zeta}\right). \quad (44)$$

Proposition 1. *When the number of N antennas at the relay approaches infinity, the secrecy outage rate of the transmission link $\mathsf{BS}\to\mathsf{R}\to\mathsf{D}_k$ for $\mathtt{MRC}/\mathtt{MRT}$ and $\mathtt{ZFT}/\mathtt{ZFR}$ in some cases can be asymptotically approximated, respectively, as follows:*

- *Case 1: α and β are chosen at bound to be equal to one in several cases as follows:*

- *Case 1.1:* $(\alpha,\beta)=(1,1)$ *i.e.,* $(P_{\mathsf{S}}=\frac{E_{\mathsf{S}}}{N}, P_{\mathsf{R}}=\frac{E_{\mathsf{R}}}{N})$

$$\mathscr{R}_{\mathtt{OSE}_k}^{\mathtt{MRC},\infty} = \frac{1}{2}\log_2\left(1+\min\left(E_{\mathsf{S}}\sigma_{\mathtt{BR}}^2, \frac{E_{\mathsf{R}}\hat{\sigma}_{\mathtt{RD},k}^4}{\sum_{i=1}^{K}\hat{\sigma}_{\mathtt{RD},i}^2}\right)\right) - \frac{1}{2}\log_2\left(\frac{e_{\mathtt{M}}+f_{\mathtt{M}}+h_{\mathtt{M}}}{e_{\mathtt{M}}+h_{\mathtt{M}}}\right), \quad (50)$$

$$\mathscr{R}_{\mathtt{OSE}_k}^{\mathtt{ZF},\infty} = \frac{1}{2}\log_2\left(1+\min\left(E_{\mathsf{S}}\sigma_{\mathtt{BR}}^2, \frac{E_{\mathsf{R}}}{\sum_{i=1}^{K}\frac{1}{\hat{\sigma}_{\mathtt{RD},i}^2}}\right)\right). \quad (51)$$

- *Case 1.2:* $(\alpha,\beta)=(0,1)$ *i.e.,* $(P_{\mathsf{S}}=E_{\mathsf{S}}, P_{\mathsf{R}}=\frac{E_{\mathsf{R}}}{N})$

$$\mathscr{R}_{\mathtt{OSE}_k}^{\mathtt{MRC},\infty} = \frac{1}{2}\log_2\left(1+\frac{E_{\mathsf{R}}\hat{\sigma}_{\mathtt{RD},k}^4}{\sum_{i=1}^{K}\hat{\sigma}_{\mathtt{RD},i}^2}\right) - \frac{1}{2}\log_2\left(\frac{e_{\mathtt{M}}+f_{\mathtt{M}}+h_{\mathtt{M}}}{e_{\mathtt{M}}+h_{\mathtt{M}}}\right), \quad (52)$$

$$\mathscr{R}_{\mathtt{OSE}_k}^{\mathtt{ZF},\infty} = \frac{1}{2}\log_2\left(1+\frac{E_{\mathsf{R}}}{\sum_{i=1}^{K}\frac{1}{\hat{\sigma}_{\mathtt{RD},i}^2}}\right). \quad (53)$$

- *Case 1.3:* $(\alpha,\beta)=(1,0)$ *i.e.,* $(P_{\mathsf{S}}=\frac{E_{\mathsf{S}}}{N}, P_{\mathsf{R}}=E_{\mathsf{R}})$

$$\mathscr{R}_{\mathtt{OSE}_k}^{\mathtt{MRC},\infty} = \frac{1}{2}\log_2\left(1+E_{\mathsf{S}}\sigma_{\mathtt{BR}}^2\right), \quad (54)$$

$$\mathscr{R}_{\mathtt{OSE}_k}^{\mathtt{ZF},\infty} = \frac{1}{2}\log_2\left(1+E_{\mathsf{S}}\sigma_{\mathtt{BR}}^2\right) - \frac{1}{2}\log_2\left(\frac{e_{\mathtt{Z}}+f_{\mathtt{Z}}+h_{\mathtt{Z}}}{e_{\mathtt{Z}}+h_{\mathtt{Z}}}\right). \quad (55)$$

- *Case 2: α and β are chosen in the interval $(0,1)$. We choose $\alpha=1/2$ and/or $\beta=1/2$ in several cases as follows:*

- *Case 2.1:* $(\alpha,\beta)=(1/2,1/2)$ *i.e.,* $(P_{\mathsf{S}}=\frac{E_{\mathsf{S}}}{\sqrt{N}}, P_{\mathsf{R}}=\frac{E_{\mathsf{R}}}{\sqrt{N}})$

$$\mathscr{R}_{\mathtt{OSE}_k}^{\mathtt{MRC},\infty} = \frac{1}{2}\log_2\left(1+\min\left(\sqrt{N}E_{\mathsf{S}}\sigma_{\mathtt{BR}}^2, \frac{\sqrt{N}E_{\mathsf{R}}\hat{\sigma}_{\mathtt{RD},k}^4}{\sum_{i=1}^{K}\hat{\sigma}_{\mathtt{RD},i}^2}\right)\right), \quad (56)$$

$$\mathscr{R}_{\mathtt{OSE}_k}^{\mathtt{ZF},\infty} = \frac{1}{2}\log_2\left(1+\min\left(\sqrt{N}E_{\mathsf{S}}\sigma_{\mathtt{BR}}^2, \frac{\sqrt{N}E_{\mathsf{R}}}{\sum_{i=1}^{K}\frac{1}{\hat{\sigma}_{\mathtt{RD},i}^2}}\right)\right). \quad (57)$$

- *Case 2.2:* $(\alpha,\beta)=(0,1/2)$ *i.e.,* $(P_{\mathsf{S}}=E_{\mathsf{S}}, P_{\mathsf{R}}=\frac{E_{\mathsf{R}}}{\sqrt{N}})$

$$\mathscr{R}_{\mathtt{OSE}_k}^{\mathtt{MRC},\infty} = \frac{1}{2}\log_2\left(1+\frac{\sqrt{N}E_{\mathsf{R}}\hat{\sigma}_{\mathtt{RD},k}^4}{\sum_{i=1}^{K}\hat{\sigma}_{\mathtt{RD},i}^2}\right), \quad (58)$$

$$\mathscr{R}_{\mathtt{OSE}_k}^{\mathtt{ZF},\infty} = \frac{1}{2}\log_2\left(1+\frac{\sqrt{N}E_{\mathsf{R}}}{\sum_{i=1}^{K}\frac{1}{\hat{\sigma}_{\mathtt{RD},i}^2}}\right). \quad (59)$$

- *Case 2.3:* $(\alpha,\beta)=(1,0)$ *i.e.,* $(P_{\mathsf{S}}=\frac{E_{\mathsf{S}}}{\sqrt{N}}, P_{\mathsf{R}}=E_{\mathsf{R}})$

$$\mathscr{R}_{\mathtt{OSE}_k}^{\mathtt{MRC},\infty} = \frac{1}{2}\log_2\left(1+\sqrt{N}E_{\mathsf{S}}\sigma_{\mathtt{BR}}^2\right), \quad (60)$$

$$\mathscr{R}_{\mathtt{OSE}_k}^{\mathtt{ZF},\infty} = \frac{1}{2}\log_2\left(1+\sqrt{N}E_{\mathsf{S}}\sigma_{\mathtt{BR}}^2\right) - \frac{1}{2}\log_2\left(\frac{e_{\mathtt{Z}}+f_{\mathtt{Z}}+h_{\mathtt{Z}}}{e_{\mathtt{Z}}+h_{\mathtt{Z}}}\right). \quad (61)$$

$$\mathscr{R}_{\mathrm{D}_k}^{\mathrm{ZF}} = \frac{1}{2}\log_2\left(1+\min\left(\frac{(N-K)E_{\mathsf{S}}\sigma_{\mathsf{BR}}^2}{N}, \frac{(N-K)E_{\mathsf{R}}\hat{\sigma}_{\mathsf{RD},k}^2}{E_{\mathsf{R}}\sum_{i=1}^{K}\sigma_{e,i}^2 + N\hat{\sigma}_{\mathsf{RD},k}^2\sum_{i=1}^{K}\frac{1}{\hat{\sigma}_{\mathsf{RD},i}^2}}\right)\right), \tag{62}$$

$$\mathscr{R}_{\mathrm{OE}_k}^{\mathrm{ZF}}(\zeta) = \frac{1}{2}\log_2\left(\frac{N\hat{\sigma}_{\mathsf{RD},k}^2\sum_{i=1}^{K}\frac{1}{\hat{\sigma}_{\mathsf{RD},i}^2} - \left(\sigma_{\mathsf{RE},k}^2 + \sigma_{\mathsf{RE},k}^2\hat{\sigma}_{\mathsf{RD},k}^2\sum_{i\neq k}^{K}\frac{1}{\hat{\sigma}_{\mathsf{RD},i}^2}\right)E_{\mathsf{R}}\log\zeta}{N\hat{\sigma}_{\mathsf{RD},k}^2\sum_{i=1}^{K}\frac{1}{\hat{\sigma}_{\mathsf{RD},i}^2} - E_{\mathsf{R}}\sigma_{\mathsf{RE},k}^2\hat{\sigma}_{\mathsf{RD},k}^2\sum_{i\neq k}^{K}\frac{1}{\hat{\sigma}_{\mathsf{RD},i}^2}\log\zeta}\right). \tag{63}$$

Proof. We first consider Case 1.1 by rewriting (48) and (49) with $P_{\mathsf{S}} = E_{\mathsf{S}}/N, P_{\mathsf{R}} = E_{\mathsf{S}}/N$, as in (62) and (63) shown at the top of the next page. The desired result as in (50) and (51) can be readily obtained by the property of $\log_2(1) = 0$ as $N \to \infty$. Other cases are omitted due to having the similar proof way. □

Remark 4. *Proposition 1 shows that, in the regime of very large relay antennas associating with either* MRC/MRT *or* ZFR/ZFT *technique at the relay, the transmit powers at both the* BS *and* R *in Case 1 and Case 2 will be scaled by factor* $1/N$ *and* $1/\sqrt{N}$*, respectively. As a result, the deterministic asymptotic expression of* $\mathscr{R}_{\mathrm{OSE}_k}^{\mathrm{MRC/ZF}}$ *is derived as* $N \to \infty$ *in all cases. In addition, the acquired rate of the* k*-th eavesdropper in almost cases is average out due to the law of large numbers, i.e.,* $\mathscr{R}_{\mathrm{OE}_k}^{\mathrm{MRC/ZF}} \to 0$*, except some cases as Case 1.1 and 1.2 for* MRC/MRT*, Case 1.3 and 2.3 for* ZFR/ZFT *go to a constant value as* $N \to \infty$*. Thus, to obtain the effectiveness against eavesdropper, Case 2 should be adopted into the massive MIMO DF relaying system.*

5. NUMERICAL RESULTS

In this section, we will assess the secure performance under different consideration by employing Monte-Carlo simulations. Most of the simulation cases, we set $\zeta = 0, 1$, $\sigma_{e,i}^2 = 0.1$, $K = 10$, and $P_{\mathsf{S}} = P_{\mathsf{R}} = 10$ dB, where the signal-to-noise ratio (SNR) is defined by either $\mathrm{SNR}_{\mathsf{S}} = 10\log_{10} P_{\mathsf{S}}$ or $\mathrm{SNR}_{\mathsf{R}} = 10\log_{10} P_{\mathsf{R}}$ to represent different transmit SNRs in dB at either BS or R, respectively. Moreover, we will take the path-loss effect of $\sigma_{\mathsf{RE},k}$ when its value is adjusted, and of σ_{BR} is normalized, i.e., $\sigma_{\mathsf{BR}} = 1$.

Figures 2 and 3 illustrate secure performance of both MRC/MRT and ZFR/ZFT processing techniques at the

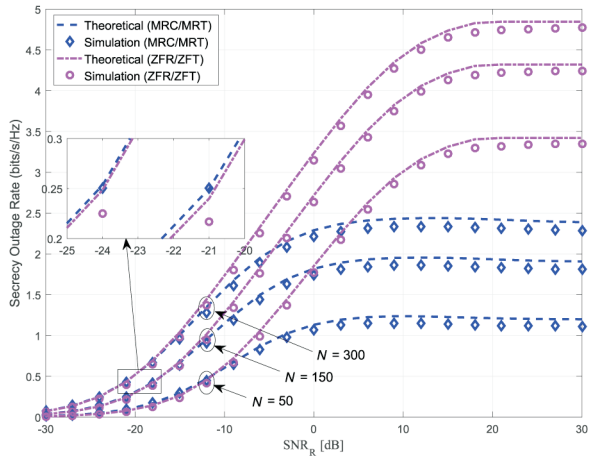

Figure 2. Secrecy outage rate versus P_{R} with $\sigma_{RE,k} = 1$ and $P_{\mathsf{S}} = 10$ dB.

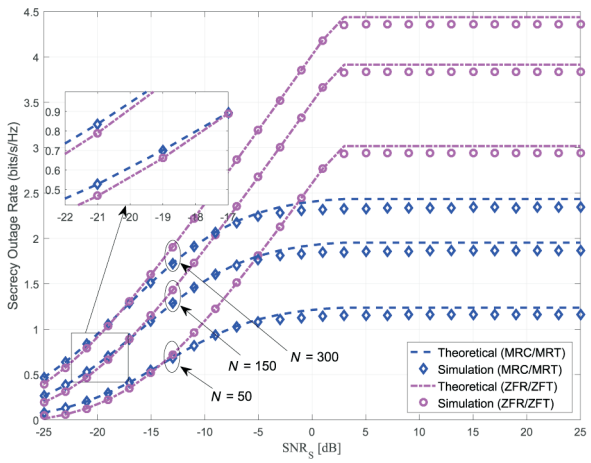

Figure 3. Secrecy outage rate versus P_{S} with $\sigma_{RE,k} = 1$ and $P_{\mathsf{R}} = 10$ dB.

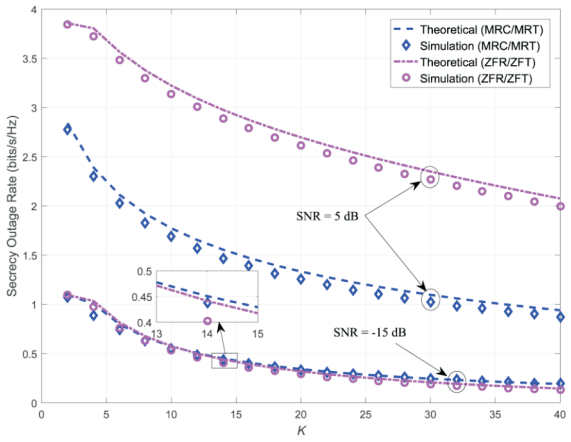

Figure 4. Secrecy outage rate versus number of destinations with $\sigma_{\mathsf{E},k} = 1, \text{SNR} = P_{\mathsf{S}} = P_{\mathsf{R}}$ and $N = 120$.

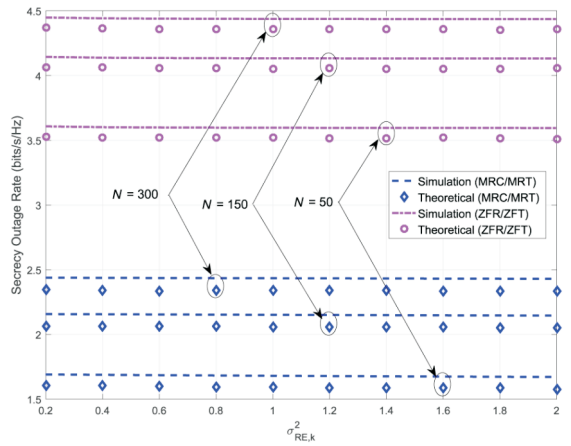

Figure 5. Effect of N on secrecy outage rate with $P_{\mathsf{S}} = P_{\mathsf{R}} = 10$ dB and $\zeta = 0.1$

relay, for the same target secure outage probability ζ by varying different transmit SNR_{R} with fixed P_{S} corresponding Figure 2 and different transmit SNR_{S} with fixed P_{R} corresponding Figure 3. In Figures 2 and 3, the secrecy outage rate will be improved by increasing either P_{R} or P_{S} increases at low SNR regime but it rapidly approaches to a saturated level, which is determined by network settings. However, when the secrecy outage rate is considered in three cases of N, i.e., $N = 50, N = 150$ and $N = 300$, it can see that increasing a number of N relay antennas can enhance the system outage rate for all range of SNRs and processing technique used at the relay. As a result, there are the following two distinguished regions. The secrecy outage rate for MRC/MRT outferforms that for ZFR/ZFT at low SNR regime. Whereas, the achieved secrecy outage rate for ZFR/ZFT within high SNR regime is better. It is due to the fact that, at high regime, the effect of multiuser interference for the MRC/MRT scheme is larger than that for ZFR/ZFT, while the system for ZFR/ZFT is able to null multiuser interference signals,[6] i.e., multiuser interference is not completely canceled out in MRC/MRT but nulled by projecting each stream onto the orthogonal complement in ZFR/ZFT scheme.

In Figure 4, the secrecy outage rate is investigated under two typical network settings, i.e., Case 1: $\text{SNR} = P_{\mathsf{S}} = P_{\mathsf{R}} = -15$ dB and Case 2: $\text{SNR} = P_{\mathsf{S}} = P_{\mathsf{R}} = 5$ dB, when we adjust a number of destinations, K. It can see that MRC/MRT outperforms ZFR/ZFT in Case 1 but not the same in Case 2, which is consistent with the numerical results in Figure 2 and 3. Because the multiuser interference of the transmission link $\mathsf{BS} \to \mathsf{R} \to \mathsf{D}_k$ within low SNR is very small, due to being inversely proportional to the number of antennas. However, within high regimes of SNR, the multiuser interference is large enough, resulting in secrecy outage rate for MRC/MRT is inferior.

In Figure 5, the transmit power at the source and the relay are fixed by 10 dB, i.e., $P_{\mathsf{S}} = P_{\mathsf{R}} = 10$ dB and $\zeta = 0.1$. The effect of eavesdropper links is investigated by comparing the secrecy outage rate with different values of $\sigma_{\mathsf{RE},k}$. It can be seen in Figure 5 that, for a given outage probability bound ζ, ZFR/ZFT can derive better secrecy outage rate than MRC/MRT, which confirms the advantage of the ZFR/ZFT scheme over the MRC/MRT within moderate to high SNR region. Moreover, the secrecy outage rate is considered in three cases of N, i.e., $N = 100$, $N = 200$, and $N = 300$, with the same effect of $\sigma_{\mathsf{RE},k}$. Results shows that increasing the number of antennas's N at R provides us an effective method to improve the achieved secrecy outage rate. On the other hand, the MRC/MRT and ZFR/ZFT are not so sensitive to short-distance eavesdropper, which shows us that the capability of both linear processing techniques against passive eavesdropper at short-distance is fairly good.

In the two figures of Figures 6 and 7, we illustrate the system secure performance when N approaches infinity in some power-scaling laws of Case 1, and 2, as addressed in Proposition 1. As expected, all asymptotic secrecy outage rates are in good agreements with the upper bound in Case 1 and the enhancement of rate of OSE_K $\left(\mathscr{R}_{\text{OSE}_k}^{\text{MRC/ZF}}\right)$ in Case 2 at high regime

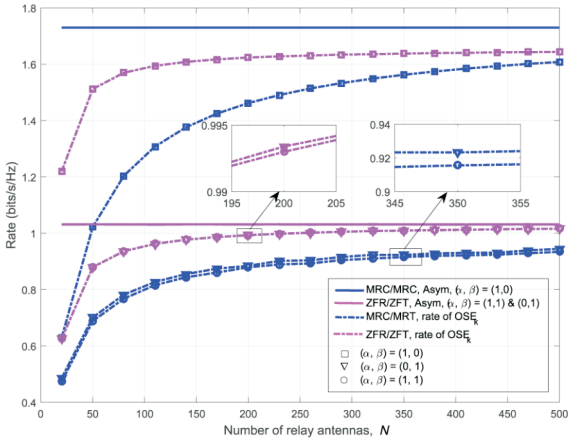

Figure 6. Secrecy rate comparison of MRC/MRT and ZFR/ZFT relaying schemes versus N in Case 1 of power scaling law with $E = E_{\mathsf{S}} = E_{\mathsf{R}} = 10$ dB and $\zeta = 0.1$.

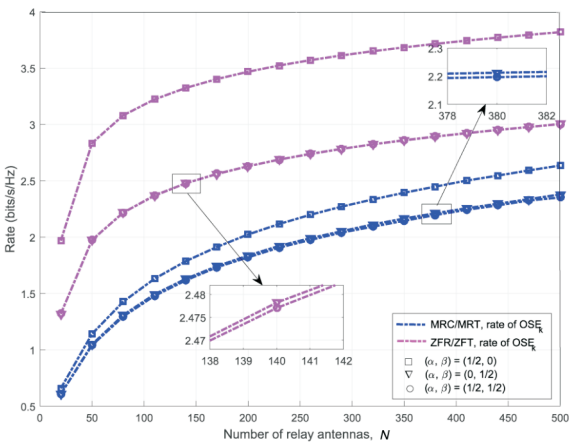

Figure 7. Secrecy outage rate comparison of MRC/MRT and ZFR/ZFT relaying schemes versus N in Case 2 of power scaling law with $E = E_{\mathsf{S}} = E_{\mathsf{R}} = 10$ dB and $\zeta = 0.1$.

of N. The advantage of ZFR/ZFT over MRC/MRT is also verified. For example, ZFR/ZFT can provide secrecy outage rate of 1.4 bits/s/Hz with $N = 40$ while $N = 150$ is required for MRC/MRT in Figure 6. Moreover, it can be seen in Figures 6 and 7 that, using both linear processing methods in Cases 1.3 and 2.3, i.e., $(\alpha, \beta) = (1, 0)$ and $(\alpha, \beta) = (1/2, 0)$ respectively, there is the best $\mathscr{R}_{\mathtt{OSE}_k}^{\mathtt{MRC/ZF}}$ compared to other cases of Case 1, i.e., $\left[(\alpha, \beta) = (1, 1); (\alpha, \beta) = (1, 0)\right]$ and

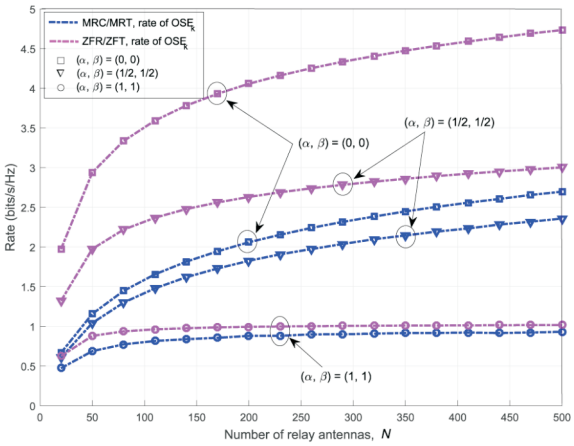

Figure 8. Secrecy outage rate of MRC/MRT and ZFR/ZFT relaying schemes versus N in Theorem 2, Theorem 4, Case 1.1 and Case 2.1 of power scaling law with $E = E_{\mathsf{S}} = E_{\mathsf{R}} = 10$ dB and $\zeta = 0.1$.

that of Case 2, i.e., $\left[(\alpha, \beta) = (1/2, 1/2); (\alpha, \beta) = (1/2, 0)\right]$ respectively, which proves that allocating transmit power at R also has significantly effect on the secrecy outage rate. Meanwhile, there is a gap of $\mathscr{R}_{\mathtt{OSE}_k}^{\mathtt{MRC/ZF}}$ between Case 1.1 and Case 1.2 or Case 2.1 and Case 2.2 being very small in Figure 6 or 7, respectively.

Furthermore, we can see that, the effective improvement of $\mathscr{R}_{\mathtt{OSE}_k}^{\mathtt{MRC/ZF}}$ according to Theorems 2 and 4, i.e., $(\alpha, \beta) = (0, 0)$, is the best when comparing to Cases 1.1 and 2.1 i.e., $(\alpha, \beta) = (1/2, 1/2)$ and $(\alpha, \beta) = (1, 1)$ respectively, as illustrated in Figure 8. However, reductive capability of transmit power at BS and R in case of $(\alpha, \beta) = (0, 0)$ hasn't ability. In Case 1.1 with $(\alpha, \beta) = (1, 1)$, the transmit power cutdown at BS and R is the best by inversely proportional to the number of antennas, $1/N$, but $\mathscr{R}_{\mathtt{OSE}_k}^{\mathtt{MRC/ZF}}$ in this case is small since it rapidly approaches to a saturated level in spite of increasing $N \to \infty$. Fortunately, Case 2.1 with $(\alpha, \beta) = (1/2, 1/2)$ shows that the transmit power at BS and R can be scaled by factor $1/\sqrt{N}$ and concurrently improving the effective $\mathscr{R}_{\mathtt{OSE}_k}^{\mathtt{MRC/ZF}}$ as more increasing N in Figure 8. From above analyses, it allows us chose effective relaying schemes based on given secure requirement of system performance.

https://doi.org/10.52111/qnjs.2021.16307

6. CONCLUSION

In this paper, we have introduced a secure multiuser transmission downlink based on massive MIMO DF relaying strategy, in which both MRC/MRT and ZFR/ZFT techniques are adopted into physical layer security. As a result, the exact and asymptotic expressions for user rate and outage secrecy rate for a predetermined secure outage probability of eavesdropper links with CSI imperfection are derived. We then have focused on the analysis and comparison of secrecy outage rate expressions in terms of SNRs, different number of users, number of antennas and eavesdropper distance. It is shown that, ZFR/ZFT processing technique at relay provides a better choice than the MRC/MRT based one in terms of the achieved secrecy performance. It is noteworthy that, information leakage prevention in all cases is quite good regardless of passive eavesdroppers located a short-distance from the relay. Since we can observe that passive eavesdroppers have less effect on secrecy rate when multiple-antenna MIMO relaying techniques are adopted. Specifically, the acquired rate of an eavesdropper diminishes to zero when asymptotic analysis is considered in various scenarios. In particular, the MIMO DF relaying system based on the large antenna array gain can balance between the achievable secrecy outage rate and effective decreased transmit power at the relay and BS. These results provide some useful insights to assist the design of massive MIMO relaying schemes for secure information transmission.

7. APPENDIX

A. Proof of Theorem 1

In this appendix, Theorem 1 is proved to achieve the rate of the transmission link $\mathsf{BS} \to \mathsf{R} \to \mathsf{D}_k$. Based on MRC/MRT, the expression (16) is rewritten as

$$\mathscr{R}_{\mathsf{D}_k}^{\mathtt{MRC}} = \frac{1}{2}\log_2\left(1+\min\left(\gamma_{\mathsf{RB}_k}^{\mathtt{MRC}}, \gamma_{\mathsf{RD}_k}^{\mathtt{MRC}}\right)\right), \quad (64)$$

From (64), we first need to calculate $\gamma_{\mathsf{RB}_k}^{\mathtt{MRC}}$, including four terms, i.e., $\mathbb{E}\left\{\mathbf{a}_k^T\mathbf{g}_{\mathsf{BR},k}\right\}$, $\mathrm{Var}\left(\mathbf{a}_k^T\mathbf{g}_{\mathsf{BR},k}\right)$, IS_k, and NR_k, as follows:
We derive $\mathbb{E}\left\{\mathbf{a}_k^T\mathbf{g}_{\mathsf{BR},k}\right\}$ by using MRC with $\mathbf{A}^T = \mathbf{G}_{\mathsf{BR}}^H$ as

$$\mathbb{E}\left\{\mathbf{a}_k^T\mathbf{g}_{\mathsf{BR},k}\right\} = \mathbb{E}\left\{\left\|\mathbf{g}_{\mathsf{BR},k}\right\|^2\right\} \approx N\sigma_{\mathsf{BR}}^2. \quad (65)$$

We are now to achieve $\mathrm{Var}\left(\mathbf{a}_k^T\mathbf{g}_{\mathsf{BR},k}\right)$, which is rewritten after using (65) as

$$\begin{aligned}\mathrm{Var}\left(\mathbf{a}_k^T\mathbf{g}_{\mathsf{BR},k}\right) &= \mathbb{E}\left\{\left|\mathbf{a}_k^T\mathbf{g}_{\mathsf{BR},k}\right|^2\right\} - N^2\sigma_{\mathsf{BR}}^4,\\ &= \mathbb{E}\left\{\left\|\mathbf{g}_{\mathsf{BR},k}\right\|^4\right\} - N^2\sigma_{\mathsf{BR}}^4. \quad (66)\end{aligned}$$

By applying [34, Lemma 2.9], we have

$$\begin{aligned}\mathrm{Var}\left(\mathbf{a}_k^T\mathbf{g}_{\mathsf{BR},k}\right) &= N(N+1)\sigma_{\mathsf{BR}}^4 - N^2\sigma_{\mathsf{BR}}^4,\\ &= N\sigma_{\mathsf{BR}}^4. \quad (67)\end{aligned}$$

We derive the third term, i.e., IS_k, by re-expressing it as follows:

$$\begin{aligned}\mathbb{E}\left\{\left|\mathbf{a}_k^T\mathbf{g}_{\mathsf{BR},i}\right|^2\right\} &= \sum_{i\neq k}^{K}\mathbb{E}\left\{\left|\mathbf{g}_{\mathsf{BR},k}^H\mathbf{g}_{\mathsf{BR},i}\right|^2\right\},\\ &= N(K-1)\sigma_{\mathsf{BR}}^4. \quad (68)\end{aligned}$$

In a similar way, we obtain NR_k as

$$\begin{aligned}\mathsf{NR}_k &= \mathbb{E}\left\{\left|\mathbf{g}_{\mathsf{BR},k}^T\mathbf{n}_{\mathsf{R}}\right|^2\right\},\\ &= N\sigma_{\mathsf{BR}}^2. \quad (69)\end{aligned}$$

Substituting (65), (67), (68), and (69) into (29), we obtain the result of $\gamma_{\mathsf{BR}_k}^{\mathtt{MRC}}$ as

$$\gamma_{\mathsf{BR}_k}^{\mathtt{MRC}} = \frac{NP_{\mathsf{S}}\sigma_{\mathsf{BR}}^2}{KP_{\mathsf{S}}\sigma_{\mathsf{BR}}^2+1}. \quad (70)$$

Next, we derive a approximated expression SINR of the transmission link $\mathsf{R} \to \mathsf{D}_k$, by following the same calculative way in the first phase above. As a result, we have

$$\gamma_{\mathsf{RD}_k}^{\mathtt{MRC}} = \frac{NP_{\mathsf{R}}\hat{\sigma}_{\mathsf{RD},k}^4}{\left[P_{\mathsf{R}}\left(\hat{\sigma}_{\mathsf{RD},k}^2+\sigma_{e,k}^2\right)+1\right]\sum_{i=1}^{K}\hat{\sigma}_{\mathsf{RD},i}^2}. \quad (71)$$

From (70) and (71), we finally obtain (35) in Theorem 1.

B. Proof of Theorem 2

We will prove Theorem 2 from starting (19), hence, the inverse CDF of γ_{E_k} is needed. We first need to calculate the SINR expression of $\gamma_{\mathsf{RE}_k}^{\mathtt{MRC}}$ (36) in terms of $\left|\mathbf{g}_{\mathsf{RE},k}^T\hat{\mathbf{g}}_{\mathsf{RD},k}^*\right|^2$ and $\sum_{i\neq k}^{K}\left|\mathbf{g}_{\mathsf{RE},k}^T\hat{\mathbf{g}}_{\mathsf{RD},i}^*\right|^2$ with MRT beamforming, $\mathbf{B} = \mathbf{B}_{\mathtt{MRC}} \triangleq \rho_{\mathtt{MRC}}\hat{\mathbf{G}}_{\mathsf{RD}}^*$.

For $\left|\mathbf{g}_{\mathsf{RE},k}^T\hat{\mathbf{g}}_{\mathsf{RD},k}^*\right|^2$, we have

$$\begin{aligned}\left|\mathbf{g}_{\mathsf{RE},k}^T\mathbf{b}_k\right|^2 &= \left|\mathbf{g}_{\mathsf{RE},k}^T\hat{\mathbf{g}}_{\mathsf{RD},k}^*\right|^2,\\ &= \left\|\mathbf{g}_{\mathsf{RE},k}\right\|^2\rho_{\mathtt{MRC}}^2\hat{\sigma}_{\mathsf{RE},k}^2. \end{aligned} \quad (72)$$

Similarly, we also have

$$\begin{aligned}\sum_{i\neq k}^{K}\left|\mathbf{g}_{\mathsf{RE},k}^T\mathbf{b}_i\right|^2 &= \sum_{i\neq k}^{K}\left|\mathbf{g}_{\mathsf{RE},k}^T\hat{\mathbf{g}}_{\mathsf{RD},i}^*\right|^2,\\ &= \left\|\mathbf{g}_{\mathsf{RE},k}\right\|^2\rho_{\mathtt{MRC}}^2\sum_{i\neq k}^{K}\hat{\sigma}_{\mathsf{RD},i}^2. \end{aligned} \quad (73)$$

Substituting (72) and (73) and into (36), the achievable rate of the eavesdropper channel $\mathsf{BS}\rightarrow\mathsf{R}\rightarrow\mathsf{E}_k$ is

$$\mathscr{R}_{\mathsf{E}_k}^{\mathtt{MRC}} = \log_2\left(1+\min\left(\frac{NP_{\mathsf{S}}\sigma_{\mathsf{BR}}^2}{KP_{\mathsf{S}}\sigma_{\mathsf{BR}}^2+1}, \frac{\left\|\mathbf{h}_{\mathsf{RE},k}\right\|^2 b}{\left\|\mathbf{h}_{\mathsf{RE},k}\right\|^2 c+Nd}\right)\right), \quad (74)$$

where $\mathbf{g}_{\mathsf{RE},k} = \sqrt{\eta_{\mathsf{RE},k}}\mathbf{h}_{\mathsf{RE},k}$ with $\eta_{\mathsf{RE},k}$ being distance-dependent path-loss attenuation with the value of one denoted by $\sigma_{\mathsf{RE},k}^2$, $b = P_{\mathsf{R}}\sigma_{\mathsf{RE},k}^2\hat{\sigma}_{\mathsf{RD},k}^2$, $c = P_{\mathsf{R}}\sigma_{\mathsf{RE},k}^2\sum_{i\neq k}^{K}\hat{\sigma}_{\mathsf{RD},i}^2$, and $d = \sum_{i=1}^{K}\hat{\sigma}_{\mathsf{RD},i}^2$.
From (74), we can rewrite the expression (19) as in (75) shown at the top of the next page. Next, it notes that we can simplify the expression (75) based on the characteristic of network setting by using advantage of large antenna arrays at R. Specifically, making $\gamma_{\mathsf{BR},k}^{\mathtt{MRC}}$ is always greater than $\gamma_{\mathsf{RE},k}^{\mathtt{MRC}}$ if $C1: N > \frac{\left(KP_{\mathsf{S}}\sigma_{\mathsf{BR}}^2+1\right)\hat{\sigma}_{\mathsf{RD},k}^2}{P_{\mathsf{S}}\sigma_{\mathsf{BR}}^2\sum_{i\neq k}^{K}\hat{\sigma}_{\mathsf{RD},i}^2}$. Consequently, we have

$$\zeta = \Pr\left(\frac{\left\|\mathbf{h}_{\mathsf{RE},k}\right\|^2 b}{\left\|\mathbf{h}_{\mathsf{RE},k}\right\|^2 c+Nd} > 2^{2\left(\mathscr{R}_{\mathsf{D}_k}^{\mathtt{MRC}}-\mathscr{R}_{\mathtt{OSE}_k}^{\mathtt{MRC}}\right)}-1\right). \quad (76)$$

Having (76) at hands allows us to derive the the CDF of $\gamma_{\mathsf{E}_k}^{\mathtt{MRC}}$. Mathematically, we can write

$$F_{\gamma_{\mathsf{E}_k}}(\gamma) = \Pr\left(\frac{\left\|\mathbf{h}_{\mathsf{RE},k}\right\|^2 b}{\left\|\mathbf{h}_{\mathsf{RE},k}\right\|^2 c+Nd} < \gamma\right) \quad (77)$$

Over Rayleigh fading channels, $\left\|\mathbf{h}_{\mathsf{RE},k}\right\|^2$ is χ^2 distributed with 2 degrees of freedom, it is straightforward to arrive at

$$\begin{aligned}F_{\gamma_{\mathsf{E}_k}}(\gamma) &= \Pr\left(\left\|\mathbf{h}_{\mathsf{E},k}\right\|^2 < \frac{Nd\gamma}{b-c\gamma}\right),\\ &= 1-\exp\left(-\frac{Nd\gamma}{b-c\gamma}\right). \end{aligned} \quad (78)$$

resulting in $F_{\gamma_{\mathsf{E}_k}}^{-1}(\gamma)$ as

$$F_{\gamma_{\mathsf{E}_k}}^{-1}(\gamma) = \frac{Nd-(b+c)\log(1-\gamma)}{Nd-c\log(1-\gamma)}. \quad (79)$$

Combining (21) and (79), Theorem 2 is derive.

C. Proof of Theorem 3

Proof of Theorem 3 is starting from (16), in which the definition of the achievable rate of the transmission link $\mathsf{BR}\rightarrow\mathsf{R}\rightarrow\mathsf{D}_k$ is derived by using ZFR/ZFT. Hence, we need to calculate both $\gamma_{\mathsf{BR}_k}^{\mathtt{ZF}}$ and $\gamma_{\mathsf{RD}_k}^{\mathtt{ZF}}$ in two phases as follows:
Firstly, the k-th signal stream processed at R can be rewritten by recalling $\mathbf{A}_{\mathtt{ZF}}$ in (26) as in (80) shown at the top of the next page. where $\left[\tilde{\mathbf{A}}_{\mathtt{ZF}}\right]_k \triangleq \left[\left(\mathbf{G}_{\mathsf{BR}}^H\mathbf{G}_{\mathsf{BR}}\right)^{-1}\mathbf{G}_{\mathsf{BR}}^H\right]_k$.

The SINR at r_k due to no multiple signal stream interference, i.e., $\mathtt{IS}_k = 0$, can be rewritten as

$$\gamma_{\mathsf{D}_k}^{\mathtt{ZF}} \triangleq \frac{P_{\mathsf{S}}\left|\mathbb{E}\left\{\left[\tilde{\mathbf{A}}_{\mathtt{ZF}}\right]_k\mathbf{g}_{\mathsf{BR},k}\right\}\right|^2}{P_{\mathsf{S}}\mathrm{Var}\left(\left[\tilde{\mathbf{A}}_{\mathtt{ZF}}\right]_k\mathbf{g}_{\mathsf{BR},k}\right)+\mathtt{NR}_k}, \quad (81)$$

With property of ZF , we have $\mathbf{A}_{ZF}^T\mathbf{G}_{\mathsf{BR}} = \mathbf{I}_K$[5] resulting in $\left[\tilde{\mathbf{A}}_{\mathtt{ZF}}\right]_k\mathbf{g}_{\mathsf{BR},i} = \delta_{ki}$, where $\delta_{1,ki} = 1$ when $k = i$ and 0 otherwise. Therefore, we have

$$\mathbb{E}\left\{\left[\tilde{\mathbf{A}}_{\mathtt{ZF}}\right]_k\mathbf{g}_{\mathsf{BR},k}\right\} = 1. \quad (82)$$

From (82), the variance of $\left(\left[\tilde{\mathbf{A}}_{\mathtt{ZF}}\right]_k\mathbf{g}_{\mathsf{BR},k}\right)$ is given by

$$\mathrm{Var}\left(\left[\tilde{\mathbf{A}}_{\mathtt{ZF}}\right]_k\mathbf{g}_{\mathsf{BR},k}\right) = \mathbb{E}\left\{\left|\left[\tilde{\mathbf{A}}_{\mathtt{ZF}}\right]_k\mathbf{g}_{\mathsf{BR},k}\right|^2\right\}-1 = 0. \quad (83)$$

For $\mathtt{NR}_k$, we have

$$\begin{aligned}\mathtt{NR}_k &= \mathbb{E}\left\{\left|\mathbf{a}_k^T\mathsf{n}_{\mathsf{R}_k}\right|^2\right\},\\ &= \mathbb{E}\left\{\left|\left[\left(\mathbf{G}_{\mathsf{BR}}^H\mathbf{G}_{\mathsf{BR}}\right)^{-1}\mathbf{G}_{\mathsf{BR}}^H\right]_k\mathsf{n}_{R,k}\right|^2\right\},\\ &= \mathbb{E}\left\{\mathrm{Tr}\left(\left[\left(\mathbf{G}_{\mathsf{BR}}^H\mathbf{G}_{\mathsf{BR}}\right)^{-1}\right]_{kk}\right)\right\}. \end{aligned} \quad (84)$$

By using the identity of the book,[34] Lemma 2.10, we have

$$\mathtt{NR}_k = \frac{1}{(N-K)\sigma_{\mathsf{BR}}^2}. \quad (85)$$

$$\begin{aligned}\zeta &= \Pr\left(\mathscr{R}_{\mathsf{OSE}_k}^{\mathtt{MRC}} > \mathscr{R}_{\mathsf{D}_k}^{\mathtt{MRC}} - \frac{1}{2}\log_2\left(1+\min\left(\gamma_{\mathsf{BR}_k}^{\mathtt{MRC}}, \gamma_{\mathsf{RE}_k}^{\mathtt{MRC}}\right)\right)\right),\\ &= \Pr\left(\frac{NP_{\mathsf{S}}\sigma_{\mathsf{BR}}^2}{KP_{\mathsf{S}}\sigma_{\mathsf{BR}}^2+1} \le \frac{\|\mathbf{h}_{\mathsf{RE},k}\|^2 b}{\|\mathbf{h}_{\mathsf{RE},k}\|^2 b + Nc}\right)\Pr\left(\frac{NP_{\mathsf{S}}\sigma_{\mathsf{BR}}^2}{KP_{\mathsf{S}}\sigma_{\mathsf{BR}}^2+1} > 2^{2\left(\mathscr{R}_{\mathsf{D}_k}^{\mathtt{MRC}} - \mathscr{R}_{\mathsf{OSE}_k}^{\mathtt{MRC}}\right)} - 1\right)\right.\\ &\left. + \Pr\left(\frac{NP_{\mathsf{S}}\sigma_{\mathsf{BR}}^2}{KP_{\mathsf{S}}\sigma_{\mathsf{BR}}^2+1} > \frac{\|\mathbf{h}_{\mathsf{RE},k}\|^2 b}{\|\mathbf{h}_{\mathsf{RE},k}\|^2 c + Nd}\right)\Pr\left(\frac{\|\mathbf{h}_{\mathsf{RE},k}\|^2 b}{\|\mathbf{h}_{\mathsf{RE},k}\|^2 c + Nd} > 2^{2\left(\mathscr{R}_{\mathsf{D}_k}^{\mathtt{MRC}} - \mathscr{R}_{\mathsf{OSE}_k}^{\mathtt{MRC}}\right)} - 1\right)\right. . \qquad (75)\end{aligned}$$

$$\begin{aligned}\mathbf{r}_k &= \sqrt{P_{\mathsf{S}}}\left[\left(\mathbf{G}_{\mathsf{BR}}^H\mathbf{G}_{\mathsf{BR}}\right)^{-1}\mathbf{G}_{\mathsf{BR}}^H\right]_k \mathbf{g}_{\mathsf{BR},k}x_k\\ &+ \sqrt{P_{\mathsf{S}}}\sum_{i\neq k}^{K}\left[\left(\mathbf{G}_{\mathsf{BR}}^H\mathbf{G}_{\mathsf{BR}}\right)^{-1}\mathbf{G}_{\mathsf{BR}}^H\right]_k \mathbf{g}_{\mathsf{BR},i}x_i + \left[\left(\mathbf{G}_{\mathsf{BR}}^H\mathbf{G}_{\mathsf{BR}}\right)^{-1}\mathbf{G}_{\mathsf{BR}}^H\right]_k \mathsf{n}_{\mathsf{R}},\\ &= \sqrt{P_{\mathsf{S}}}\left[\tilde{\mathbf{A}}_{\mathtt{ZF}}\right]_k \mathbf{g}_{\mathsf{BR},k}x_k + \sqrt{P_{\mathsf{S}}}\sum_{i\neq k}^{K}\left[\tilde{\mathbf{A}}_{\mathtt{ZF}}\right]_k \mathbf{g}_{\mathsf{BR},i}x_i + \left[\tilde{\mathbf{A}}_{\mathtt{ZF}}\right]_k \mathsf{n}_{\mathsf{R}}, \qquad (80)\end{aligned}$$

Substituting (82), (83), and (85) into (81), the achieved close-expression SINR of the k-th signal stream at R is obtained as

$$\gamma_{\mathsf{BR},k}^{\mathtt{ZF}} = (N-K)P_{\mathsf{S}}\sigma_{\mathsf{BR}}^2. \qquad (86)$$

Secondly, we derive a close-form expression SINR of the transmission link $\mathsf{R}\to\mathsf{D}_k$ by the above same way, namely,

$$\gamma_{\mathsf{RD}_k}^{\mathtt{ZF}} = \frac{(N-K)P_{\mathsf{R}}\hat{\sigma}_{\mathsf{RD},k}^2}{P_{\mathsf{R}}\sum_{i=1}^{K}\sigma_{e,i}^2 + \hat{\sigma}_{\mathsf{RD},k}^2\sum_{i=1}^{K}\frac{1}{\hat{\sigma}_{\mathsf{RD},i}^2}}. \qquad (87)$$

From (86) and (87), we finally obtain (40), i.e., the proof of Theorem 3 is completed.

D. Proof of Theorem 4

To prove Theorem 4, we first compute $\gamma_{\mathsf{RE}_k}^{\mathtt{ZF}}$ from (42). With the help of the book,[34] Lemma 2.10, we obtain items as follows:
The received signal at E_k is

$$\begin{aligned}\left|\mathbf{g}_{\mathsf{RE},k}^T\left[\tilde{\mathbf{B}}_{\mathtt{ZF}}\right]_k\right|^2 &= \\ &\rho_{\mathtt{ZF}}^2\mathbb{E}\left\{\left|\mathbf{g}_{\mathsf{RE},k}^T\left[\hat{\mathbf{G}}_{\mathsf{RD}}^*\left(\hat{\mathbf{G}}_{\mathsf{RD}}^T\hat{\mathbf{G}}_{\mathsf{RD}}^*\right)^{-1}\right]_k\right|^2\right\},\\ &= \|\mathbf{g}_{\mathsf{RE},k}\|^2\rho_{\mathtt{ZF}}^2\mathbb{E}\left\{\left[\left(\hat{\mathbf{G}}_{\mathsf{RD}}^T\hat{\mathbf{G}}_{\mathsf{RD}}^*\right)^{-1}\right]_{kk}\right\},\\ &\approx \frac{\|\mathbf{g}_{\mathsf{RE},k}\|^2\rho_{\mathtt{ZF}}^2}{\hat{\sigma}_{\mathsf{RD},k}^2}\frac{1}{N-K}. \qquad (88)\end{aligned}$$

For $\sum_{i\neq k}^{K}\mathbb{E}\left\{\left|\mathbf{g}_{\mathsf{RE},k}^T\left[\tilde{\mathbf{B}}_{\mathtt{ZF}}\right]_i\right|^2\right\}$, we have

$$\begin{aligned}&\sum_{i\neq k}^{K}\mathbb{E}\left\{\left|\mathbf{g}_{\mathsf{RE},k}^T\left[\tilde{\mathbf{B}}_{\mathtt{ZF}}\right]_i\right|^2\right\}\\ &\quad= \rho_{\mathtt{ZF}}^2\sum_{i\neq k}^{K}\mathbb{E}\left\{\left|\mathbf{g}_{\mathsf{RE},k}^T\left[\hat{\mathbf{G}}_{\mathsf{RD}}^*\left(\hat{\mathbf{G}}_{\mathsf{RD}}^T\hat{\mathbf{G}}_{\mathsf{RD}}^*\right)^{-1}\right]_i\right|^2\right\},\\ &\quad\approx \frac{\|\mathbf{g}_{\mathsf{RE},k}\|^2\rho_{\mathtt{ZF}}^2\sum_{i\neq k}^{K}\frac{1}{\hat{\sigma}_{\mathsf{RD},i}^2}}{N-K}. \qquad (89)\end{aligned}$$

Substituting (88) and (89) into (42), we have

$$\mathscr{R}_{\mathsf{E}_k}^{\mathtt{ZF}} = \frac{1}{2}\log_2\left(1+\min\left((N-K)P_{\mathsf{S}}\sigma_{\mathsf{BR}}^2, \frac{\frac{\|\mathbf{g}_{\mathsf{RE},k}\|^2\rho_{\mathtt{ZF}}^2}{\hat{\sigma}_{\mathsf{RD},k}^2}\frac{1}{N-K}}{\frac{\|\mathbf{g}_{\mathsf{RE},k}\|^2\rho_{\mathtt{ZF}}^2\sum_{i\neq k}^{K}\frac{1}{\hat{\sigma}_{\mathsf{RD},i}^2}}{N-K}+1}\right)\right). \qquad (90)$$

Next, we perform the same approach as for Theorem 2. Finally, we easily obtain the result as in Theorem 4.

Acknowledgments

This research is conducted within the framework of science and technology projects at institutional level of Quy Nhon University under the project code T2022.760.16.

REFERENCES

1. J. G. Andrews, S. Buzzi, W. Choi, S. V. Hanly, A. Lozano, A. C. Soong, J. C. Zhang. What will 5G be?, *IEEE Journal on Selected Areas in Communications*, **2014**, *32*(6), 1065– 1082.

2. C.-X. Wang, F. Haider, X. Gao, X.-H. You, Y. Yang, D. Yuan, H. Aggoune, H. Haas, S. Fletcher, E. Hepsaydir. Cellular architecture and key technologies for 5G wireless communication networks, *IEEE Communications Magazine,* **2014**, *52*(2), 122–130.

3. T. L. Marzetta. Noncooperative cellular wireless with unlimited numbers of base station antennas, *IEEE Transactions on Wireless Communications*, **2010**, *9*(11), 3590–3600.

4. E. G. Larsson, O. Edfors, F. Tufvesson, T. L. Marzetta. Massive mimo for next generation wireless systems, *IEEE Communications Magazine*, **2014**, *52*(2), 186–195.

5. H. Q. Ngo, E. G. Larsson, T. L. Marzetta. Energy and spectral efficiency of very large multiuser mimo systems, *IEEE Transactions on Communications*, **2013**, *61*(4), 1436–1449.

6. H. Yang, T. L. Marzetta. Performance of conjugate and zero-forcing beamforming in large-scale antenna systems, *IEEE Journal on Selected Areas in Communications*, **2013**, *31*(2), 172–179.

7. X. Chen, L. Lei, H. Zhang, C. Yuen. *On the secrecy outage capacity of physical layer security in large-scale mimo relaying systems with imperfect CSI,* the 50th IEEE International Conference on Communications University of Sydney Australia, June 2014.

8. J. Zhu, R. Schober, V. K. Bhargava. Linear precoding of data and artificial noise in secure massive mimo systems, *IEEE Transactions on Wireless Communications*, **2016**, *15*(3), 2245–2261.

9. D. Kapetanovic, G. Zheng, F. Rusek. Physical layer security for massive mimo: An overview on passive eavesdropping and active attacks, *IEEE Communications Magazine,* **2015**, *53*(6), 21–27.

10. T. Liu, S. Shamai. A note on the secrecy capacity of the multiple-antenna wiretap channel, *IEEE Transactions on Information Theory*, **2009**, *55*(6), 2547–2553.

11. F. Oggier, B. Hassibi. The secrecy capacity of the mimo wiretap channel, *IEEE Transactions on Information Theory,* **2011**, *57*(8), 4961–4972.

12. X. Chen, H. - H. Chen. Physical layer security in multi-cell miso downlinks with incomplete CSI—a unified secrecy performance analysis, *IEEE Transactions on Signal Processing,* **2014**, *62*(23), 6286–6297.

13. L. Dong, Z. Han, A. P. Petropulu, H. V. Poor. Improving wireless physical layer security via cooperating relays, *IEEE transactions on signal processing*, **2010**, *58*(3), 1875–1888.

14. X. Chen, C. Zhong, C. Yuen, H. - H. Chen. Multi-antenna relay aided wireless physical layer security, *IEEE Communications Magazine*, **2015**, *53*(12), 40–46.

15. M. Pei, J. Wei, K.-K. Wong, X. Wang. Masked beamforming for multiuser MIMO wiretap channels with imperfect CSI, *IEEE Transactions on Wireless Communications*, **2012**, *11*(2), 544–549.

16. X. Wang, K. Wang, X.-D. Zhang. Secure relay beamforming with imperfect channel side information, *IEEE Transactions on Vehicular Technology,* **2013**, *62*(4), 2140–2155.

17. J. Jose, A. Ashikhmin, T. L. Marzetta, S. Vishwanath. Pilot contamination and precoding in multi-cell tdd systems, *IEEE Transactions on Wireless Communications*, **2011**, *10*(8), 2640–2651.

18. N. Yang, H. A. Suraweera, I. B. Collings, C. Yuen. Physical layer security of TAS/MRC with antenna correlation, *IEEE Transactions on Information Forensics and Security*, **2013**, *8*(1), 254–259.

19. X. Chen, Y. Zhang. Mode selection in MU - MIMO downlink networks: A physical-layer security perspective, *IEEE Systems Journal*, **2017**, *11*(2), 1128–1136.

https://doi.org/10.52111/qnjs.2021.16307

20. H.-M. Wang, Q. Yin, X.-G. Xia. Distributed beamforming for physical-layer security of two-way relay networks, *IEEE Transactions on Signal Processing,* **2012**, *60*(7), 3532–3545.

21. G. Zheng, L.-C. Choo, K.-K. Wong. Optimal cooperative jamming to enhance physical layer security using relays, *IEEE Transactions on Signal Processing,* **2011**, *59*(3), 1317–1322.

22. J. Huang, A. L. Swindlehurst. Cooperative jamming for secure communications in mimo relay networks, *IEEE Transactions on Signal Processing*, **2011**, *59*(10), 4871–4884.

23. M. Shakiba-Herfeh, A. Chorti, H. V. Poor. *Physical layer security: Authentication, integrity, and confidentiality,* in Physical Layer Security, Springer, 2021.

24. N. D. Dung, V. N. Q. Bao *et al.* Secrecy performance of massive mimo relay-aided downlink with multiuser transmission, *IET Communications*, **2019**, *13*(9), 1207–1217.

25. Y. Fu, W. P. Zhu, C. Liu. *Rate optimization for relay precoding design with imperfect CSI in two-hop mimo relay networks,* the 73rd Vehicular Technology Conference, Budapest, Hungary, May 2011.

26. C. B. Chae, T. Tang, R. W. Heath, S. Cho. Mimo relaying with linear processing for multiuser transmission in fixed relay networks, *IEEE Transactions on Signal Processing*, **2008**, *56*(2), 727–738.

27. D. W. K. Ng, E. S. Lo, R. Schober. Robust beamforming for secure communication in systems with wireless information and power transfer, *IEEE Transactions Wireless Communications,* **2014**, *13*(2), 544–549.

28. X. Wang, K. Wang, X. D. Zhang. Secure relay beamforming with imperfect channel side information, *IEEE Transactions on Vehicular Technology*, **2013**, *62*(5), 2140–2155.

29. Y. Zou, X. Wang, W. Shen. Optimal relay selection for physical-layer security in cooperative wireless networks, *IEEE Journal on Selected Areas in Communications*, **2013**, *31*(10), 2099–2111.

30. T. Liu, S. Shamai. A note on the secrecy capacity of the multiple-antenna wiretap channel, *IEEE Transactions on Information Theory*, **2009**, *55*(6), 2547–2553.

31. J. Huang, A. L. Swindlehurst. Cooperative jamming for secure communications in mimo relay networks, *IEEE Transactions on Signal Processing*, **2011**, *59*(10), 4871–4884.

32. H. Yin, D. Gesbert, M. Filippou, Y. Liu. A coordinated approach to channel estimation in large-scale multiple-antenna systems, *IEEE Journal on Selected Areas in Communications*, **2013**, *31*(2), 264–273.

33. T. L. Marzetta. Noncooperative cellular wireless with unlimited numbers of base station antennas, *IEEE Transactions on Wireless Communications*, **2010**, *9*(11), 3590–3600.

34. A. M. Tulino, S. Verdú. Random matrix theory and wireless communications, *Foundations and Trends ® in Communications and Information Theory,* **2004**, *1*(1), 1–182.

35. B. Hassibi, B. M. Hochwald. How much training is needed in multiple-antenna wireless links?, *IEEE Transactions on Information Theory,* **2003**, *49*(4), 951–963.

https://doi.org/10.52111/qnjs.2022.16307

TẠP CHÍ KHOA HỌC
TRƯỜNG ĐẠI HỌC QUY NHƠN

Ổn định trung bình mũ của hệ ngẫu nhiên rời rạc có độ trễ biến thiên theo thời gian, thông qua cách tiếp cận dựa trên IPR

Phạm Kỳ Anh và Trần Ngọc Nguyên*

Khoa Toán và Thống kê, Trường Đại Học Quy Nhơn, Việt Nam

Ngày nhận bài: 16/03/2022; Ngày nhận đăng: 07/06/2022

TÓM TẮT

Kỹ thuật IPR (Internally Positive Representation) giúp chuyển bài toán xét độ ổn định của hệ tuyến tính không dương thành xét độ ổn định của hệ tuyến tính dương mà ma trận hệ số được xây dựng từ việc trích xuất các ma trận của hệ thống cần xem xét. Trong bài báo này, chúng tôi trình bày sự phát triển của cách tiếp cận dựa trên IPR cho một lớp các hệ ngẫu nhiên rời rạc với trễ thời gian. Nghiên cứu của chúng tôi cố gắng tìm một ước lượng α mũ cho giá trị tuyệt đối của kỳ vọng của vectơ trạng thái. Để làm được điều này, đầu tiên, chúng tôi xem xét tính ổn định mũ của một hệ ngẫu nhiên rời rạc dương có độ trễ thay đổi theo thời gian. Ở đây cả tính dương và tính ổn định hàm mũ được xem xét theo nghĩa kỳ vọng. Tiếp theo, bằng cách sử dụng kỹ thuật IPR, chúng tôi phát triển kết quả thu được cho hệ ngẫu nhiên không dương. Cuối cùng, chúng tôi đưa ra một số ví dụ minh họa cho tính hiệu quả của phương pháp vừa phát triển.

Từ khóa: *Internally Positive Representation, ước lượng trạng thái trung bình mũ, hệ ngẫu nhiên rời rạc, trễ biến thiên theo thời gian bị chặn.*

* *Tác giả liên hệ chính.*
Email: tranngocnguyen@qnu.edu.vn

https://doi.org/10.52111/qnjs.2022.16308

JOURNAL OF SCIENCE
QUY NHON UNIVERSITY

Exponential mean stability of stochastic discrete-time systems with time-varying delays via an IPR-based approach

Pham Ky Anh and Tran Ngoc Nguyen*

Department of Mathematics and Statistics, Quy Nhon University, Binh Dinh, Vietnam

Received: 16/03/2022; Accepted: 07/06/2022

ABSTRACT

The internally positive representation (IPR) technique helps to reformulate the stability problem of non-positive linear systems into the stability problem of a class of positive linear systems, whose matrices are constructed from the extraction of matrices of the considered system. In this paper, we present a development of the IPR-based approach to a class of stochastic discrete-time systems with time-delays. Our study is devoted to the problem of finding an α-exponential estimate of the absolute of the expectation of the state vector. For this, firstly, we investigate the the exponential stability problem for a class of positive stochastic discrete-time systems with time-varying delays. Here, both the positivity and the exponential stability are considered in the sense of expectation. Next, by using the IPR technique, we develop the obtained result to a class of non-positive stochastic systems. Finally, a numerical example is given to illustrate the effectiveness of the developed approach.

Keywords: *Internally positive representation (IPR), exponential mean state estimate, stochastic discrete-time systems, bounded time-varying delay.*

1. INTRODUCTION

The IPR-based approach for analyzing the stability of linear dynamical systems has been proposed by the authors in.[1–3] It includes two main steps: (1) Constructing a positive linear system, whose matrices are designed from the extraction of matrices of the considered system, such that the stability of a considered system is followed from the stability of the constructed positive system; (2) Analyzing the stability of the constructed positive linear system. In five recent years, this approach has been developed to some classes of linear systems with time-delays, e.g., continuous-time linear systems with time-varying delays,[4,5] singular linear systems with time-varying delays,[6–8] difference equations with constant time-delays.[9] To the best of our knowledge, so far, there has not been any result which reported on the IPR-based approach to the stability problem of classes of stochastic systems with time-delays. This unsolved problem, therefore, will be investigated in this paper.

Because of a vast applicability in many areas such as finance, economics, biology, physics, communication,. . . , the topic on stability analysis of stochastic systems has been an attractive research issue for past decades, see, e.g.,[10–14] and the references therein. Rather than the asymptotic stability where guarantees only the convergence of the state vector, the exponential stability with a given rate and a known factor can provide more quantitative estimates, which is often required in practical applications. Most of existing results reported on two types of the exponential stability for classes of stochastic systems, including: (1) p-th moment exponential stability with $p \geq 2$ (in the case $p = 2$, it is referred as mean square exponential stability);[15–19] (2) Almost-sure exponential stability.[20–23] In 2014, Bolzern et al.,[13] proposed and investigated the 1-th moment exponential stability (i.e., the exponential mean stability) for a class of Markov jump systems. They have also shown that the estimate of the expectation of the state vector obtained from the exponential mean stability is more accurate than the one obtained from the exponential mean square stability. Recently, the problem of exponential mean stability has also been developed to some classes of positive Markov jump systems with/without time-delays.[24–26] However, it seems that, so far, there

**Corresponding author.*
Email: tranngocnguyen@qnu.edu.vn

https://doi.org/10.52111/qnjs.2021.163078

has not been any result reported on the exponential mean stability problem for classes of non-Markov jump stochastic systems.

Within ten recent years, a considerable number of research attention has been paid to the problem on stability analysis of classes of positive linear systems with time-varying delays. There are two popular approaches, including: (1) the approach based on the solution comparisons between a positive system with time-varying delays and the one with constant time-delays,[27–37] and (2) the approach based on the direct comparison between the system solution and a constructed exponential function.[37–42] With regarding to the topic on the stability analysis of positive stochastic systems, almost existing works have reported only on classes of positive stochastic systems of the Markov jump type. Because coefficient matrices of a positive Markov jump system belong to a predefined set of Metzler or nonnegative matrices, under a positive initial condition, its state vector is always positive.[13,43–47] Very recently, Liang and Jin,[52] have considered two other classes of positive stochastic (non-Markov) systems, these are more general notions of positivity for classes of stochastic (non-Markov) systems: the positivity in the sense of probability and the positivity in the sense of expectation. The former notion means that, for a predefined threshold, m, between 0 and 1, from any positive initial condition, there exists a time point such that from this time point, the probability that state vectors of the system are non-negative is not less than the threshold m. The latter notion is used for stochastic systems in which the expectation of state vectors is always non-negative for any positive initial condition. These two notions of positive stochastic systems have not yet been developed to any discrete-time or continuous-time stochastic systems with time delays.

Motivated by these discussions, in this paper, we will consider a class of linear stochastic discrete-time systems with time-varying delays which can be seen as a discrete-time version of stochastic continuous-time systems with time-varying delays and random uncertainties. An IPR is firstly constructed to deal with the α-exponential mean estimate for an arbitrary (not necessarily positive) system. We then develop results about the exponential mean stability for positive stochastic systems. Under the effect of stochastic factors, the system is not positive in the normal sense as in deterministic systems. However, we will show that under some conditions on coefficient matrices and stochastic process, the system is still positive in the sense of expectation (see Definition 4.1 below). From this property, we will study the monotonicity of the expectation of the state vector of stochastic systems. As a result, for the first time, a solution comparison principle for linear stochastic discrete-time systems with time-varying delays will be introduced. By using this solution comparison and a state transformation, we will derive an α-exponential mean estimate for state vector of positive stochastic systems. A sufficient condition for the α-exponential mean boundedness of positive stochastic systems (in the sense of expectation) which is based on the spectral property of the coefficient matrices is then introduced. This new approach will give us an estimation with time-varying coefficients. For the sake of demonstrating the effectiveness of the IPR approach, we also introduce another result about the α-exponential mean boundedness of linear stochastic systems which is based on positive "upper bound" systems. Together with theoretical results, a numerical example is also conducted to show that the approach based on the IPR will give us i) a less conservative condition for the exponential mean stability of the stochastic discrete-time system with time-varying delays than the approach based on an "upper bound" system, and ii) a more accurate α-exponential mean estimates of state vector of the system. Our contributions in this paper can be summarized as below:

- For the first time, an IPR is applied for a class of stochastic discrete-time systems with time-varying delays to derive an α-exponential mean estimate for state vectors.
- The notion of the positivity in the sense of expectation is introduced for a class of linear stochastic discrete-time systems with time-varying delays. We then prove some sufficient conditions for stochastic systems to be positive in the sense of expectation. A solution comparison between positive stochastic systems with time-varying delays is established. This comparison is then combined with a state transformation to derive an α-exponential mean estimate for positive stochastic discrete-time systems with time-varying delays. This is the key tool for the IPR method.

The paper is organized as below. The next section introduces notations, definitions and some preliminary results. The IPR approach is presented in Section 3 to derive an α-exponential mean estimate of non-positive linear stochastic discrete-timeys stems. Section 4 is devoted

https://doi.org/10.52111/qnjs.2022.16308

to positivity and solution comparison principle of linear stochastic systems. In addition, an α-exponential mean estimate for positive stochastic systems is also established in this section. Section 5 introduces another approach to obtain an α-exponential mean estimate for stochastic systems which is based on "upper bound" systems. An illustrative example will be presented in Section 6 to verify theoretical results. Section 7 concludes the paper.

2. SYSTEM, NOTATIONS AND DEFINITIONS

Notations: $\mathbb{N}$, $\mathbb{R}^n$ and $\mathbb{R}^n_{0,+}$ are respectively the set of nonnegative integers, the n-dimensional vector space and the nonnegative orthant in $\mathbb{R}^n$; $e = [1\ 1\ \cdots\ 1]^\top \in \mathbb{R}^n$; for two vectors $x = [x_1\ x_2\ \cdots\ x_n]^\top$, $y = [y_1\ y_2\ \cdots\ y_n]^\top$ in $\mathbb{R}^n$, two $n \times n$-matrices $A = [a_{ij}]$, $B = [b_{ij}]$, $x \prec y$ ($x \preceq y$) means that $x_i < y_i$ ($x_i \leq y_i$), $\forall i = 1, \cdots, n$ and $A \prec B$ ($A \preceq B$) means that $a_{ij} < b_{ij}$ ($a_{ij} \leq b_{ij}$), $\forall i, j = 1, \cdots, n$; A is a nonnegative matrix if $0 \preceq A$; $x \succeq y$ ($A \succeq B$) means that $y \preceq x$ ($B \preceq A$); $\rho(A) = \max\{|\lambda| : \lambda \in \sigma(A)\}$ is the spectral radius of A; I_n is the identity matrix of size n. The maximum, minimum of a finite set of vectors (of matrices) are understood componentwise. Similarly, the absolute value of a matrix A (or a vector x) is also understood componentwise.

Let (Ω, σ, P) be a basic probability space. The notation $\mathbb{E}\zeta$ denotes the componentwise expectation of a random variable $\zeta = [\zeta_1\ \zeta_2\ \cdots \zeta_n]^\top$ in $\mathbb{R}^n$, i.e. $\mathbb{E}\zeta = [\mathbb{E}\zeta_1\ \mathbb{E}\zeta_2\ \cdots \mathbb{E}\zeta_n]^\top$. For a positive integer $h \in \mathbb{N}$, let $\mathcal{C}([-h, 0], \mathbb{R}^n)$ be the set of all functions $\phi : \{-h, -h+1, \cdots, 0\} \to \mathbb{R}^n$. Let $\mathcal{C}_\sigma([-h, 0], \mathbb{R}^n)$ be the family of $\mathcal{C}([-h, 0], \mathbb{R}^n)$-valued random variables on (Ω, σ, P) such that $\max_{s \in \{-h, -h+1, \cdots, 0\}} |\mathbb{E}\phi(s)| < \infty$, for any $\phi(\cdot) \in \mathcal{C}_\sigma([-h, 0], \mathbb{R}^n)$.

The result in this paper can be easily developed for linear stochastic discrete-time systems with multiple time-varying delays. Hence, for the sake of simplicity, in this paper, we consider the following linear stochastic discrete-time system with a time-varying delay

$$\begin{aligned} x(t+1) =& [A_0 + \xi(t)B_0]x(t) \\ &+ [A_1 + \xi(t)B_1]x(t - h_1(t)),\ t \in \mathbb{N}, \\ x(s) =& \phi(s),\ s \in \{-h, -h+1, \cdots, 0\}, \end{aligned} \tag{1}$$

where $x(t) \in \mathbb{R}^n$ is the state vector; $\xi(t)$ is a scalar random process satisfying $\mathbb{E}\xi(t) = \hat{\xi}$ $\forall t \in \{-h, -h+1, \cdots, 0\}$, for some $\hat{\xi} \in \mathbb{R}$ and $\xi(0), \xi(1), \cdots$ are assumed to be mutually independent; A_0, A_1, B_0 and B_1 are four matrices in $\mathbb{R}^{n \times n}$; an unknown time-varying delay $h_1(t) \in [0, h]$, where $h > 0$ is a known integer and $\phi \in \mathcal{C}_\sigma([-h, 0], \mathbb{R}^n)$ is an unknown random function satisfying

$$|\mathbb{E}\phi(s)| \preceq \overline{\phi}(s),\ s \in \{-h, -h+1, \cdots, 0\}, \tag{2}$$

where $\overline{\phi} \in \mathcal{C}([-h, 0], \mathbb{R}^n_{0,+})$ is a known function. Let us denote by $x(t, \phi)$ the unique solution, under the initial value function $\phi(\cdot)$, of system (1). The process $\xi(t)$ whose the expectation equals to 0 is considered very often in discrete-time stochastic systems, e.g..[17,48–50] In this paper, we will study the system (1) under a more general stochastic process $\xi(t)$.

Inspired by the notion of exponential mean stability in,[13] we introduce the following definition of α-exponentially mean boundedness for the stochastic system (1).

Definition 2.1. Let $\alpha > 1$ be a positive real number. System (1) is said to be α-exponentially mean bounded if there exist a vector-valued function $\eta(t, A_0, B_0, A_1, B_1, h, \bar{\phi}, \hat{\xi}) \in \mathbb{R}^n_{0,+}$, $t \in \mathbb{N}$ such that

$$|\mathbb{E}x(t, \phi)| \preceq \eta(t, \cdot)\alpha^{-t},\quad t \in \mathbb{N}. \tag{3}$$

The function $\eta(\cdot)$ is called the factor function. In the case where system (1) is α-exponentially mean bounded, for some $\alpha > 1$, an estimation in the form (3) is called an α-exponential mean estimate of this system.

Before introducing main results of this paper in next sections, we recall a well-known result related to properties of Schur matrices.

Lemma 2.2 ([51])**.** Let M be a nonnegative matrix in $\mathbb{R}^{n \times n}$. Then M is Schur matrix, i.e. $\rho(M) < 1$, if and only if one of the following conditions holds: i) there exits an vector $z \in \mathbb{R}^n_+$ such that $(M - I_n)z \prec 0$; ii) $(I_n - M)^{-1} \succeq 0$.

3. AN IPR APPROACH FOR α-EXPONENTIAL MEAN BOUNDEDNESS OF NON-POSITIVE STOCHASTIC SYSTEMS

In this section, by using an IPR approach for the system (1), we will establish an exponential mean estimate for this system. For any $x \in \mathbb{R}^n$ and $M \in \mathbb{R}^{n \times n}$, let us introduce the following min-positive representation,[9]

$$\pi(x) = \begin{bmatrix} x^+ \\ x^- \end{bmatrix}, \tag{4}$$

where $x^+ = \max\{x, 0\}, x^- = \max\{-x, 0\}$,

https://doi.org/10.52111/qnjs.2021.16308

and

$$\Pi(M) = \begin{bmatrix} M^+ & M^- \\ M^- & M^+ \end{bmatrix}, \tag{5}$$

where $M^+ = \max\{M, 0\}, M^- = \max\{-M, 0\}$.

Let us consider the following stochastic system

$$\begin{aligned} \hat{x}(t+1) =& \Pi\left(A_0 + \xi(t)B_0\right)\hat{x}(t) \\ &+ \Pi\left(A_1 + \xi(t)B_1\right)\hat{x}(t - h_1(t)),\ t \in \mathbb{N}, \\ \hat{x}(s) =& \pi(\phi(s)),\ s \in \{-h, -h+1, \cdots, 0\}. \end{aligned} \tag{6}$$

The next lemma gives us some properties of the min-positive representation.

Lemma 3.1. Let $x(t, \phi)$ and

$$\hat{x}(t, \phi) = [\hat{x}^1(t, \pi(\phi))\ \hat{x}^2(t, \pi(\phi))] \in \mathbb{R}^{2n}$$

be respectively the solution of (1) and (6). For all $t \in \mathbb{N}$, we then have

(a) $x(t, \phi) = x(t, \phi)^+ - x(t, \phi)^-$ and $|x(t, \phi)| = x(t, \phi)^+ + x(t, \phi)^-$;

(b) $M = M^+ - M^-$ and $|M| = M^+ + M^-$;

(c) $x(t, \phi) = \hat{x}^1(t, \pi(\phi)) - \hat{x}^2(t, \pi(\phi))$.

Proof. The first two properties can be verified easily. The proof of (c) can be found in,[9] Theorem 6. □

For each $t \in \mathbb{N}$, Lemma 3.1-(c) implies that

$$\begin{aligned} |\mathbb{E}x(t, \phi)| &= |\mathbb{E}\hat{x}^1(t, \pi(\phi)) - \mathbb{E}\hat{x}^2(t, \pi(\phi))| \\ &\leq |\mathbb{E}\hat{x}^1(t, \pi(\phi))| + |\mathbb{E}\hat{x}^2(t, \pi(\phi))|. \end{aligned} \tag{7}$$

We will prove, in the next section (see Lemma 4.2-i)), that the system (6) is positive in the sense of expectation. In particular, we have

$$|\mathbb{E}\hat{x}(t, \pi(\phi))| = \mathbb{E}\hat{x}(t, \pi(\phi)) \succeq 0,\ \forall t \in \mathbb{N}.$$

Moreover, we will prove (see Theorem 4.4 below) that for any $\alpha > 1$ which satisfies

$$\rho\left(\alpha\Pi\left(A_0 + \hat{\xi}B_0\right) + \alpha^{h+1}\Pi\left(A_1 + \hat{\xi}B_1\right)\right) < 1,$$

we have

$$\mathbb{E}\hat{x}(t, \pi(\phi)) \preceq \hat{z}(t, \hat{\phi})\alpha^{-t},\ t \in \mathbb{N}, \tag{8}$$

where $\hat{\phi} \in \mathcal{C}([-h, 0], \mathbb{R}^n)$ will be defined later and $\hat{z}(t, \hat{\phi})$ is the solution of the following system

$$\begin{aligned} \hat{z}(t+1) =& \alpha\Pi\left(A_0 + \xi(t)B_0\right)\hat{z}(t) \\ &+ \alpha^h\Pi\left(A_1 + \xi(t)B_1\right)\hat{z}(t - h_1(t)), \\ & t \in \mathbb{N}, \\ \hat{z}(s) =& \hat{\phi}(s),\ s \in \{-h, -h+1, \cdots, 0\}. \end{aligned} \tag{9}$$

In addition, $\hat{z}(t, \cdot)$ is a non-increasing function. This means that the system (6) is α-exponentially mean bounded.

By combining the previous facts, we obtain the following theorem which gives us a sufficient condition for the α-exponential mean boundedness of system (1).

Theorem 3.2. Let $\alpha > 1$ be such that

$$\rho\left(\alpha\Pi\left(A_0 + \hat{\xi}B_0\right) + \alpha^{h+1}\Pi\left(A_1 + \hat{\xi}B_1\right)\right) < 1. \tag{10}$$

Then, system (1) is α-exponentially mean bounded and the α-exponential mean estimate is given by

$$|\mathbb{E}x(t, \phi)| \preceq \bar{z}(t, \hat{\phi})\alpha^{-t}, \tag{11}$$

where $\bar{z}(t, \hat{\phi}) := \mathbb{E}\hat{z}^1(t, \hat{\phi}) + \mathbb{E}\hat{z}^2(t, \hat{\phi})$ and $\hat{z}(t, \hat{\phi}) = [\hat{z}^1(t, \hat{\phi})\ \hat{z}^2(t, \hat{\phi})] \in \mathbb{R}^{2n}$ is the solution of (9). In addition, the factor function $\bar{z}(\cdot, \hat{\phi})$ is non-increasing.

In the next section, we will establish an α-exponential mean estimate for positive stochastic discrete-time systems in the sense of expectation from which the result in Theorem 3.2 is followed.

4. AN α-EXPONENTIAL MEAN ESTIMATE FOR POSITIVE STOCHASTIC DISCRETE-TIME SYSTEMS AND ITS APPLICATIONS

Different from positive Markov jump linear systems, under the influence of stochastic uncertainty $\xi(t)$, the system (1) might not be positive even if the initial value function belongs to the nonnegative orthant. From this fact and the notion of positive systems, see, e.g.,[52,53] we introduce the following definition of positive stochastic systems in the sense of expectation.

Definition 4.1. System (1) is said to be positive in the sense of expectation if for any random initial value function $\phi \in \mathcal{C}_\sigma([-h, 0], \mathbb{R}^n)$ such that $\mathbb{E}\phi(\cdot) \succeq 0$, we then have $\mathbb{E}x(t, \phi) \succeq 0$.

From now on, for simplicity, sometimes we say that a stochastic system is positive to mean that this system is positive in the sense of expectation. We will prove that under some assumptions related to the coefficient matrices, the random process and the initial value function, system (1) is positive. From the positivity of this system, we will apply solution comparison-based methods to establish relations between positive

systems, see, e.g..[34,54] More specifically, this approach will make a comparison between state vectors of the stochastic discrete-time system with time-varying delay (1) with state vectors of the following "similar" constant time delay system

$$\begin{aligned} y(t+1) =&[A_0+\xi(t)B_0]y(t) \\ &+[A_1+\xi(t)B_1]y(t-h),\ t\in\mathbb{N}, \\ y(s) =&\psi(s),\ s\in\{-h,-h+1,\cdots,0\}, \end{aligned} \tag{12}$$

where $\psi\in\mathcal{C}_\sigma([-h,0],\mathbb{R}^n)$ is a random function with known expectation. In addition, the system (1) is also compared with the following "upper" system

$$\begin{aligned} \bar{x}(t+1) =&[\bar{A}_0+\xi(t)\bar{B}_0]\bar{x}(t) \\ &+[\bar{A}_1+\xi(t)\bar{B}_1]\bar{x}(t-h_1(t)),\ t\in\mathbb{N}, \\ \bar{x}(s) =&\phi(s),\ s\in\{-h,-h+1,\cdots,0\}, \end{aligned} \tag{13}$$

where $\bar{A}_0,\bar{A}_1,\bar{B}_0$ and $\bar{B}_1$ are matrices in $\mathbb{R}^{n\times n}$ such that $0\preceq A_0+\hat{\xi}B_0\preceq\bar{A}_0+\hat{\xi}\bar{B}_0$ and $0\preceq A_1+\hat{\xi}B_1\preceq\bar{A}_1+\hat{\xi}\bar{B}_1$. The positivity and the monotonic property of these systems will be applied to derive an α-exponential mean estimate for the positive stochastic system (1).

4.1. Positivity and solution comparisons

In this section, we will prove the positivity of systems (1), (12) and (13). From this property, we then derive some solution comparisons between these systems. The main results of this section are presented in the next lemma.

Lemma 4.2. Let us assume that the matrices A_0,A_1,B_0,B_1 and the random process $\xi(t)$ satisfy $A_0+\mathbb{E}\xi(t)B_0\succeq 0$ and $A_1+\mathbb{E}\xi(t)B_1\succeq 0$ for all $t\in\mathbb{N}$. Then, the following assertions hold true.

i) Assume that $\mathbb{E}\phi(\cdot)\succeq 0$ and $\mathbb{E}\psi(\cdot)\succeq 0$. Then, systems (1), (12) and (13) are positive in the sense of expectation.

ii) For all $\phi_1,\phi_2\in\mathcal{C}_\sigma([-h,0],\mathbb{R}^n)$ such that $0\preceq\mathbb{E}\phi_1(s)\preceq\mathbb{E}\phi_2(s)\ \forall s\in\{-h,-h+1,\cdots,0\}$, then

$$\mathbb{E}x(t,\phi_1)\preceq\mathbb{E}x(t,\phi_2)\ \forall t\in\mathbb{N}. \tag{14}$$

iii) For all $\phi\in\mathcal{C}_\sigma([-h,0],\mathbb{R}^n)$ such that $\mathbb{E}\phi(\cdot)\succeq 0$, we have

$$\mathbb{E}x(t,\phi)\preceq\mathbb{E}\bar{x}(t,\phi)\ \forall t\in\mathbb{N}. \tag{15}$$

iv) For every random function $\delta\in\mathcal{C}_\sigma([-h,0],\mathbb{R}^n)$ such that $\mathbb{E}\delta(t+1)\preceq\mathbb{E}\delta(t)$ for all $t\in\{-h,-h+1,\cdots,-1\}$ and $(A_1+\hat{\xi}B_1)\mathbb{E}\delta(-h)+(A_0+\hat{\xi}B_0)\mathbb{E}\delta(0)\preceq\mathbb{E}\delta(0)$, we then have

iv)-1) $\mathbb{E}y(t+1,\delta)\preceq\mathbb{E}y(t,\delta),\ \forall t\in\mathbb{N}$,

iv)-2) $\mathbb{E}x(t,\delta)\preceq\mathbb{E}y(t,\delta),\ \forall t\in\mathbb{N}$,

where $x(t,\delta)$ and $y(t,\delta)$ are respectively solutions of systems (1) and (12) under the initial conditions $\phi(s)=\psi(s)=\delta(s)$ for all $s\in\{-h,-h+1,\cdots,0\}$.

Proof. *i)* We just need to prove the positivity in the sense of expectation of the system (1). The positivity of two systems (12) and (13) follows as a particular case of (1). From the initial condition that $\mathbb{E}\phi(t)\succeq 0$, for all $t\in\{-h,-h+1,\cdots,0\}$ and noting that $\mathbb{E}\xi(0)=\hat{\xi}$, $A_0+\hat{\xi}B_0\succeq 0$ and $A_1+\hat{\xi}B_1\succeq 0$, we then have

$$\begin{aligned} &\mathbb{E}x(1,\phi) \\ &=\mathbb{E}\{[A_0+\xi(0)B_0]x(0) \\ &\quad+[A_1+\xi(0)B_1]x(-h_1(0))\} \\ &=(A_0+\hat{\xi}B_0)\mathbb{E}\phi(0)+(A_1+\hat{\xi}B_1)\mathbb{E}\phi(-h_1(0)) \\ &\succeq 0. \end{aligned}$$

Suppose that $\mathbb{E}x(t,\phi)\succeq 0$ for all $t\in\{-h,-h+1,\cdots,t_0\}$ for some $t_0\in\mathbb{N}_0$. We now prove that $\mathbb{E}x(t_0+1,\phi)\succeq 0$. Indeed, from the assumption that $\mathbb{E}\xi(t_0)=\hat{\xi}$, $A_0+\hat{\xi}B_0\succeq 0$, $A_1+\hat{\xi}B_1\succeq 0$, and noting that $0\le h_1(t_0)\le h$, we then get from the induction hypothesis that

$$\begin{aligned} \mathbb{E}x(t_0+1,\phi) =&\mathbb{E}\{[A_0+\xi(t_0)B_0]x(t_0) \\ &+[A_1+\xi(t_0)B_1]x(t_0-h_1(t_0))\} \\ =&(A_0+\hat{\xi}B_0)\mathbb{E}x(t_0) \\ &+(A_1+\hat{\xi}B_1)\mathbb{E}x(t_0-h_1(t_0)) \\ \succeq&0. \end{aligned}$$

By induction argument, we obtain the conclusion.
ii) Let us denote

$$e(t,\hat{\phi})=x(t,\phi_2)-x(t,\phi_1),$$

where

$$\hat{\phi}(t)=\phi_2(t)-\phi_1(t),\forall t\in\{-h,-h+1,\cdots,0\}.$$

It can be verified that $e(t,\hat{\phi})$ is the solution of the following linear stochastic discrete-time system

$$\begin{aligned} e(t+1) =&[A_0+\xi(t)B_0]e(t) \\ &+[A_1+\xi(t)B_1]e(t-h_1(t)),\ t\in\mathbb{N}, \\ e(s) =&\hat{\phi}(s),\ s\in\{-h,-h+1,\cdots,0\}, \end{aligned}$$

https://doi.org/10.52111/qnjs.2021.16308

By using assertion i) with noting that

$$\mathbb{E}\hat{\phi}(t) = \mathbb{E}\phi_2(t) - \mathbb{E}\phi_1(t) \succeq 0 \quad \forall t \in \{-h, -h+1, \cdots, 0\},$$

the above system is positive in the sense of expectation. This means that

$$\mathbb{E}e(t, \hat{\phi}) = \mathbb{E}x(t, \phi_2) - \mathbb{E}x(t, \phi_1) \succeq 0$$

from which the conclusion ii) follows.
iii) Let $t \in \mathbb{N}$. By using the positivity of systems (1), (13), and the assumption that

$$0 \preceq A_0 + \hat{\xi}B_0 \preceq \bar{A}_0 + \hat{\xi}\bar{B}_0,$$

$$0 \preceq A_1 + \hat{\xi}B_1 \preceq \bar{A}_1 + \hat{\xi}\bar{B}_1,$$

taking the expectation on both sides of (1) with noting that $\mathbb{E}\xi(t) = \hat{\xi}$, $\mathbb{E}x(t) \succeq 0$ and $\mathbb{E}x(t - h_1(t)) \succeq 0$, one gets

$$\begin{aligned}
\mathbb{E}x(t+1, \phi) =& \mathbb{E}\{[A_0 + \xi(t)B_0]x(t) \\
&+ [A_1 + \xi(t)B_1]x(t - h_1(t))\} \\
=& (A_0 + \hat{\xi}B_0)\mathbb{E}x(t) \\
&+ (A_1 + \hat{\xi}B_1)\mathbb{E}x(t - h_1(t)) \\
\preceq& (\bar{A}_0 + \hat{\xi}\bar{B}_0)\mathbb{E}x(t) \\
&+ (\bar{A}_1 + \hat{\xi}\bar{B}_1)\mathbb{E}x(t - h_1(t)) \\
=& (\bar{A}_0 + \hat{\xi}\bar{B}_0)\mathbb{E}\bar{x}(t) \\
&+ (\bar{A}_1 + \hat{\xi}\bar{B}_1)\mathbb{E}\bar{x}(t - h_1(t)) \\
=& \mathbb{E}\{[\bar{A}_0 + \xi(t)\bar{B}_0]\bar{x}(t) \\
&+ [\bar{A}_1 + \xi(t)\bar{B}_1]\bar{x}(t - h_1(t))\} \\
=& \mathbb{E}\bar{x}(t+1, \phi),
\end{aligned}$$

from which completes the proof of iii).
iv) Firstly, we will prove iv)-1) by induction. For $t = 0$, from assumption on the initial value function δ and $\mathbb{E}\xi(0) = \hat{\xi}$, we then have from system (12) that

$$\begin{aligned}
\mathbb{E}y(1, \delta) =& \mathbb{E}\{[A_0 + \xi(0)B_0]y(0) \\
&+ [A_1 + \xi(0)B_1]y(-h)\} \\
=& (A_0 + \hat{\xi}B_0)\mathbb{E}y(0) \\
&+ (A_1 + \hat{\xi}B_1)\mathbb{E}y(-h) \\
=& (A_0 + \hat{\xi}B_0)\mathbb{E}\delta(0) \\
&+ (A_1 + \hat{\xi}B_1)\mathbb{E}\delta(-h) \\
\preceq& \mathbb{E}\delta(0) = \mathbb{E}y(0, \delta).
\end{aligned}$$

Suppose that $\mathbb{E}y(t+1, \delta) \preceq \mathbb{E}y(t, \delta)$ for all $t \in \{-h, -h+1, \cdots, t_0\}$ for some $t_0 \in \mathbb{N}$.
We will prove that $\mathbb{E}y(t_0 + 2, \delta) \preceq \mathbb{E}y(t_0 + 1, \delta)$. Indeed, from system (12) and the assumption that $\mathbb{E}\xi(t_0 + 1) = \mathbb{E}\xi(t_0) = \hat{\xi}$, one gets

$$\begin{aligned}
\mathbb{E}y(t_0+2, \delta) =& \mathbb{E}\{[A_0 + B_0\xi(t_0+1)]y(t_0+1) \\
&+ [A_1 + B_1\xi(t_0+1)]y((t_0+1) - h)\} \\
=& (A_0 + \hat{\xi}B_0)\mathbb{E}y(t_0+1) \\
&+ (A_1 + \hat{\xi}B_1)\mathbb{E}y((t_0+1) - h) \\
\preceq& (A_0 + \hat{\xi}B_0)\mathbb{E}y(t_0) \\
&+ (A_1 + \hat{\xi}B_1)\mathbb{E}y(t_0 - h) \\
=& \mathbb{E}\{[A_0 + \xi(t_0)B_0]y(t_0) \\
&+ [A_1 + \xi(t_0)B_1]y(t_0 - h)\} \\
=& \mathbb{E}y(t_0+1, \delta).
\end{aligned}$$

By induction argument, the proof of iv)-1) is then completed.

Finally, we use again induction reasoning to prove that iv)-2) is true. For the case $t = 1$, by using the initial condition and the fact that $\mathbb{E}\xi(0) = \hat{\xi}$ and $0 \le h_1(0) \le h$, we then have

$$\begin{aligned}
\mathbb{E}x(1, \delta) =& \mathbb{E}\{[A_0 + \xi(0)B_0]x(0) \\
&+ [A_1 + \xi(0)B_1]x(-h_1(0))\} \\
=& (A_0 + \hat{\xi}B_0)\mathbb{E}x(0) \\
&+ (A_1 + \hat{\xi}B_1)\mathbb{E}x(-h_1(0)) \\
=& (A_0 + \hat{\xi}B_0)\mathbb{E}\delta(0) \\
&+ (A_1 + \hat{\xi}B_1)\mathbb{E}\delta(-h_1(0)) \\
\preceq& (A_0 + \hat{\xi}B_0)\mathbb{E}\delta(0) \\
&+ (A_1 + \hat{\xi}B_1)\mathbb{E}\delta(-h) \\
=& (A_0 + \hat{\xi}B_0)\mathbb{E}y(0) \\
&+ (A_1 + \hat{\xi}B_1)\mathbb{E}y(-h) \\
=& \mathbb{E}\{[A_0 + \xi(0)B_0]y(0) \\
&+ [A_1 + \xi(0)B_1]y(-h)\} \\
=& \mathbb{E}y(1, \delta).
\end{aligned}$$

Suppose that $\mathbb{E}x(t, \delta) \preceq \mathbb{E}y(t, \delta)$ for all $t \in \{-h, -h+1, \cdots, t_0\}$ for some $t_0 \in \mathbb{N}$. We will prove that $\mathbb{E}y(t_0 + 1, \delta) \preceq \mathbb{E}x(t_0 + 1, \delta)$. Indeed, by using induction hypothesis, $\mathbb{E}\xi(t_0) = 0$ and

https://doi.org/10.52111/qnjs.2022.16308

iv)-1), systems (1) and (12) give us

$$\begin{aligned}\mathbb{E}x(t_0+1,\delta) =&\mathbb{E}\{[A_0+\xi(t_0)B_0]x(t_0)\\ &+[A_1+\xi(t_0)B_1]x(t_0-h_1(t_0))\}\\ =&(A_0+\hat{\xi}B_0)\mathbb{E}x(t_0)\\ &+(A_1+\hat{\xi}B_1)\mathbb{E}x(t_0-h_1(t_0))\\ \preceq&(A_0+\hat{\xi}B_0)\mathbb{E}y(t_0)\\ &+(A_1+\hat{\xi}B_1)\mathbb{E}y(t_0-h_1(t_0))\\ \preceq&(A_0+\hat{\xi}B_0)\mathbb{E}y(t_0)\\ &+(A_1+\hat{\xi}B_1)\mathbb{E}y(t_0-h)\\ =&\mathbb{E}\{[A_0+\xi(t_0)B_0]y(t_0)\\ &+[A_1+\xi(t_0)B_1]y(t_0-h)\}\\ =&\mathbb{E}y(t_0+1,\delta).\end{aligned}$$

From induction argument, we have thus proved the conclusion iv)-2). □

4.2. An α-exponential mean estimates for positive stochastic systems

Let us assume throughout this section that the coefficient matrices A_0, A_1, B_0, B_1 and the random process $\xi(t)$ of system (1) satisfy conditions in Lemma 4.2 for which this system is positive. In this section, we will provide a sufficient condition for the α-exponential mean boundedness of the positive system (1). By using results developed in Section 4.1, we will derive an α-exponential mean estimate for state vectors of system (1) with time-varying factor function. Our approach is based on an exponential state transformation and solution comparisons.

Step 1: An exponential state transformation
Let $\alpha > 1$ and let us consider the following α-exponential state transformation

$$p(t) = \alpha^t x(t). \tag{16}$$

We introduce the following notations

$$\varphi(s) := \alpha^s\phi(s) \text{ and } \overline{\varphi}(s) := \alpha^s\bar{\phi}(s), \quad s\in\{-h,-h+1,\cdots,0\}.$$

System (1) then becomes the following system

$$\begin{aligned}p(t+1) =&\alpha[A_0+\xi(t)B_0]p(t)\\ &+\alpha^{(h_1(t)+1)}[A_1+\xi(t)B_1]p(t-h_1(t)),\\ p(s) =&\varphi(s),\ s\in\{-h,-h+1,\cdots,0\},\end{aligned} \tag{17}$$

and from (2), one has

$$0\preceq\mathbb{E}\varphi(s)\preceq\overline{\varphi}(s) \quad \forall s\in\{-h,-h+1,\cdots,0\}. \tag{18}$$

Step 2: Solution comparisons
We consider the following "upper" system of (17)

$$\begin{aligned}\hat{p}(t+1) =&\alpha[A_0+\xi(t)B_0]\hat{p}(t)\\ &+\alpha^{h+1}[A_1+\xi(t)B_1]\hat{p}(t-h_1(t)),\\ \hat{p}(s) =&\varphi(s),\ s\in\{-h,-h+1,\cdots,0\}.\end{aligned} \tag{19}$$

It follows from $0\le h_1(t)\le h\ \forall t\in\mathbb{N}$, $\alpha>1$ and $A_1+\hat{\xi}B_1\in\mathbb{R}^n_{0,+}$ that

$$0\preceq\alpha^{(h_1(t)+1)}(A_1+\hat{\xi}B_1)\preceq\alpha^{h+1}(A_1+\hat{\xi}B_1)\ \forall t\in\mathbb{N}.$$

From this, Lemma 4.2 – ii), iii) and (18), we then obtain

$$\mathbb{E}p(t,\varphi)\preceq\mathbb{E}\hat{p}(t,\varphi)\preceq\mathbb{E}\hat{p}(t,\bar{\varphi}),\ \forall t\in\mathbb{N}. \tag{20}$$

Finally, we consider the following "similar" system of (19)

$$\begin{aligned}z(t+1) =&\alpha[A_0+\xi(t)B_0]z(t)\\ &+\alpha^{h+1}[A_1+\xi(t)B_1]z(t-h),\ t\in\mathbb{N},\\ z(s) =&\eta(s),\ s\in\{-h,-h+1,\cdots,0\},\end{aligned} \tag{21}$$

where the function $\eta(\cdot)\in\mathcal{C}_\sigma([-h,0],\mathbb{R}^n)$ will be defined such that the expectation of the solution $z(t,\eta)$ is a non-increasing function and is an upper bound of the expectation of the solution $\hat{p}(t,\bar{\varphi})$. The next lemma will give us a condition for the existence of such initial value function.

Lemma 4.3. Assume that

$$\rho\left(\alpha\left(A_0+\hat{\xi}B_0\right)+\alpha^{h+1}\left(A_1+\hat{\xi}B_1\right)\right)<1.$$

Then, there exists an initial value function $\eta(\cdot)\in\mathcal{C}_\sigma([-h,0],\mathbb{R}^n)$ such that $\mathbb{E}z(\cdot,\eta)$ is a non-increasing function and

$$\mathbb{E}\hat{p}(t,\bar{\varphi})\preceq\mathbb{E}z(t,\eta),\ \forall t\in\mathbb{N}. \tag{22}$$

Proof. Let us consider the following linear programming problem

$$\begin{bmatrix}-I_n & I_n & 0 & \cdots & 0 & 0\\ 0 & -I_n & I_n & \cdots & 0 & 0\\ 0 & 0 & -I_n & \cdots & 0 & 0\\ \vdots & \vdots & \vdots & \ddots & I_n & 0\\ 0 & 0 & 0 & \cdots & -I_n & I_n\end{bmatrix}u\preceq 0, \tag{23}$$

$$v-u\preceq 0, \tag{24}$$

$$\left[\alpha^{h+1}(A_1+\hat{\xi}B_1)\ 0\cdots 0\ \alpha(A_0+\hat{\xi}B_0)-I_n\right]u\preceq 0, \tag{25}$$

where $v:=[\overline{\varphi}^\top(-h)\ \overline{\varphi}^\top(-h+1)\ \cdots\ \overline{\varphi}^\top(0)]^\top\in\mathbb{R}^{(h+1)n}$ and $u:=[u_{-h}^\top\ u_{-h+1}^\top\ \cdots\ u_0^\top]^\in\mathbb{R}^{(h+1)n}$ are unknown.

https://doi.org/10.52111/qnjs.2021.16308

By using the same argument as in,[36] Step 2 we conclude the proof of this lemma. □

Noting that since both h, $\eta(\cdot)$ and $\mathbb{E}\xi(\cdot)$ are known, we can use system (21) to calculate the expectation of the state vector $z(t,\eta)$ for all $t \in \mathbb{N}$. By combining (16), (20) and (22), we obtain an α-exponential mean estimate with a decreasing factor function for the solution $x(t,\phi)$ of system (1) which is stated in the following theorem.

Theorem 4.4. Let $\alpha > 1$ be such that

$$\rho(\alpha(A_0 + \hat{\xi}B_0) + \alpha^{h+1}(A_1 + \hat{\xi}B_1)) < 1. \quad (26)$$

Then, there exists an initial value function $\eta(\cdot) \in \mathcal{C}([-h,0],\mathbb{R}^n)$ such that the system (1) is α-exponentially mean bounded and its α-exponential mean estimate is given by

$$\mathbb{E}x(t,\phi) \preceq \mathbb{E}z(t,\eta)\alpha^{-t},\ \forall t \in \mathbb{N}, \quad (27)$$

where $z(t,\eta)$ is the solution of the system (21). In addition, $\mathbb{E}z(\cdot,\eta)$ is a non-increasing function.

Remark 4.5. In Lemma 4.3, instead of considering the linear programming (23)–(25), let us consider the following one

$$\min_{u\in\mathbb{R}^{(h+1)n}} f(u) := c^\top(u - v) \ \text{ s.t. } (23),(24),(25), \quad (LP)$$

where $c := [1\ \ 1\ \cdots\ 1]^\top \in \mathbb{R}^{(h+1)n}$. Let u^* be an optimal solution of (LP). By setting

$$\eta(s) = u_s^*, \quad \forall s \in \{-h, -h+1, \cdots, 0\}, \quad (28)$$

the function $\eta(\cdot)$ not only satisfies conditions of Lemma 4.3 but also makes $\sum_{s=-h}^{0} ||\mathbb{E}(\eta(s) - \bar{\varphi}(s))||_1$ smallest. The latter condition means that in general (in the sense of expectation) the function $\eta(\cdot)$ is not too far from $\bar{\varphi}(\cdot)$. This will provide an α-exponential mean estimate of the state vector $x(t,\phi)$ as accurate as possible.

Remark 4.6. By applying the result in Theorem 4.4 to system (6) and noting that

$$\Pi\left(A_0 + \hat{\xi}B_0\right) \succeq 0, \Pi\left(A_1 + \hat{\xi}B_1\right) \succeq 0 \text{ and } \mathbb{E}\pi(\phi(s)) \succeq 0,$$

we then obtain the α-exponentially mean estimate for the non-positive system (1) (given by Theorem 3.2).

5. AN α-EXPONENTIAL MEAN ESTIMATE VIA AN "UPPER BOUND" SYSTEM

For the sake of demonstrating the effectiveness of the IPR approach when applying to the non-positive stochastic discrete-time system (1), we introduce another α-exponential mean estimate for this system via an "upper bound" system, see, e.g..[17,35] In this approach, we will bound from above the system (1) by the following positive stochastic discrete-time system (1)

$$\begin{aligned} u(t+1) =& [|A_0| + |\xi(t)||B_0|]u(t) \\ &+ [|A_1| + |\xi(t)||B_1|]u(t - h_1(t)),\ t \in \mathbb{N}, \\ u(s) =& |\phi(s)|,\ s \in \{-h, -h+1, \cdots, 0\}. \end{aligned} \quad (29)$$

Let us denote by $u(t,|\phi|)$ the solution of this system. By virtue of Lemma 4.2 – i), this system is positive in the sense of expectation, i.e. $\mathbb{E}u(t,|\phi|) \succeq 0$, for all $t \in \mathbb{N}$. The following result gives us an α-exponential mean estimate of system (1) based on this "upper bound" system.

Theorem 5.1. Let us assume that the stochastic process $\xi(t)$ satisfies $\mathbb{E}|\xi(t)| \le \bar{\xi}$ for all $t \in \mathbb{E}$, for some $\bar{\xi} \ge 0$. Assume that there exists $\alpha > 1$ such that

$$\rho(\alpha(|A_0| + \bar{\xi}|B_0|) + \alpha^{h+1}(|A_1| + \bar{\xi}|B_1|)) < 1. \quad (30)$$

Then, there exists a vector-valued function $\lambda(t) \in \mathbb{R}^n_{0,+},\ t \in \mathbb{N}$ such that

$$\mathbb{E}x(t,\phi) \preceq \lambda(t)\alpha^{-t},\ \forall t \in \mathbb{N}, \quad (31)$$

In addition, $\lambda(\cdot)$ is a non-increasing function.

Proof. To complete the proof of Theorem 5.1, we just need to prove that system (29) is an upper bound of system (1) in the sense of expectation, i.e.,

$$|\mathbb{E}x(t,\phi)| \preceq \mathbb{E}u(t,|\phi|),\ \forall t \in \mathbb{N}. \quad (32)$$

The above inequality will be proved by induction. For all $s \in \{-h, -h+1, \cdots, 0\}$, by applying the Jensen's inequality, see, e.g.,[55] for the convex function $f(x) = |x|$ and using the initial conditions for systems (1) and (29), one gets

$$|\mathbb{E}x(s,\phi)| = |\mathbb{E}\phi(s)| \preceq \mathbb{E}|\phi(s)| = \mathbb{E}u(s,|\phi|).$$

Suppose that (32) is valid for all $t \in \{-h, -h+1, \cdots, t_0\}$, for some $t_0 \in \mathbb{N}$. Let us prove that this inequality also holds at $t = t_0 + 1$. Indeed, from the definition of systems (1) and (29) and remembering that $0 \le h_1(t_0) \le h$, we then have

$$
\begin{aligned}
|\mathbb{E}x(t_0,\phi)| &= |\mathbb{E}\{[A_0+\xi(t_0)B_0]x(t_0)\\
&\quad + [A_1+\xi(t_0)B_1]x(t_0-h_1(t_0))\}|\\
&= |\{[A_0+\mathbb{E}\xi(t_0)B_0]\mathbb{E}x(t_0)\\
&\quad + [A_1+\mathbb{E}\xi(t_0)B_1]\mathbb{E}x(t_0-h_1(t_0))\}|\\
&\preceq [|A_0|+|\mathbb{E}\xi(t_0)||B_0|]|\mathbb{E}x(t_0)|\\
&\quad + [|A_1|+|\mathbb{E}\xi(t_0)||B_1|]|\mathbb{E}x(t_0-h_1(t_0))\ |\\
&\preceq [|A_0|+\mathbb{E}|\xi(t_0)||B_0|]\mathbb{E}u(t_0)\\
&\quad + [|A_1|+\mathbb{E}|\xi(t_0)||B_1|]\mathbb{E}u(t_0-h_1(t_0))\\
&= \mathbb{E}\{[|A_0|+|\xi(t_0)||B_0|]u(t_0)\\
&\quad + [|A_1|+|\xi(t_0)||B_1|]u(t_0-h_1(t_0))\}\\
&= \mathbb{E}u(t_0+1,|\phi|),
\end{aligned}
$$

where the second inequality is obtained from the induction hypothesis and the Jensen's inequality. This concludes the proof. □

Remark 5.2.

1. The result in Theorem 5.1 seems to be more natural than the one in Theorem 3.2. However, we should note that system (29) is an overestimate of system (1). As a consequence, the range of α to get an α-exponential mean estimate (condition (30)) will be narrowed. In addition, the α-exponential mean estimate given in this theorem is also looser than the one obtained by Theorem 3.2. These advantages of the IPR approach will be demonstrated in Section 6

2. By using a direct evaluation on the expectation of the square norm of the state vector, Xu and Ge,[17] proved the mean square exponential stability of system (1) under the usual condition on the stochastic process $\xi(t)$, i.e., $\mathbb{E}\xi(t)=0$ and $\mathbb{E}\xi(t)^2=1$. From this result and the Jensen's inequality, we can derive an α-exponential mean estimate for the system (1). It worth noting that we can apply a direct evaluation on the expectation of state vector (not the square norm of state vector) to obtain a more accurate α-exponential mean estimate for this system. However, these two estimates will be not as accurate as the ones obtained in Theorems 3.2 and 5.1.

6. ILLUSTRATIVE EXAMPLE

This section is devoted to verify the effectiveness of the IPR approach for deriving the α-exponential mean estimate of the stochastic discrete-time system with time-varying delay (1). Let us consider system (1) with the following coefficient matrices

$$
A_0=\begin{bmatrix}0.51 & 0.10 & -0.12\\ 0.04 & -0.12 & 0.04\\ 0.12 & 0.05 & -0.06\end{bmatrix}
$$

$$
A_1=\begin{bmatrix}0.12 & 0.01 & -0.08\\ -0.03 & -0.15 & 0.02\\ 0.04 & -0.01 & 0.10\end{bmatrix}
$$

$$
B_0=\begin{bmatrix}-0.21 & -0.03 & 0.11\\ -0.05 & 0.02 & 0.01\\ 0.02 & 0.01 & -0.02\end{bmatrix}
$$

$$
B_1=\begin{bmatrix}0.01 & -0.02 & 0.02\\ 0.05 & -0.03 & -0.07\\ -0.05 & 0.01 & -0.01\end{bmatrix}
$$

The stochastic process $\xi(t)$ will be chosen such that $\mathbb{E}\xi(t)=0.2$ and $\mathbb{E}|\xi(t)|\le 0.8$, for all $t\in\mathbb{N}$. We assume that the expectation of the initial value function is bounded by $\bar{\phi}(-2)=[3.3,\ 3.8,\ 1.7], \bar{\phi}(-1)=[2.4,\ 2.8,\ 0.7]$ and $\bar{\phi}(0)=[-3.0,\ -3.3,\ 1.7]$. The bound of the time-varying delays h is set by 2.

By using one dimensional search, we can find the largest value of the decay rate α such that Theorems 4.4 and 5.1 can be applied. The results are given in Table 1. From this table, we can see that the sufficient condition derived by the IPR method the (condition (10)) gives us a larger range of decay rate α than the condition obtained in Theorem 5.1 (condition (30)). This means that the α-exponential mean estimate of state vectors obtained by Theorem 4.4 has a broader applicability.

Table 1. Ranges of decay rate α

Methods	Range of α
Theorem 3.2 (condition (10))	[1, 1.294]
Theorem 5.1 (condition (30))	[1, 1.046]

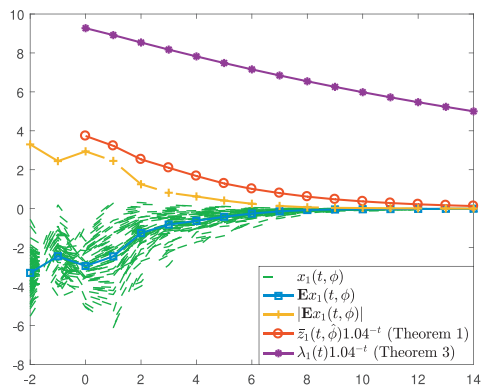

Figure 1. Trajectories of $x_1(t,\phi)$, the mean value $\mathbb{E}x_1(t,\phi)$ and its α-exponential mean estimates

https://doi.org/10.52111/qnjs.2021.16308

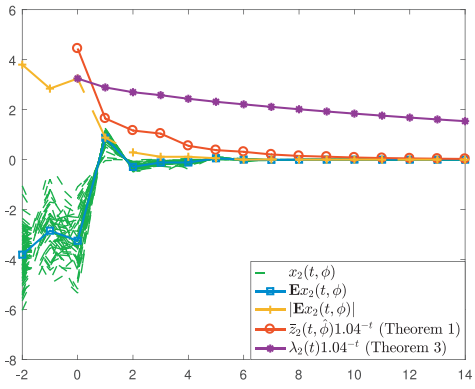

Figure 2. Trajectories of $x_2(t,\phi)$, the mean value $\mathbb{E}x_2\,(t,\phi)$ and its α-exponential mean estimates

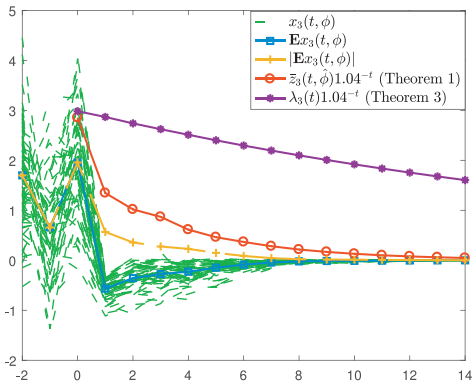

Figure 3. Trajectories of $x_3(t,\phi)$, the mean value $\mathbb{E}x_3(t,\phi)$ and its α-exponential mean estimates

To illustrate the behavior of system (1) and α-exponential mean estimates of this system, for each $t \in \mathbb{N}$ and $s \in \{-2,-1,0\}$, we generate 100 random variables $\xi(t)$ and $\zeta(s)$ such that $\mathbb{E}\xi(t) = 0.2, |\mathbb{E}\xi(t)| \leq 0.8$ and $\mathbb{E}\zeta(s) = 0$ to create 100 stochastic systems under the form (1). The initial condition is chosen by $\phi(s) = \bar{\phi}(s) + \zeta(s)$ for $s = -2,-1,0$. Let us choose the decay rate $\alpha = 1.04$ for which both results in Theorem 3.2 and 5.1 can be applied. Figures 1–3 show us the behavior of 100 realizations of the system (1) together with its mean values $\mathbb{E}x(t,\phi)$ and its α-exponential mean estimates $\mathbb{E}\bar{z}(t,\eta)$. As we can see, the expectation of state vectors (the line) is not positive. The behavior of the line means that these systems are α-exponentially mean bounded. Moreover, these figures also show us that the α-exponential mean estimate obtained by the IPR approach (the line) is more accurate than the one given by the "upper bound" approach (the line). This verifies the effectiveness of the IPR approach on the stochastic discrete-time system with time-varying delays (1).

7. CONCLUSION AND PERSPECTIVES

In this paper, we consider a class of linear stochastic discrete-time systems with time-varying delays which can be seen as the usual linear discrete-time system with time-varying delays and with random uncertainty. Under the assumption that the random process does not lose the positivity of coefficient matrices, we prove that the system is still positive in the sense of expectation. In addition, a new solution comparison for stochastic systems is derived and then is applied to obtain an α-exponential mean estimate of positive stochastic systems. This result is used together with the IPR approach to obtain an α-exponential mean estimate for non-positive stochastic discrete-time systems. Some numerical examples are performed to demonstrate the effectiveness of the IPR approach on stochastic systems. The approach in this paper can be also applied to some other problems, e.g., interval observer,[30,56,57] ℓ_∞-gain analysis,[58,59] etc. Finally, we list here some other open problems which can be studied for stochastic systems: the positivity in the sense of probability for stochastic systems, the exponential estimate in the sense of probability for stochastic systems, etc.

Acknowledgments

The authors would like to thank the editor(s) and anonymous reviewers for their constructive comments and suggestions that have helped to improve the present paper.

REFERENCES

1. A. Germani, C. Manes, P. Palumbo. Representation of a class of mimo systems via internally positive realization, *European Journal of Control*, **2010**, *16*(3), 291 - 304.

2. F. Cacace, A. Germani, C. Manes, R. Setola. A new approach to the internally positive representation of linear mimo systems, *IEEE Transactions on Automatic Control*, **2012**, *57*(1), 119 - 134.

3. F. Cacace, L. Farina, A. Germani, C. Manes. Internally positive representation of a class of continuous time systems, *IEEE Transactions on Automatic Control*, **2012**, *57*(12), 3158 - 3163.

4. F. Conte, V.D. Iuliis, C. Manes. *Internally positive representations and stability analysis of linear delay systems with multiple time-varying delays, Positive Systems*, Springer, Cham, 2017, 81 - 93.

5. V. D. Iuliis, A. D'Innocenzo, A. Germani, C. Manes. Internally positive representations and stability analysis of linear differential systems with multiple time-varying delays, *IET Control Theory & Applications* , **2019**, *13*(7), 920 - 927.

6. V. D. Iuliis, A. Germani, C. Mane. Internally positive representations and stability analysis of coupled differential-difference systems with time-varying delays, *IEEE Transactions on Automatic Control*, **2019**, *64*(6), 2514 - 2521.

7. V. D. Iuliis, A. D'Innocenzo, A. Germani, C. Manes. Stability analysis of coupled differential-difference systems with multiple time-varying delays: A positivity-based approach, *IEEE Transactions on Automatic Control*, **2021**, *66*(12), 6085 - 6092.

8. Q. Xiao, Y. Yang, T. Huang. Internally positive representation to stability of delayed timescale-type differential- difference equation, *IEEE Access*, **2021**, *9*, 34660 - 34666.

9. V. D. Iuliis, A. Germani, C. Manes. Internally positive representations and stability analysis of linear difference systems with multiple delays, *IFAC-PapersOnLine*, 20$^{\text{th}}$ IFAC World Congress, **2017**, *50*(1), 3099 - 3104.

10. X. Mao. *Stochastic differential equations and applications*, second edition, Woodhead Publishing, Cambridge, 2007.

11. L. Wu, P. Shi, H. Gao. State estimation and sliding-mode control of Markovian jump singular systems, *IEEE Transactions on Automatic Control*, **2010**, *55*(5), 1213 - 1219.

12. S. Aberkane. Stochastic stabilization of a class of nonhomogeneous Markovian jump linear systems, *Systems & Control Letters*, **2011**, *60*(3), 156 - 160.

13. P. Bolzern, P. Colaneri, G.D. Nicolao. Stochastic stability of positive Markov jump linear systems, *Automatica*, **2014**, *50*(4), 1181 - 1187.

14. W. Zhang, Y. Zhao, L. Sheng. Some remarks on stability of stochastic singular systems with state-dependent noise, *Automatica*, **2015**, *51*, 273 - 277.

15. X. Yang, Q. Zhu. New criteria for mean square exponential stability of stochastic systems with variable and distributed delays, *IET Control Theory & Applications*, **2019**, *13*, 116 - 122.

16. P. H. A. Ngoc, H. L. Trung. A novel approach to mean square exponential stability of stochastic delay differential equations, *IEEE Transactions on Automatic Control*, **2021**, *66*(5), 2351 - 2356.

17. L. Xu, S. S. Ge. Exponential ultimate boundedness of nonlinear stochastic difference systems with time-varying delays, *International Journal of Control*, **2015**, *88*(5), 983 - 989.

18. Y. Chen, W. X. Zheng, A. Xue. A new result on stability analysis for stochastic neutral systems, *Automatica*, **2010**, *46*(12), 2100 - 2104.

19. V. Dragan, T. Morozan. Mean square exponential stability for some stochastic linear discrete time systems, *European Journal of Control*, **2006**, *12*(4), 373 - 395.

20. P. Bolzern, P. Colaner, G. D. Nicolao. On almost sure stability of continuous-time markov jump linear systems, *Automatica*, **2006**, *42*(6), 983 - 988.

21. D. J. Higham, X. Mao, C. Yuan. Almost sure and moment exponential stability in the numerical simulation of stochastic differential equations, *SIAM Journal on Numerical Analysis*, **2007**, *45*(2), 592 - 609.

22. Q. Gu, X. Mao, R. Yue. Almost sure exponential stability of stochastic differential delay equations, *SIAM Journal on Control and Optimization*, **2016**, *54*(4), 1919 - 1933.

23. Y. Song, J. Yang, T. Yang, M. Fei. Almost sure stability of switching markov jump linear systems, *IEEE Transactions on Automatic Control*, **2016**, *61*(9), 2638 - 2643.

24. L. V. Hien. An LP approach to full-order and reduced-order state estimations of positive Markov jump systems with delay, *International Journal of Systems Science*, **2017**, *48*(12), 2534 - 2543.

25. L. V. Hien, H. Trinh. Delay-dependent stability and stabilisation of two-dimensional positive markov jump systems with delays, *IET Control Theory & Applications*, **2017**, *11*, 1603 - 1610.

26. Y. Chen, Y. Bo, B. Du. Stochastic stability of positive markov jump linear systems with completely/partially known transition rates, *Transactions of the Institute of Measurement and Control*, **2018**, *40*(9), 2724 - 2731.

27. X. Liu. *Stability and stabilization of positive systems with delays*, International Conference on Communications, Circuits and Systems, 2009.

https://doi.org/10.52111/qnjs.2021.16308

28. X. Liu, W. Yu, L. Wang. Stability analysis for continuous-time positive systems with time-varying delays, *IEEE Transactions on Automatic Control*, **2010**, *55*(4), 1024 - 1028.

29. A. Hmamed, M. A. Rami, A. Benzaouia, F. Tadeo. Stabilization under constrained states and controls of positive systems with time delays, *European Journal of Control*, **2012**, *18*(2), 182 - 190.

30. M. A. Rami, M. Schönlein, J. Jordan. Estimation of linear positive systems with unknown time-varying delays, *European Journal of Control*, **2013**, *19*(3), 179 - 187.

31. S. Zhu, M. Meng, C. Zhang. Exponential stability for positive systems with bounded time-varying delays and static output feedback stabilization, *Journal of the Franklin Institute*, **2013**, *350*(3), 617 – 636.

32. J. Shen, J. Lam. Stability and performance analysis for positive fractional-order systems with time-varying delays, *IEEE Transactions on Automatic Control*, **2015**, *61*(9), 2676 - 2681.

33. Y. Cui, J. Shen, Z. Feng, Y. Chen. Stability analysis for positive singular systems with time-varying delays, *IEEE Transactions on Automatic Control*, **2017**, *63*(5), 1487 - 1494.

34. P. T. Nam, P. N. Pathirana, H. Trinh. Partial state bounding with a pre-specified time of non-linear discrete systems with time-varying delays, *IET Control Theory & Applications*, **2016**, *10*(13), 1496 - 1502.

35. P. T. Nam, P. N. Pathirana, H. Trinh. Minimization of state bounding for perturbed positive systems with delays, *SIAM Journal on Control and Optimization*, **2018**, *56*(3), 1739 - 1755.

36. C. T. Tinh, P. T. Nam, T. N. Nguyen, H. Trinh. Exponential estimate with a time-varying factor for positive discrete-time systems with time-delays, *Applied Mathematics Letters*, **2021**, *119*.

37. P. T. Nam, L. Q. Thuan, T. N. Nguyen, H. Trinh. Comparison principle for positive time-delay systems: An extension and its application, *Journal of the Franklin Institute*, **2021**, *358*(13), 6818 - 6834.

38. P. H. A. Ngoc. New criteria for exponential stability of nonlinear time-varying differential systems, *International Journal of Robust and Nonlinear Control*, **2014**, *24*, 264 - 275.

39. P. H. A. Ngoc. Exponential stability of coupled linear delay time-varying differential-difference equations, *IEEE Transactions on Automatic Control*, **2018**, *63*(3), 843 - 848.

40. N. H. Sau, D.C. Huong, M. V. Thuan. New results on reachable sets bounding for delayed positive singular systems with bounded disturbances, *Journal of the Franklin Institute*, **2021**, *358*(1), 1044 - 1069.

41. D. C. Huong, N. H. Sau. Finite-time stability and stabilisation of singular discrete-time linear positive systems with time-varying delay, *International Journal of Systems Science*, **2019**, *50*(15), 2824 - 2837.

42. D. C. Huong, N. H. Sau. Stability and l_∞-gain analysis for discrete-time positive singular systems with unbounded time-varying delays, *IET Control Theory & Applications*, **2019**, *14*(17), 2507 - 2513.

43. S. Zhu, Q. L. Han, C. Zhang. L_1-Stochastic stability and L_1-Gain performance of positive Markov jump linear systems with time-delays: Necessary and sufficient conditions, *IEEE Transactions on Automatic Control*, **2017**, *62*(7), 3634 - 3639.

44. J. Xie, S. Zhu, J. Feng. Delay-dependent and decay-rate-dependent conditions for exponential mean stability and non-fragile controller design of positive Markov jump linear systems with time-delay, *Applied Mathematics and Computation*, **2020**, *369*.

45. J. Jiang, J. Shen. $l_1/l\_$ Filter-based fault detection for positive Markov jump linear systems with time delay, *IEEE*, **2019**, *7*, 117727 - 117739.

46. L. J. Liu, X. Zhang, X. Zhao, B. Yang. Stochastic finite-time stabilization for discrete-time positive Markov jump time-delay systems, *Journal of the Franklin Institute*, **2022**, *359*(1),84 - 103.

47. S. Zhu, Q. L. Han, C. Zhang. Investigating the effects of time-delays on stochastic stability and designing l_1-gain controllers for positive discrete-time Markov jump linear systems with time-delay, *Information Sciences*, **2016**, *355-356*, 265 - 281.

48. L. Huang, H. Hjalmarsson, H. Koeppl. Almost sure stability and stabilization of discrete-time stochastic systems, *Systems & Control Letters*, **2015**, *82*, 26 - 32.

49. Z. Y. Li, Y. Wang, B. Zhou, G. R. Duan. Detectability and observability of discrete-time stochastic systems and their applications, *Automatica*, **2009**, *45*(5), 1340 - 1346.

50. Z. Wang, Y. Liu, G. Wei, X. Liu. A note on control of a class of discrete-time stochastic systems with distributed delays and nonlinear disturbances, *Automatica*, **2010**, *46*(3), 543 - 548.

https://doi.org/10.52111/qnjs.2022.16308

51. A. Berman, R. J. Plemmons. *Nonnegative matrices in the mathematical sciences*, Society for Industrial and Applied Mathematics, 1994.

52. J. Liang, Y. Jin. *Positivity and stability of continuous-time stochastic linear systems, Positive Systems*, Springer International Publishing, Cham, 2019, 85 - 96.

53. T. Kaczorek. *Positive 1D and 2D Systems*, Springer-Verlag, London, 2002.

54. X. Liu, W. Yu, L. Wang. Stability analysis of positive systems with bounded time-varying delays, *IEEE Transactions on Circuits and Systems II: Express Briefs*, **2009**, *56*(7), 600 - 604.

55. R. Durrett. *Probability: Theory and Examples*, 5th edn, Cambridge University Press, 2019.

56. D. C. Huong, M. V. Thuan. On reduced-order linear functional interval observers for nonlinear uncertain time-delay systems with external unknown disturbances, *Circuits, Systems, and Signal Processing*, **2019**, *38*(5), 2000 - 2022.

57. M. A. Rami, U. Helmke, F. Tadeo. *Positive observation problem for linear time-delay positive systems*, Mediterranean Conference on Control & Automation, 2007.

58. J. Shen, J. Lam. ℓ_∞/L_∞-gain analysis for positive linear systems with unbounded time-varying delays, *IEEE Transactions on Automatic Control*, **2015**, *60*(3), 857 - 862.

59. J. Shen, J. Lam. On ℓ_∞ and L_∞ gains for positive systems with bounded time-varying delays, *International Journal of Systems Science*, **2015**, *46*(11), 1953 - 1960.

https://doi.org/10.52111/qnjs.2021.16308

MỤC LỤC